Spatiotemporal *stop-and-go* dynamics of the mitochondrial TOM core complex correlates with channel activity

Von der Fakultät Energie-, Verfahrens- und Biotechnik der Universität Stuttgart

zur

Erlangung der Würde eines Doktors der Naturwissenschaften (Dr. rer. nat.)

genehmigte Abhandlung

Vorgelegt von

M.Sc. Shuo Wang

aus Kaifeng

Hauptberichter:	Prof. Dr. Stephan Nussberger
Nebenberichter:	Prof. Dr. Robin Ghosh

Tag der mündlichen Prüfung:	31.07.2023

Institut für Biomaterialien und biomolekulare Systeme der Universität Stuttgart

2023

Ich erkläre hiermit, dass ich die vorliegende Arbeit selbstständig verfasst habe und keine anderen als die angegebenen Quellen und Hilfsmittel benutzt habe.

Stuttgart, den 23. 02. 2023

Learn from yesterday, live for today, hope for tomorrow. The important thing is not to stop questioning.

Albert Einstein

Contents

Abbreviations

AFM	Atomic force microscopy
APS	Ammonium persulfate
CFTR	Cystic fibrosis transmembrane conductance regulator
CV	Column volume
CMC	Critical micelles concentration
DDM	n-dodecyl-β-D-maltoside
DIB	Droplet interface bilayer
DOPC	1,2-dioleoyl-sn-glycero-3-phosphocholine
DPhPC	1,2-diphytanoyl-sn-glycero-3-phosphocholine
ECM	Extracellular matrix
EDTA	Ethylenediaminetetraacetic acid
EMCCD	Electron-multiplying CCD camera
Erv1	Essential for respiration and vegetative growth
FRET	Förster resonance energy transfer
HEPES	4-(2-hydroxyethyl)-1-piperazineethanesulfonic acid
αHL	α-Hemolysin
IM	Inner membrane
IMS	Intermembrane space
LB	Luria-Bertani
MBP	Maltose-binding protein
Mia40	Mitochondrial intermembrane space import and assembly
MIM	Mitochondrial import
MINIFLUX	Mminimum photon flux fluorescence microscopy
MPP	Mitochondrial processing peptidase
MSD	Mean square displacement
MSK	Membrane skeleton
Ni-NTA	Nickel-nitrilotriacetic acid
NMR	Nuclear magnetic resonance
Octyl-POE	n-octyl polyoxyethylene

OG	n-octyl β-D-glucopyranoside
OM	Outer membrane
PAM	Presequence translocase
PMMA	Poly (methyl methacrylate)
PMSF	Phenylmethylsulfonyl fluoride
POPC	1-palmitoyl-2-oleoyl-sn-glycero-3-phosphocholine
ROI	Region of interested
TCEP	Tris(2-carboxyethyl) phosphine
TEMED	Tetramethylethylenediamine
TfR	Transferrin receptor
TIM	Translocase of the inner (mitochondrial) membrane
TIRF	Total internal reflection fluorescence
TOM	Translocase of the outer (mitochondrial) membrane
TOM-CC	TOM core complex
Tris	Tri(hydroxymethyl)aminomethane
SAM	Sorting and assembly machinery
SDS	Sodium dodecyl sulfate
SDS-PAGE	Sodium dodecyl sulfate polyacrylamide gel electrophoresis
SEM	Standard error of the mean
Small TIMs	Small Tim proteins in the IMS
SPT	Single particle tracking
Su9	F_0-ATPase subunit 9
Su9-MBP	F_0-ATPase subunit 9 fused to maltose-binding protein
VDAC	Voltage dependent anion channel

1 Zusammenfassung

Der TOM-Komplex der äußeren Membran von Mitochondrien ist die Haupteingangspforte für kernkodierte Proteine aus dem Zytosol in Mitochondrien. In dieser Arbeit wird mit Hilfe der Totalinterferenzfluoreszenzmikroskopie (TIRF-M) die Korrelation zwischen lateraler Proteindiffusion und Kanalaktivität der allgemeinen Proteinimportpore der Mitochondrien (TOM-CC) in Membranen, die auf ultradünnen Hydrogelfilmen ruhen, am einzelnen Molekül untersucht. Die Einzelmolekülstudien führen dabei zur Beobachtung und Entdeckung von Phänomenen, die bisher in Ensemble-Messungen im Verborgenen blieben. Mit Hilfe von elektrodenfreien optischen Aufzeichnungen des Ionenflusses wird in der vorliegenden Arbeit gezeigt, dass TOM-CC reversibel zwischen drei Zuständen der Ionenpermeabilität in Verbindung mit der Proteindiffusion wechselt. Während sich frei diffundierende TOM-CC-Moleküle überwiegend in einem Zustand hoher Permeabilität befinden, befinden sich nicht mobile Moleküle meist in einem Zustand mittlerer oder niedriger Permeabilität. Dieses Verhalten lässt sich durch mechanische Bindung der beiden Tom22-Untereinheiten des TOM Komplexes an das Hydrogel und ein damit einhergehendes kombinatorisches Öffnen und Schließen der beiden β-Fassporen Tom40 von TOM-CC erklären. TOM-CC ist somit der erste β-Fass-Membranproteinkomplex, der membranzustandsabhängige und mechanosensitive Eigenschaften aufweist.

2 Summary

The TOM complex of the outer membrane of mitochondria is the main entry gate for nuclear-encoded proteins from the cytosol into mitochondria. Single-molecule studies can reveal phenomena that remain hidden in ensemble measurements. In this thesis, total internal reflection fluorescence (TIRF) microscopy has been used to study the correlation between lateral protein diffusion and channel activity of the general protein import pore of mitochondria (TOM-CC) in membranes resting on ultrathin hydrogel films. Using electrode-free optical recordings of ion flux, it is shown that TOM-CC switches reversibly between three states of ion permeability associated with protein diffusion. While freely diffusing TOM-CC molecules are predominantly in a high permeability state, non-mobile molecules are mostly in an intermediate or low permeability state. This behavior can be explained by the mechanical binding of the two protruding Tom22 subunits to the hydrogel and a concomitant combinatorial opening and closing of the two β-barrel pores of TOM-CC. TOM-CC is thus the first β-barrel membrane protein complex to exhibit membrane state-dependent mechanosensitive properties.

3 Introduction

3.1 Mitochondria

Mitochondria are the powerhouses of eukaryotic cells. Except this main function, mitochondria are also involved in numerous metabolic processes and signaling pathways including quality control and programmed cell death (for review, see Nunnari and Suomalainen, 2012; Bratic and Larsson, 2013).

Mitochondria have a characteristic architecture with two membranes and two aqueous compartments, i.e. an outer membrane, an intermembrane space, an inner membrane containing invaginations termed cristae, and a matrix (for review, see Kühlbrandt, 2015; for review, see Wiedemann and Pfanner, 2017; for review, see Pfanner et al., 2019). Both outer and inner membranes are formed by amphiphilic phospholipids, into which hydrophobic transmembrane proteins are embedded. The mitochondrial outer membrane is permeable for ions and small molecules, while the mitochondrial inner membrane has much more restricted permeability. Consequently, the composition is very different between the cytosol and the mitochondrial matrix.

The mitochondrial outer membrane encloses the entire organelle and contains two types of integral transmembrane proteins with predominantly β-barrel or α-helical secondary structure. Ions and small, uncharged molecules up to a molecular mass of about 5 kDa can freely pass through the outer membrane via pore-forming transmembrane protein channels (Demirel and Gerbaud, 2019), such as the voltage dependent anion channel VDAC (Bayrhuber et al., 2008). However, larger molecules, especially nuclear encoded precursor proteins synthesized in the cytosol, do not have free access to mitochondria; they must be imported into the organelle by specific protein translocases (Figure 3.1), known as TOM, SAM and MIM in the outer mitochondrial membrane and TIM23 and TIM22 in the inner mitochondrial membrane (for review, see Herrmann and Neupert, 2004; for review, see Wiedemann and Pfanner, 2017).

The mitochondrial inner membrane possesses a several times larger surface area than the outer membrane, due to the extensive folding (Demirel and Gerbaud, 2019). It contains the fully

assembled complexes of the electron transport chain (Demirel and Gerbaud, 2019), including ATP synthase, and is the site where oxidative phosphorylation and ATP synthesis occur. The inner membrane also contains two translocase protein machineries TIM23 and TIM22 that transport mitochondrial-incoming precursor proteins across the inner membrane or mediate their insertion into the inner membrane (Demishtein-Zohary and Azem, 2017; for review, see Wiedemann and Pfanner, 2017; Valpadashi et al., 2021). In contrast to the high permeability of the outer mitochondrial membrane, the inner membrane acts as a strict diffusion barrier for all ions and molecules (for review, see Kühlbrandt, 2015; Demirel and Gerbaud, 2019). This allows the formation of a proton-motive force and thus an electrochemical membrane potential of up to ~180 mV across the membrane (Zorova et al., 2018), a prerequisite for ATP synthesis. This in turn leads to specific structural requirements for the protein translocases TIM22 and TIM23 when transferring proteins across or into the inner membrane without membrane potential dissipation.

The mitochondrial intermembrane space (IMS) is 6 to 8 nm wide (Demirel and Gerbaud, 2019). It plays a vital role in the coordination of mitochondrial activities with other cellular processes (Herrmann and Riemer, 2010), such as the transfer of precursors from TOM to SAM, TIM23 and TIM22 via specific chaperone transport proteins (Tim8, Tim9, Tim10, Tim13). The IMS also contains the mitochondrial intermembrane space import and assembly complex MIA to promote the folding of cysteine-rich imported precursors in the IMS (Webb et al., 2006; Beverly et al., 2008; Gebert et al., 2008; Banci et al., 2010; Peleh et al., 2016).

The innermost compartment of mitochondria is the mitochondrial matrix. In this compartment, numerous enzymatic reactions take place, such as the citric acid cycle as well as organellar DNA replication, transcription, protein biosynthesis of the few proteins that are encoded in mitochondria themselves (Demirel and Gerbaud, 2019). It contains the mitochondrial genetic system and the enzymes responsible for the central reactions of oxidative metabolism, i.e., oxidative degradation of carbohydrates and fatty acids as main source of energy for metabolism in animal cells.

3.2 Protein translocation into mitochondria

While about 99% of mitochondrial proteins (more than 1000 different proteins) are nuclear-encoded and synthesized on cytosolic ribosomes, only a small fraction of proteins is encoded
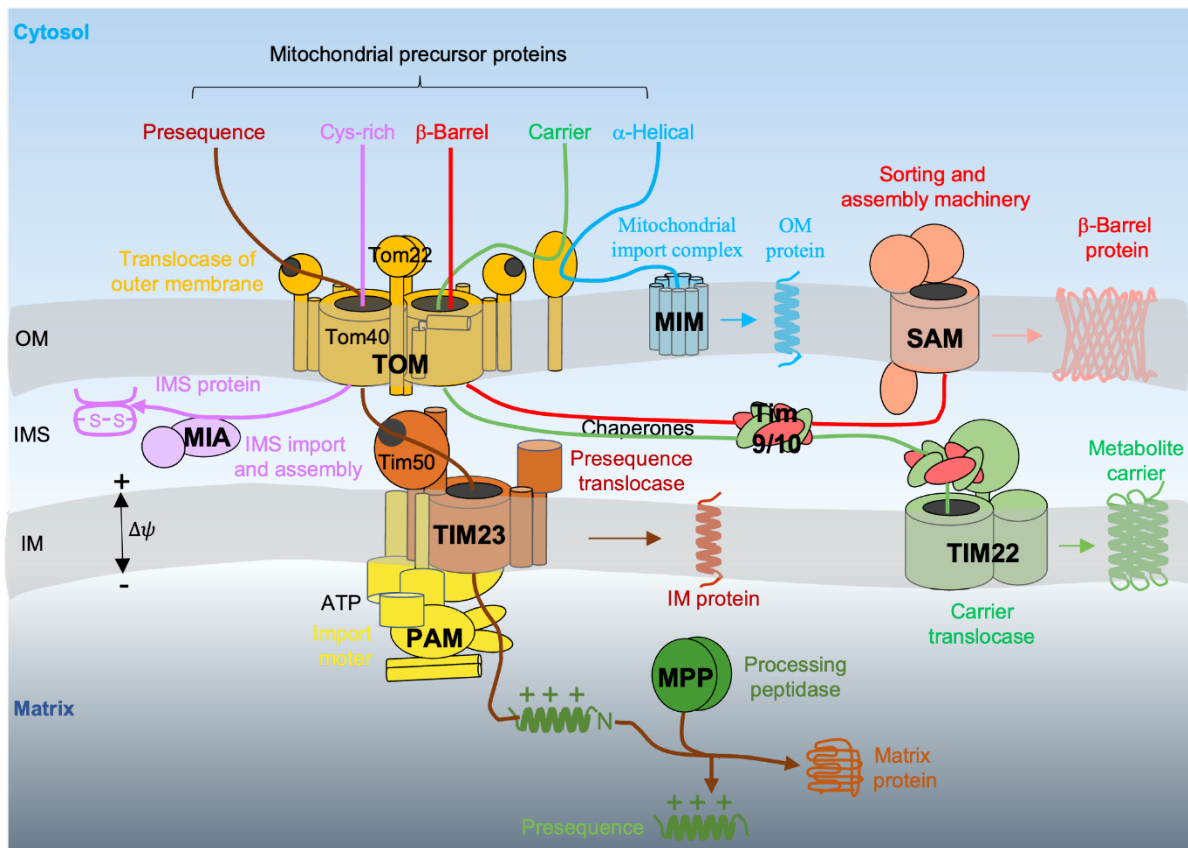
Figure 3.1: ***Protein import pathways into mitochondria.*** *Nuclear-encoded precursor proteins carrying a presequence destined for the mitochondrial matrix are imported by the outer membrane translocase TOM and the inner membrane presequence translocase TIM23. Cysteine-rich precursor proteins destined for the IMS are imported via TOM. Barrel protein precursors destined for incorporation into the outer mitochondrial membrane are transported by TOM and small TIM chaperones, and they are released into the outer membrane by the sorting and assembly machinery SAM. Finally, carrier precursor proteins are imported from the cytosol into the mitochondrial inner membrane via TOM, small TIM chaperones and the inner membrane TIM22 machinery. Single-helical transmembrane segments are directly incorporated into the OM via TOM and the mitochondrial import complex MIM. OM, mitochondrial outer membrane; IM, mitochondrial inner membrane; IMS, intermembrane space.*

by the mitochondrial genome. In humans, for example, these are 13 subunits of the human electron transport chain (for review, see Wiedemann and Pfanner, 2017). The nuclear-encoded mitochondrial proteins are equipped with specific targeting signals that direct freshly synthesized proteins from the cytosol into the mitochondria and, via the mitochondrial protein import machinery TOM, SAM, MIM, MIA, TIM23, and TIM22 (Figure 3.1 and Table 3.1), into the designated mitochondrial subcompartments (for review, see Dolezal et al., 2006; for review, see Neupert and Herrmann, 2007; for review, see Kutik et al., 2009). Thus, the

mitochondrial protein import machineries TOM, SAM, MIM, MIA, TIM23 and TIM22 are essential for the control of mitochondrial biogenesis, signaling and metabolism.

Five major pathways for protein precursor import have been identified, termed *presequence-, Cys-rich-, β-barrel-, carrier-, and α-helical-pathways*, and characterized by different types of targeting signals (Figure 3.1) (for review, see Wiedemann and Pfanner, 2017; for review, see Pfanner et al., 2019).

The classical protein import pathway is the *presequence-pathway* (Figure 3.1), which is responsible for the transport of around 60 % of all mitochondrial proteins (Roise et al., 1986; Abe et al., 2000; Vögtle et al., 2009). The precursors of these proteins are synthesized with N-terminal targeting signals, the so-called presequence, which is proteolytically cleaved after the import of the protein. They comprise amphipathic α-helices containing a positively charged hydrophilic face and a hydrophobic face (Roise et al., 1986). The presequence-bearing precursors are first recognized and bound by the TOM receptor Tom20 (Table 3.1), passed to the TOM receptor Tom22 and then translocated across the mitochondrial outer membrane via TOM subunit Tom40 (Kiebler et al., 1990; Mokranjac and Neupert, 2015). When the precursor appears at the intermembrane space surface of Tom40-Tom22, the receptor subunit Tim50 of TIM23 binds to it (Rahman et al., 2014). Proteins with a second hydrophobic stop-transfer targeting sequence are laterally released via TIM23 into the inner membrane (Glick et al., 1992; Botelho et al., 2011). Proteins without this signal sequence are driven by the membrane potential $\Delta\psi$ across the mitochondrial inner membrane and the presequence translocase-associated motor PAM (Figure 3.1) via TIM23 through the inner membrane into the matrix (Truscott et al., 2001; Meinecke et al., 2006). The presequence of the imported precursors is cleaved off by the mitochondrial processing peptidase MPP and the proteins fold into their functional conformation (Schulz and Rehling, 2014; Fukasawa et al., 2015).

Protein import of precursors that do not carry cleavable presequences but contain other targeting signals (for review, see Wiedemann and Pfanner, 2017; for review, see Pfanner et al., 2019), occurs in a different way. An important import pathway involving this class of proteins is the second *Cys-rich precursor pathway*. It describes how cysteine-rich precursor proteins destined for the mitochondrial intermembrane space IMS are imported via the TOM complex (Figure 3.1). When cysteine-carrying precursors emerge at the IMS surface of Tom40, they are recognized by a hydrophobic binding pocket of the Mia40 subunit of the mitochondrial

intermembrane space import and assembly complex MIA (Chacinska et al., 2004; Peleh et al., 2016). Here, Mia40 not only acts as a receptor for incoming precursors, but also promotes the folding of the imported precursors in the IMS (Banci et al., 2010; Peleh et al., 2016). A sulfhydryl oxidase (Erv1) cooperates with Mia40, whereby a disulfide bond generated by Erv1 is first transferred to Mia40 and then inserted into the imported protein (Mesecke et al., 2005; Rissler et al., 2005).

The third protein import pathway involving the class of proteins that do not carry cleavable presequences is the *carrier pathway*. Typical examples are the precursors of the mitochondrial metabolite carrier family, such as the inner membrane ADP/ATP carrier AAC (Truscott et al., 2002). They comprise hydrophobic proteins with six α–helical transmembrane segments. In the cytosol, the carrier precursors are initially bound to cytosolic chaperones Hsp70 and Hsp90 (Young et al., 2003). For import into mitochondria, the receptor Tom70 of the TOM complex binds both the carrier precursor and the chaperone (Brix et al., 1999). Transfer of the bound carrier from Tom70 to Tom40 channel is thought to trigger translocation across the outer membrane (Wiedemann et al., 2001). When the carrier precursor exits at the intermembrane space surface of the Tom40 channel, it is directly transferred via the small TIM molecules (Gebert et al., 2008; Lionaki et al., 2008) to the carrier translocase of the inner membrane TIM22, which drives integration into the mitochondrial inner membrane in a membrane potential dependent manner (Rehling et al., 2003).

The fourth protein import pathway involving the class of proteins that do not carry cleavable presequences is the *β-barrel pathway*. It is responsible for the incorporation of β-barrel protein precursors synthesized on the cytosolic ribosomes into the outer membrane of mitochondria. Typically, the two most C-terminal β-strands and the connecting loop of these strands constitute the targeting signal for these precursors (Jores et al., 2016). The precursors are first recognized and transported by the TOM subunit Tom40 across the mitochondrial outer membrane. When the proteins appear at the IMS side of mitochondrial outer membrane, they bind to the small TIM chaperones, which prevent them from aggregation in the IMS (for review, see Straub et al., 2016; Weinhäupl et al., 2018) and transfer them to the sorting and assembly machinery SAM (for review, see Straub et al., 2016; Weinhäupl et al., 2018). The SAM subunits Sam50 and Sam35 then mediate their folding and lateral release into the outer membrane (for review, see Wiedemann et al., 2003; Kutik et al., 2008). Biochemical crosslinking-based studies showed that the cytosolic domain of TOM subunit Tom22 transiently binds to Sam37, indicating the

dynamic formation of a TOM-SAM supercomplex to promote efficient import (Qiu et al., 2013; Wenz et al., 2015).

Eventually, the fifth protein import pathway is the *α-helical transmembrane segments pathway*. The precursor substrates following this import pathway are classified into three main types: signal-anchored proteins containing an α-helical transmembrane segment at the N terminus, tail-anchored proteins containing an α-helical transmembrane segment at the C terminus, and polytopic outer membrane proteins (for review, see Wiedemann and Pfanner, 2017). The mitochondrial import complex MIM functions here as protein insertase (Becker et al., 2008) together with Tom70 of the TOM complex (Kemper et al., 2008; Krumpe et al., 2012).

Table 3.1: Components involved in the import and sorting of nuclear-encoded precursors translocated from cytosol into the mitochondria

Component	Description	Protein substrates	Subunits
TOM	translocase of the outer membrane	all nuclear-encoded mitochondrial precursors	Tom70, Tom40, Tom22 Tom20, Tom7, Tom6, Tom5
MIM	mitochondrial import	α-helical transmembrane segments of the outer membrane	Mim1, Mim2
SAM	sorting and assembly machinery	β -barrel proteins of the outer membrane	Sam50, Sam37, Sam35, Mdm10
TIM23	translocase of the inner membrane	matrix proteins, inner membrane proteins	Tim50, Tim23, Tim21, Tim17
TIM22	translocase of the inner membrane	hydrophobic inner membrane proteins	Tim54, Tim22, Tim18, Tim12
PAM	presequence translocase	matrix proteins	Pam18, Pam16, Tim44, Mge1, mtHsp70
MPP	mitochondrial processing peptidase	proteins with N-terminal presequence	Mas1, Mas2
Small TIMs	small Tim proteins in the IMS	hydrophobic inner membrane proteins	Tim10, Tim9, Tim13, Tim8
Mia40	mitochondrial intermembrane space import and assembly	proteins of the intermembrane space	-
Erv1	essential for respiration and vegetative growth	proteins of the intermembrane space	-

3.3 Mitochondrial TOM core complex

In the previous introductory section, the five different protein import pathways into mitochondria were described. This highlighted the importance of the TOM complex in

mitochondrial biogenesis (for review, see Wiedemann and Pfanner, 2017). Therefore, the TOM complex has been the subject of many studies. Most of structural studies have been performed in baker's yeast *Saccharomyces cerevisae* (Araiso et al., 2019; Tucker and Park, 2019) and in the filamentous fungus *Neurospora crassa* (Bausewein et al., 2017, 2020). In this context, baker's yeast was particularly suitable for genetic studies since this organism was the first eukaryotic organism whose DNA was fully sequenced (Goffeau et al., 1996). *N. crassa*, in contrast to yeast, was particularly suitable, since several grams of mitochondria (Sebald et al., 1979) and milligrams of protein translocase complexes could be easily obtained from this for structural and functional studies *in vitro* (Künkele et al., 1998; Ahting et al., 1999; Poynor et al., 2008).

3.3.1 Components and atomic structure

Previous studies have shown that the TOM core complex (TOM-CC) consists of a central receptor subunit Tom22, a channel-forming β-barrel Tom40 protein, and three low molecular mass "baby" Tom proteins, designated as Tom5, Tom6 and Tom7 (Figure 3.2A) (Ahting et al., 1999; Bausewein et al., 2017; Araiso et al., 2019; Tucker and Park, 2019; Wang et al., 2020). Native mass spectrometry (Mager et al., 2010) and high-resolution electron cryo-microscopy (Cryo-EM) revealed a dimeric two-pore complex with a mass of ~148 kDa and a size of approximately 130 Å x 100 Å x 90 Å (Figure 3.2B) (Bausewein et al., 2017). Protein translocation occurs via two copies of Tom40 (Hill et al., 1998; Ahting et al., 2001), which form a 19-strand transmembrane β-barrel, each with two helical termini. The two β-barrels of the TOM core complex was found to be fully embedded in the lipid bilayer of the mitochondrial outer membrane and to bend the outer mitochondrial membrane locally towards the IMS with an average radius of approximately 140 Å (Lomize et al., 2022).

In addition to the components of the core complex, the larger TOM holo complex (Figure 3.2A) contains two receptor subunits Tom20 (Abe et al., 2000) and Tom70 (Söllner et al., 1990). Tom20 has a cytosolic domain with 5 α-helices forming one tetratricopeptide repeat (TPR) motif at its C-terminus and is anchored to the membrane via a transmembrane helix at its N-terminus. NMR studies have indicated that Tom20 interacts with the hydrophobic presequence side of precursor proteins targeted to the matrix (Abe et al., 2000), and it has been suggested that it collaborates with Tom22 in the early steps of translocation. Tom70 consists of 26 α-helices forming a large cytosolic domain with 11 TPR motifs and is also anchored to the

membrane via a transmembrane helix. Tom70 interacts in the cytosol with the chaperones Hsp70 and Hsp90 and recognizes mitochondrial preproteins with non-cleavable presequences (Wiedemann et al., 2001; Young et al., 2003). It also cooperates with the mitochondrial import protein Mim1 (Becker et al., 2011).
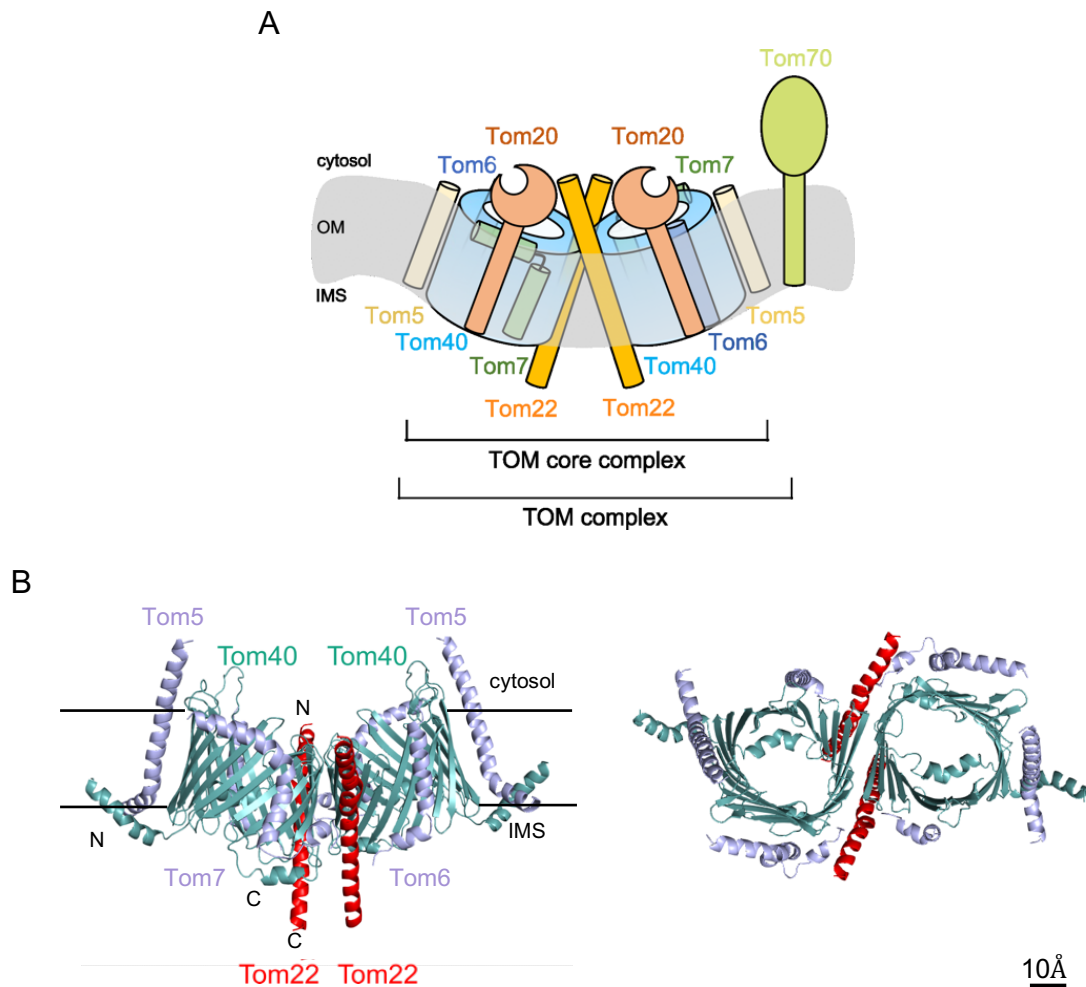
Figure 3.2: Schematic and atomic structure of N. crassa TOM complex*. A) Schematic of the TOM complex. The TOM complex consists of six receptors (2 x Tom20, 2 x Tom22 and 2 x Tom70), two protein-conducting channel proteins Tom40, and six smaller protein subunits (2 x Tom5, 2x Tom6 and 2x Tom7). The core complex (TOM-CC) lacks the receptors Tom20 and Tom70 and has total molecular mass of ~148 kDa. B) Atomic model based on the Cryo-EM map of N. crassa TOM-CC (EMDB-3761, (Bausewein et al., 2017).* left, side view; right, top view. (Label N, C terminal of Tom40)*

Tom40 is the central pore-forming unit of the TOM-CC. It is a β-barrel transmembrane protein with a molecular mass of ~38 kDa, which belongs to the voltage-dependent anion channel VDAC protein superfamily. It forms a β-barrel (Ahting et al., 2001) with 19 antiparallel β-strands (Figure 3.2B) (Bausewein et al., 2017). The shortest and largest dimensions of the

Tom40 pore are 11Å and 32Å, respectively (Bausewein et al., 2017). Two Tom40 pores in TOM-CC are not parallel with each other, but tilted by 20° relative to the 2-fold symmetric axis of the complex (Bausewein et al., 2017). The dimer interface of the Tom40 barrel is limited to only nine amino acid residues at the cytosolic side of the barrel (Bausewein et al., 2017). At the IMS side, two conserved lysine residues (Tom40-K298), contributed from each Tom40 monomer seem to destabilize the dimer (for review, see Bausewein et al., 2020). An inner α-helix in the pore is mainly used to stabilize the barrel structure, as in the case of the β-barrel protein VDAC (Naveed et al., 2009; Gessmann et al., 2011a; Teijido et al., 2012; Lipper et al., 2019). It also restricts the inner diameter of the Tom40 channel (Figure 3.2B). The N-terminus may cooperate with Tom5 to recruit the IMS-Tim9/Tim10 chaperones to TOM (Vasiljev et al., 2004). The C-terminal end of Tom40 (Figure 3.2B) may be instrumental for threading precursors through the Tom40 channel (for review, see O'Rourke, 2007; Keil et al., 1996). The pattern of hydrophobic and polar patches on the Tom40 inner channel surface (Gessmann et al., 2011b) may be helpful to maintain the unfolded state of precursors translocating through the barrel pore, such as presequence-containing precursors, cysteine-carrying precursors, C-terminal β-strand signal containing precursors and carrier precursors (for review, see Neupert and Herrmann, 2007; for review, see Straub et al., 2016; for review, see Wiedemann and Pfanner, 2017; for review, see Pfanner et al., 2019).

Tom22, with a molecular mass of ~20 kDa, contains two domains, one in the cytosol and one in the IMS, connected by a hydrophobic transmembrane helix (for review, see Walther and Rapaport, 2009; Bausewein et al., 2017). Within the complex, the two transmembrane helices of Tom22 are curved (Figure 3.2B) between the two Tom40 subunits with a total length of at least 75Å. They cross at an angle of 36° (Bausewein et al., 2017). The C-terminus of Tom22 protrudes 20 Å towards the IMS (Bausewein et al., 2017). In addition to its role as a preprotein receptor, the position of Tom22 in the complex supports the earlier hypothesis (Ahting et al., 2001) that Tom22 plays an essential role in stabilizing the TOM complex (Bausewein et al., 2017). The molecular mass of the cytosolic domains (N-termini) is 9.8 kDa each, but is not shown in the Cryo-EM structure, probably due to structural disorder caused by the many negatively charged residues (Glu) in this domain (Müller-Späth et al., 2010).

In addition to the two Tom22s wedged between the Tom40 barrels (Figure 3.2B), the TOM complex also contains two transmembrane Tom5 molecules (5.46 kDa), which are essentially straight, two Tom6 (6.33 kDa) L-shaped proteins, and two Tom7 (6.06 kDa), which are

approximately Z-shaped (Bausewein et al., 2017). Tom6 strongly interacts with Tom22 (Ahting et al., 2001) and Tom40. The Cryo-EM structure indicates that Tom6 stabilizes the interaction of Tom40 with Tom22 at the dimer interface (Bausewein et al., 2017). Tom7 is in close contact with Tom40 (Yamano et al., 2010; Bausewein et al., 2017).

3.3.2 Protein-conducting channel activity and importance of Tom22

The importance of the TOM complex in mitochondrial biogenesis has been well established by numerous studies based on the import of radiolabeled model proteins into isolated mitochondria (Lutz et al., 2003; Murschall et al., 2021). However, the biophysical mechanisms of binding and translocation of the precursor proteins remained open. Most studies that reported on the dynamic and functional properties of the TOM-CC channel itself have been based on ion current measurements through single TOM-CC channels in planar lipid membranes under application of a membrane potential (Hill et al., 1998; Künkele et al., 1998; Ahting et al., 1999; Becker et al., 2005; Mager et al., 2011; Mahendran et al., 2013; Kuszak et al., 2015). TOM-CC has been found to switch between a complex set of conductance states (Poynor et al., 2008). Although, the physiological significance of the corresponding conformational open and closed states of the TOM-CC remains controversial, as the voltage above which TOM-CC channels close is significantly higher than any potential at the outer mitochondrial membrane derived from metabolic theory (Lemeshko and Lemeshko, 2000), it has been suggested that Tom22 adds flexibility to the complex by reducing the energy required for transitions between these states (Poynor et al., 2008; Romero-Ruiz et al., 2010). Other electrophysiology studies (van Wilpe et al., 1999) have suggested that the TOM channels of *S. cerevisiae* mitochondria are mainly in closed states, while TOM lacking Tom22 has been found mainly in open states, similar to that of Tom40 (Hill et al., 1998; van Wilpe et al., 1999; Ahting et al., 2001). It has therefore been postulated that Tom22 negatively regulates the opening probability of TOM (van Wilpe et al., 1999). However, the molecular mechanism of how Tom22 influences the activity of the open-closed channels of the TOM machinery has remained an open question. In this context, it also remained unclear how possible interactions of TOM with components of the inner mitochondrial membrane, such as TIM23, Tim9/Tim10 or TIM22 (Figure 3.1), affect the open-closed state of its Tom40 pores during protein import.

3.4 Lateral organization and mobility of membrane proteins

The lateral organization of membrane proteins is often regulated by interactions with other membrane proteins, peripheral structures, and lipid composition (for review, see Sezgin et al., 2017). An example of the latter is the HIV glycoprotein subunit gp41, which has cholesterol-binding motifs (Checkley et al., 2011; Schwarzer et al., 2014). Moreover, length mismatch between the transmembrane protein domains and surrounding lipids, as shown for SNARE proteins (Milovanovic et al., 2015), induces membrane protein aggregation in the membrane (Lang et al., 2001; Schmidt and Weiss, 2010; Kaiser et al., 2011). In addition, actin filaments coupled to lipid species via membrane adaptor proteins can induce the formation of locally ordered lipid domains (Liu and Fletcher, 2006; Gowrishankar et al., 2012; Fritzsche et al., 2017), which results in the immobilization of long acyl chain-containing lipid-anchored proteins (e.g. glycosylphosphatidylinositol (GPI)-anchored proteins such as *Trypanosoma brucei* variant surface glycoprotein VSG and rat brain Thy-1 (Krakow et al., 1986; Rege and Hagood, 2006; Paulick and Bertozzi, 2008; Saha et al., 2015; Fujiwara et al., 2016)). Finally, non-reversible or reversible palmitoylated proteins, such as postsynaptic density protein 95 (Tulodziecka et al., 2016) and membrane palmitoylated protein 1 (Podkalicka et al., 2015), are recruited to lipid raft domains (for review, see Greaves et al., 2009; Levental et al., 2010; Tulodziecka et al., 2016).

The lateral mobility of membrane proteins, which is related to the local dynamic composition and structure of the membrane, is important for predicting the outcome of membrane-based reactions (Zhang et al., 1993; for review, see Nicolson, 2014; for review, see Sezgin et al., 2017). Previous microscopic single-molecule tracking studies (for review, see Kusumi et al., 2012; Sanderson, 2012) have shown that the lateral movement of integral membrane proteins in biological membranes is not always freely diffusive following purely Brownian motion. Five different types of lateral protein mobility in biological membranes have been described: (i) free diffusion, (ii) hop diffusion, (iii) transient or permanent anchorage (no mobility), (iv) channel diffusion and (v) directed motion (for review, see Jacobson et al., 2019). Free lateral movements of integral membrane proteins in the plasma membrane can be restricted by lipid and protein clusters in the membrane (Kusumi et al., 1993, 2012) or by the interaction of the proteins with components of the intracellular cytoskeletal filament network or the extracellular matrix (Edidin, 1992; Kusumi et al., 1993, 2012) resulting in transient or permanent anchorage. Restriction of integral membrane proteins was found to create membrane regions with a high density of supramolecular protein complexes, which improve the efficiency of signal

transduction (Zhang et al., 1993; for review, see Kusumi et al., 2011, 2012; for review, see Jacobson et al., 2019). This includes, for example, GPI-anchored proteins associated with receptor tyrosine kinases (RTKs) (Štefanová et al., 1991; Davy et al., 1999) and SecA-SecYEG supercomplexes (Mori and Ito, 2006; Winkler et al., 2020) involved in developmental process and protein translocation, respectively. A similar finding could also apply to the mitochondrial protein translocases TOM, SAM, TIM23, and TIM22 (Figure 3.1) when forming supercomplexes in mitochondrial contact sites (for review, see Pfanner et al., 2019; Scorrano et al., 2019), as already indicated by biochemical crosslinking studies for TOM-SAM (Qiu et al., 2013; Wenz et al., 2015), TOM-TIM23 (Sharma et al., 2007) and TOM-TIM22 (Kang et al., 2016).

The latter experiments indicated that the TOM complex of the outer membrane of mitochondria does not act as an independent entity, but in a network of interacting protein complexes, which transiently cluster in mitochondrial outer- and inner-membrane contact sites (for review, see Pfanner et al., 2019; Scorrano et al., 2019). For proteins destined for integration into the lipid bilayer of the inner mitochondrial membrane, TOM transiently cooperates with components of the inner membrane protein translocase TIM22. Proteins *en route* to the mitochondrial matrix require supercomplex formation with the inner membrane protein translocase TIM23 (Chacinska et al., 2005; Mokranjac et al., 2009). Depending on the activity of mitochondria, the lateral organization and the possibility of the respective repositioning of TOM, TIM22 and TIM23 in the outer and inner mitochondrial membranes to form transient contact sites may therefore be of fundamental importance for the different import requirements of the organelle (for review, see Pfanner et al., 2019). The mobility of the main TIM23 subunit Tim23, with a low diffusion constant D_{Tim23} of about 0.06 $\mu m^2 s^{-1}$, is significantly lower than that of freely diffusing Tom40 ($D_{\text{Tom40}} \sim 0.5\ \mu m^2\ s^{-1}$) (Kuzmenko et al., 2011; for review, see Appelhans and Busch, 2017) and Tom20 ($D_{\text{Tom20}} \sim 0.3\ \mu m^2\ s^{-1}$) (Bhagawati et al., 2021) indicating an anchoring of the TIM23 complex in the mitochondrial inner membrane. Therefore, one could assume that the TOM machinery is temporarily immobilized by TIM23 when the TOM-TIM23 supercomplexes are formed. How such immobilization would affect the channel activity of the TOM machinery was one of the main questions and the subject of the present work, which was to be investigated in a defined experimental *in vitro* system without external artificial membrane potentials.

3.5 Aim of this study

The overall aim of the present research work was to investigate whether and how lateral membrane protein movement affects the channel permeability of the TOM-CC in a well-defined *in vitro* membrane system. This should provide new insights into the spatiotemporal dynamics of the TOM-CC that cannot be captured by single-molecule electrophysiology or structural work. The results may help to further elucidate the role of TOM-CC motion in the outer mitochondrial membrane and the mechanism of protein translocation across the outer mitochondrial membrane *in vivo*. To achieve this goal, the following three sub-projects and questions have been addressed:

i. Design of an optical TIRF setup that allows the investigation of the biophysical properties of single-molecule TOM-CC channels in supported lipid membranes without the need to apply artificial membrane voltages (results section 5.1). This includes a detailed description of how TOM-CC is isolated from *N. crassa* mitochondria, how the complex is fluorescently labeled, and how induced TOM-CC molecules are functionally integrated into DIB membranes. The latter should be demonstrated by single-molecule FRET between fluorescently labeled TOM-CC and mitochondrial presequence proteins.

ii. The second goal is to optically visualize the channel activity of single TOM-CC in supported lipid bilayers and to unravel how the channel activity correlates with the lateral movement of the complex in the membrane (results section 5.2). To this end, both channel activity and single-molecule membrane protein diffusion will be studied simultaneously using single-molecule TIRF microscopy.

iii. Based on the observations made in (2), the components affecting the lateral motion and channel opening of the TOM-CC should be determined and discussed on a molecular and mechanistic level (results section 5.3). For this, the channel activity of immobilized and non-immobilized TOM-CC molecules should be compared with that of monomeric Tom40, trimeric OmpF and α-hemolysin channels.

4 Materials and Methods

All chemicals were purchased from Roth (Germany), Merck (Germany), and Sigma Aldrich (Germany), except for those listed in Table 4.1.

Table 4.1: Specific chemicals used in this work and their commercial sources

Chemical	Provider	Country
n-dodecyl-β-D-maltoside (DDM)	Glycon Biochemicals	Germany
n-octyl β-D-glucopyranoside (OG)	Glycon Biochemicals	Germany
n-octyl polyoxyethylene (Octyl-POE)	Bachem	Switzerland
Cy3-maleimide	AAT Bioquest	USA
Cy5-maleimide	AAT Bioquest	USA
1,2-diphytanoyl-sn-glycero-3-phosphocholine	Avanti Polar Lipids	USA
Ni-NTA-modified agarose	Cube Biotech	Germany
Chelex resin	Bio-Rad	Germany
Fluo-8 sodium salt	Santa Cruz Biotechnology	USA
Immunoglobulin G	Bio-Rad	Germany
BioRad Protein assay	Bio-Rad	Germany
Tetramethylethylenediamine	Thermo Fisher	Germany
Ammonium persulfate	Thermo Fisher	Germany

4.1 Cell culture

4.1.1 *N. crassa* cultivation

For the biophysical characterization of TOM core complex, TOM-CC was isolated from the filamentous fungus *Neurospora crassa* (*N. crassa,* strain GR-107) (Künkele et al., 1998), which contains a hexahistidinyl-tagged form of Tom22.

Silicate dried *N.crassa* T107 conidia (Künkele et al., 1998) were used to inoculate complete medium agar (Table 4.2) in a sterilized conical flask (primary culture A). The conidia were incubated at 30 °C for two days in the dark and then incubated at room temperature for five days in daylight. The grown conidia from this primary culture A were either used to inoculate additional sterile flasks B ($N = 20$) and cultured in the same manner as primary culture A or to produce new silicate stocks. For the latter, conidia were resuspended in 50 mL 100 g/L skim milk in sterile water. Afterwards, this suspension was filtered through sterile filter paper, and

aliquots of ~300 µL filtrate were mixed with 1g sterile silicate. This solution was dried in an exicator at room temperature for three weeks and eventually stored at 4 °C.

Table 4.2: *N. crassa* **growth media**

	Reagent concentrations
Trace elements solution [1]	50 g/L Citric acid
	50 g/L $ZnSO_4$
	10 g/L $FeNH_4SO_4$
	2.5 g/L $CuSO_4$
	0.5 g/L $MnSO_4$ x H_2O
	0.5 g/L H_3BO_3
	0.5 g/L Na_2MoO_4
Biotin solution [1]	50 % (v/v) Ethanol
	0.01 % (v/v) Biotin
Histidine solution [1]	20 g/L L-Histidine
Sucrose solution [1]	500 g/L Sucrose
50x Vogel's minimal medium [1]	150 g/L Na_3-Citrate x $2H_2O$
	250 g/L KH_2PO_4
	100 g/L NH_4NO_3
	10 g/L $MgSO_4$
	5 g/L $CaCl_2$
	0.005 % (v/v) Trace elements solution
	0.0025 % (v/v) Biotin solution
Vitamin solution [1]	20 mg/L Vitamin B1
	10 mg/L Vitamin B2
	10 mg/L Vitamin B6
	10 mg/L *p*-aminobenzoic acid
	10 mg/L Nicotinamide
	200 mg/L Choline chloride
	2 mg/L Folic acid
	200 mg/L Inositol
	100 mg/L Calcium-D-pantothenate
Complete medium agar	2 % (v/v) 50x Vogel's minimal medium [1]
	1 % (v/v) Vitamin solution [1]
	1 % (v/v) Histidine solution [1]
	1 % (v/v) Glycerol [2]
	15 g/L Sucrose [2]
	2 g/L Yeast extract [2]
	1 g/L Casein hydrolysate [2]
	20 g/L Agar [2]

[1] sterilized by filtration, [2] sterilized by autoclaving

To obtain a large amount (> 1 kg) of *N. crassa* hyphae, conidia were collected from 10 conical flasks B in distilled water under sterile conditions and transferred to an 8 L solution containing 2 % (v/v) 50x Vogel's minimal medium (Table 4.2), 4 % (v/v) sucrose solution (Table 4.2) and 1 % (v/v) histidine solution (Table 4.2), where the conidia grew for 8 hours at 25 °C with aeration and light. Subsequently, this culture was diluted to 80 L solution containing 2 % (v/v) 50x Vogel's minimal medium, 4 % (v/v) sucrose solution and 1 % (v/v) histidine solution and

incubated for 16 hours under the same growth conditions. To harvest the *N. crassa* hyphae, the culture was sedimented in a large volume custom-built centrifuge (> 10 L). Finally, the wet weight of the hyphae was determined and either stored at -20 °C or used immediately to isolate mitochondria.

4.1.2 *Escherichia coli* cultivation

Table 4.3: *E. coli* growth media

	Reagent concentrations
LB medium	10 g/L Tryptone
	10 g/L NaCl
	5 g/L Yeast extract [1]
LB plate	20 g/L Bacto-agar
	100 % (v/v) LB medium
	100 µg/L Ampicillin (Na salt)
	30 µg/L Kanamycin sulfate

[1] sterilized

Escherichia coli strain BE BL21(DE3)omp6, lacking both LamB and OmpC (Bieligmeyer et al., 2016), was recovered from a frozen glycerol stock and streaked onto a Luria-Bertani (LB) plate (Table 4.3). 7.5 mL LB medium (Table 4.3) was inoculated with a single colony and *E.coli* were grown overnight (12 - 14 h) with agitation (170 rpm) at 37 °C. Then, 2 x 1 mL of cells were transferred into 2 x 500 mL LB medium, respectively, and grown overnight (12 - 14 h) with agitation (170 rpm) at 37 °C. The cells were harvested by centrifugation at 5,000 x g for 20 min at 4 °C and the pellet was frozen in liquid nitrogen and stored at -80 °C until further use. The wet weight of the cell pellet was typically ~5 g per 1 L culture.

4.2 Biochemical methods

4.2.1 Isolation of mitochondria from *N. crassa*

Approximately 1.5 kg (wet weight) of *N. crassa* hyphae (section 4.1.1) was homogenized in a Waring mixer at 4 °C with ~2 L SET buffer (Table 4.4). 1.5 kg of sea sand was added, and the suspension was passed through a corundum stone mill to break up the cell walls. Unbroken cells and sea sand were sedimented and discarded by a centrifugation step at 3,000 x g for 5 minutes at 4 °C. This centrifugation step was repeated twice. Mitochondria in the supernatant were sedimented at 17,700 x g for 80 minutes. The isolated mitochondria were then scratched out from the inner wall of the centrifuge bottle with a spatula and homogenized by using a glass

Table 4.4: Mitochondria isolation buffer

	Reagent concentrations
SET buffer	250 mM Sucrose
	2 mM EDTA
	20 mM Tris-HCl pH 8.5
	1 mM Phenylmethylsulfonyl fluoride (PMSF)
ST buffer	250 mM Sucrose
	20 mM Tris-HCl pH 8.5

Teflon homogenizer after addition of 50 mL SET buffer. This centrifugation step was repeated. The isolated mitochondria were suspended in ST buffer (Table 4.4) with a final protein concentration of 50 mg/mL, flash frozen in liquid nitrogen and stored at -20 °C until further use.

4.2.2 Purification of TOM core complex from mitochondria

Table 4.5: TOM core complex purification buffer

	Reagent concentrations
Solubilization buffer	1 % (w/v) n-dodecyl-β-D-maltoside
	20 % (v/v) Glycerol
	300 mM NaCl
	20 mM Imidazole-HCl
	20 mM Tris-HCl (pH 8.5)
	1 mM PMSF
Equilibration buffer	0.1 % (w/v) n-dodecyl-β-D-maltoside
	10 % (v/v) Glycerol
	300 mM NaCl
	20 mM Tris-HCl (pH 8.5)
	1 mM PMSF
TOM-CC elution buffer	0.1 % (w/v) n-dodecyl-β-D-maltoside
	10 % (v/v) Glycerol
	20 mM Tris-HCl (pH 8.5)
	1 mM PMSF
	1 M Imidazole-HCl
ResQ buffer1	20 mM HEPES (pH 7.2)
	2 % (v/v) Dimethyl sulfoxide
	0.1 % (w/v) n-dodecyl-β-D-maltoside
ResQ buffer2	20 mM HEPES (pH 7.2)
	2 % (v/v) Dimethyl sulfoxide
	0.1 % (w/v) n-dodecyl-β-D-maltoside
	1 M KCl

TOM-CC was purified according to (Bausewein et al., 2017). Briefly, 2g *N. crassa* mitochondria (section 4.2.1) were solubilized in 200 mL solubilization buffer (Table 4.5) at a protein concentration of 10 mg/mL and stirred at 4 °C for 30 min. The non-solubilized membranes were separated from the solubilized membrane proteins by ultracentrifugation at

130,000 x g (rotor: Ti70) for 40 min at 4 °C and filtration through standard grade filter paper. A prepacked 5 mL Ni-NTA column (Cytiva, Germany) was equilibrated with approximately 5 column volumes (CV) of equilibration buffer (Table 4.5) by using an automated protein purification system (Äkta, Cytiva, Germany). The solubilized protein sample was loaded onto the Ni-NTA column (flow rate of 1 mL/min). The column was rinsed with ~5 CV equilibration buffer to remove unbound proteins. The TOM core complex was eluted with 30 % TOM-CC elution buffer (Table 4.5, 300 mM imidazole). For further purification, a pre-packed Resource Q anion exchange column (1 mL, Cytiva, Germany) was equilibrated with 5 CV each of ResQ buffer 1, ResQ buffer 2, and ResQ buffer 1 (Table 4.5) using an automated protein purification system. The anion exchange column was run at a constant flow rate of 1 mL/min in all steps. The Ni-NTA column peak fraction containing TOM-CC was loaded onto the anion exchange column. Unbound proteins were removed by rinsing the column with ~5 CV of ResQ buffer1 and a linear salt gradient of 0 to 22 % ResQ buffer2. The TOM core complex was eluted with a linear salt gradient of 22 to 40 % ResQ buffer2. The purity of protein samples (0.4 - 1.2 mg/mL) was assessed by sodium dodecyl sulfate polyacrylamide gel electrophoresis (SDS-PAGE) followed by staining with Coomassie Brilliant Blue. Protein samples were flash frozen in liquid nitrogen and stored at -20 °C until further use.

4.2.3 Purification of Tom40 from mitochondrial outer membranes

Table 4.6: Tom40 purification buffer

	Reagent concentrations
Tom40 elution buffer	3 % (w/v) n-octyl β-D-glucopyranoside 2 % (v/v) Dimethyl sulfoxide 20 mM Tris-HCl (pH 8.5)
A1 buffer	1 % (w/v) n-octyl β-D-glucopyranoside 2 % (v/v) Dimethyl sulfoxide 20 mM Tris-HCl (pH 8.5) 300 mM Imidazole-HCl
A2 buffer	1 % (w/v) n-octyl β-D-glucopyranoside 2 % (v/v) Dimethyl sulfoxide 20 mM Tris-HCl (pH 8.5) 1 M Imidazole-HCl

For the isolation of Tom40 (Ahting et al., 2001), isolated mitochondria of *N. crassa* strain GR-107 were solubilized at a protein concentration of 10 mg/mL in 200 mL solubilization buffer (Table 4.5) for 30 min with stirring at 4°C. After centrifugation at 130,000 x g for 40 min at 4 °C, the clarified extract was filtered and loaded onto a 5 mL Ni-NTA column (Cytiva, Germany). The column was washed with equilibration buffer (Table 4.5), and Tom40 was

eluted directly with Tom40 elution buffer (Table 4.6), which contains octyl-glucoside and dissociates the TOM-CC into its subunits. The specifically bound proteins (e.g., Tom22) were sequentially eluted with A1 buffer and A2 buffer (Table 4.6). The purity of the isolated Tom40 protein ($\sim$0.3 mg/mL) was assessed by SDS-PAGE. Protein samples were flash frozen in liquid nitrogen and stored at -20 °C until further use.

4.2.4 Purification of OmpF from *E. coli*

Table 4.7: OmpF purification buffer

	Reagent concentrations
Lysis buffer	2 mM MgCl$_2$
	$\sim$750 units DNAse
	50 mM Tris-HCl (pH 7.5)
Tris-HCl	50 mM Tris-HCl (pH 7.5)
SDS buffer1	4 % (w/v) Sodium dodecyl sulfate
	2 mM β-mercaptoethanol
	50 mM Tris-HCl (pH 7.5)
SDS buffer2	2 % (w/v) Sodium dodecyl sulfate
	500 mM NaCl
	50 mM Tris-HCl (pH 7.5)
Dialysis buffer	20 mM Tris (pH 8.5)
	1 mM EDTA
	0.5 % (w/v) octyl-polyoxyethylene

$\sim$5 g Cells from 1 L culture were suspended in 20 mL lysis buffer (Table 4.7) and broken by suspension three times passing through a pre-cooled (4 °C) French press at 1.000 psig (Bieligmeyer et al., 2016). Unbroken cells were removed at 4,000 x g (rotor: SA-300) centrifugation for 15 min at 4 °C. Then the supernatant was centrifuged at 100,000 x g (rotor: Ti70) for 1 h at 4 °C to collect membranes. The membrane pellet was resuspended in 10 mL Tris-HCl (Table 4.7) by a ball-bearing glass-glass homogenizer, then mixed with an equal volume of SDS buffer1 (Table 4.7). After incubation in a 50 °C water bath for 30 minutes, the solution was centrifuged at 100,000 x g for 1 h at 20 °C. The pellet was resuspended in SDS buffer2 (Table 4.7) by a ball-bearing glass-glass homogenizer, then incubated in a 37 °C water bath for 30 min and centrifuged again with 100,000 x g for 30 min at 20 °C. OmpF were obtained from the supernatant. Finally, the OmpF-containing supernatant mixed with 5 g/L n-octyl polyoxyethylene (Octyl-POE) was dialyzed twice against dialysis buffer (Table 4.7) overnight at 4 °C using dialysis tubing with a cut-off of 20 kDa. The purity of the isolated protein ($\sim$1.0 mg/mL) was assessed by SDS-PAGE. Dialyzed protein samples were flash frozen in liquid nitrogen and stored at -20 °C until further use.

4.2.5 Fluorescence labeling of TOM core complex

Table 4.8: TOM core complex fluorescence labeling buffer

	Reagent concentrations
FL buffer [1]	20 mM HEPES (pH 7.2)
	2 % (v/v) Dimethyl sulfoxide
	350 mM KCl
	0.1 % (w/v) n-dodecyl-D-maltoside

[1] degassed before use

Fluorescent labeling of TOM-CC containing a 6xHis tag at Tom22 (section 4.2.2) with fluorescent dye Cy3-maleimide was performed according to (Joo and Ha, 2008). To this end, 500 μL Ni-NTA resin (Thermo Fisher, Germany) was washed with double deionized water (~5 CV) in a gravity flow column (2 mL bed volume, Bio-Rad, Germany) and then equilibrated with ~5 column volumes FL buffer (Table 4.8). Approximately 1 mg of purified TOM-CC (1 mg/mL) was loaded onto the equilibrated 500 μL Ni-NTA resin and washed with 8 CV of FL buffer at 4 °C. FL buffer containing 0.1 mM Tris (2-carboxyethyl) phosphine TCEP was added to the column, incubated for 10 min at room temperature, and washed with 20 CV of FL buffer at 4 °C. Next, the mixture of TOM-CC and Ni-NTA resin was removed from the column and transferred to an Eppendorf tube. Cy3 maleimide in FL buffer was added to the TOM-CC bound to the Ni-NTA resin at a 1:5 molar ratio of complex to dye. To avoid oxidation, the top of the Ni-NTA resin was covered with N_2 gas. After 2 hours of reaction labeling at room temperature in the dark, Cy3-labeled TOM-CC molecules were separated from unconjugated Cy3-maleimide dye by washing the Ni-NTA resin 5 times with 4 CV FL buffer. Finally, the Cy3-labeled-TOM-CC molecules were eluted with 1CV FL buffer containing 300 mM imidazole. The purity of Cy3-labeled-TOM-CC protein (~0.5 mg/mL) was assessed by SDS-PAGE, and first visualized by 555 nm light and then by Coomassie Brilliant Blue staining. Fluorescently labeled protein samples were flash frozen in liquid nitrogen and stored at -20 °C until further use.

4.2.6 Fluorescence labeling of mitochondrial presequence protein

Mitochondrial presequence protein (Su9-MBP, courtesy Pamela Ornelas, MPI Biophysics, Frankfurt) was covalently labeled with the fluorescent dye Cy5-maleimide according to (Joo and Ha, 2008). The mitochondrial presequence protein (1 mL, 1 mg/mL) was initially treated with 0.1 mM TCEP for 10 mins at room temperature. Then, mitochondrial presequence protein was reacted with Cy5-maleimide in FL buffer (Table 4.9) at a 1:5 molar ratio of complex to dye

Table 4.9: Mitochondrial presequence protein fluorescence labeling buffer

	Reagent concentrations
FL buffer [1]	20 mM HEPES (pH 7.2)
	50 mM KCl

[1] degassed before use

for 2 h at room temperature in the dark. This chemical reaction was carried out in an Eppendorf tube which was covered with N_2 gas at the top. To remove the unconjugated Cy5-maleimide dyes from the Cy5-labeled protein, a PD-10 desalting column (8.3 mL bed volume, GE Healthcare, Germany) was firstly equilibrated with 4 CV of FL buffer (Table 4.9). Afterwards, the mixture of Cy5-labeled protein, the unconjugated Cy5-maleimide dyes and 1.5 mL FL buffer was loaded onto an equilibrated PD-10 desalting column. Cy5-labeled protein eluted first according to the manufacturer's protocol at an elution volume of ~3.5 mL. The purity of the Cy5-labeled- protein (~1.0 mg/mL) was assessed by SDS-PAGE, and visualized by 638 nm light and Coomassie Brilliant Blue staining. Fluorescently labeled protein samples were flash frozen in liquid nitrogen and stored at -20 °C until further use.

4.2.7 Determination of protein concentration with the Bradford method

The concentration of unknown protein samples was determined as described by (Bradford, 1976) using immunoglobulin G as calibration standard (Table 4.1). Protein samples and calibration standards (mg/mL: 0, 0.17, 0.34, 0.68, 1.36) were prepared in triplicate in a final volume of 35.3 μL before adding 1 mL of BioRad protein assay (Table 4.1) reagent. The samples were incubated for 10 min at room temperature before measuring the absorbance at 595 nm. The measured absorbance of the protein sample was compared to the calibration curve to determine the concentration of the protein sample using customized software.

4.2.8 Protein gel electrophoresis

To cast acrylamide gels for SDS-PAGE, two glass plates and spacers were cleaned with 70 % ethanol and mounted on a gel casting apparatus (8 x 6 cm and spacers of 0.7 mm, Bio-Rad, Germany). After adding APS and TEMED to the separating gel buffer (Table 4.10) to induce acrylamide polymerization, the separating gel buffer was poured between the two glass plates in the SDS-PAGE apparatus (Bio-Rad, Germany) until it reached three-quarters of the height of the glass plates. Isopropanol was then poured over the separating gel buffer. After 30 minutes

and complete acrylamide polymerization, the isopropanol was removed. A 10-pocket comb was inserted between two glass plates, and the stacking gel buffer (Table 4.10) was poured to the top of the glass plates. After complete polymerization of the stacking gel buffer, the cast gels were wrapped in wet paper towels and stored at 4 °C until use.

Table 4.10: Protein gel electrophoresis buffer

	Reagent concentrations
Separating gel buffer	14 % (v/v) Acrylamide/bis-acrylamide (37.5:1)
	375 mM Tris-HCl (pH = 8.8)
	0.1% (w/v) Sodium dodecyl sulfate SDS
	1 % (v/v) Ammonium persulfate APS [1]
	0.1 % (v/v) Tetramethylethylenediamine TEMED [1]
Stacking gel buffer	3.9 % (v/v) Acrylamide/bis-acrylamide (37.5:1)
	125 mM Tris-HCl (pH = 6.8)
	0.1 % (w/v) Sodium dodecyl sulfate SDS
	1 % (v/v) Ammonium persulfate APS [1]
	0.1 % (v/v) Tetramethylethylenediamine TEMED [1]
4x Laemmli buffer	40 % (v/v) glycerol
	0.4 g/L Bromphenolblue
	4 % (v/v) β-mercaptoethanol
	8 % (w/v) Sodium dodecyl sulfate SDS
	250 μm Tris-HCl (pH 7.6)
1x Running buffer	0.1 % (w/v) Sodium dodecyl sulfate SDS
	3 g/L Tris-HCl (pH 7.6)
	14.4 g/L Glycine
Coomassie Blue	2.5 g/L Coomassie brilliant blue R-250
	45 % (v/v) Ethanol
	10 % (v/v) Acetic acid
	45 % (v/v) mL Double deionized water
Destaining buffer	26 % (v/v) Ethanol
	8 % (v/v) Acetic acid
	66 % (v/v) Double deionized water

[1] add only to initiate acrylamide polymerization

According to the method of (Laemmli, 1970), the separation of protein samples was then performed based on their different molecular mass. 5 μL 4x Laemmli buffer (Table 4.10) was added to 15 μL protein sample, and it was heated at 90 °C for 5 min. The protein samples were then loaded on SDS acrylamide gel, and electrophoresis was performed in 1x running buffer (Table 4.10) at 25 mA and 200 V per SDS acrylamide gel. To visualize the purity of protein samples, the gel was stained with Coomassie Brilliant Blue (Table 4.10) for 1 h and destained with destaining buffer (Table 4.10) for another 1 h.

4.3 Formation of droplet interface bilayers

Droplet interface bilayer (DIB) membranes were prepared as previously described (Leptihn et al., 2013; Huang et al., 2015) with minor modifications as outlined in Figure 4.1.

Table 4.11: Droplet interface bilayers formation buffer

	Reagent concentrations
Lipid/Oil solution	9.5 mg/mL 1,2-diphytanoyl-sn-glycero-3-phosphocholine 50 % (v/v) Hexadecane 50 % (v/v) Silicon oil AR20
2.5 % agarose solution without imidazole	25 mg/mL Low melting agarose 0.66 M $CaCl_2$ 8.8 mM HEPES (pH 7.2)
2.5 % agarose solution with imidazole	25 mg/mL Low melting agarose 0.66 M $CaCl_2$ 8.8 mM HEPES (pH 7.2) 300 mM Imidazole-HCl
Droplet buffer [1]	7 µM Fluo-8 sodium salt 400 µM EDTA 8.8 mM HEPES (pH 7.2) 1.32 M KCl ~27 nM Transmembrane protein (TOM-CC, Tom40, OmpF, α-Hemolysin)

[1] The double deionized water used for the droplet buffer was treated with Chelex resin (Wang et al., 2018) for ~2 days to scavenge residual Ca^{2+} that could interfere with Fluo-8 calcium signaling.

4.3.1 Preparation of lipid solutions

Lipid stock solution containing 1,2-diphytanoyl-sn-glycero-3-phosphocholine (25 mg/mL DPhPC) dissolved in chloroform was removed from the freezer at -20 °C and warmed to room temperature. A microliter Hamilton glass syringe with stainless steel plungers (Merck, Germany) was washed three times with methanol and subsequently three times with chloroform. 380 µL DPhPC stock solution was transferred into a glass vial and then dried under a stream of N_2. Afterwards, residual organic solvent was removed overnight under vacuum (2.0 mbar) using an oil-free vacuum pump. The lipid film was dissolved in a hexadecane/silicone oil solution by adding equal volumes of hexadecane and silicone oil (500 µL each) to a final lipid concentration of 9.5 mg/mL (Table 4.11).

4.3.2 Preparation of agarose hydrogels

To prepare the hydrogel for DIB membranes, 0.75 % (w/v) low-melting agarose (Tm < 65 °C, Sigma-Aldrich) or alternatively 50 % (w/v) low-melting agarose modified with Ni-NTA was heated at 85 °C for ∼20 min or at 95 °C overnight, respectively. In addition, a 2.5 % agarose solution (Table 4.11) with or without imidazole was heated at 85 °C for ∼20 min.

4.3.3 Preparation of clean glass coverslips

Glass coverslips (40 mm x 24 mm x 0.13 mm, Roth, Germany) were cleaned in acetone in an ultrasonic bath for 10 min, rinsed several times with deionized water and dried under a stream of N_2. The glass coverslips were then subjected to plasma cleaning under 0.5 mbar oxygen for 5 minutes.

4.3.4 Assembly of DIB chamber

140 µL of melted 0.75 % (w/v) low melting point unmodified agarose or alternatively 50 % (w/v) low melting point Ni-NTA modified agarose was spun at 3,000 rpm for 30 s onto the plasma cleaned surface of a glass coverslip (Figure 4.1, Step 1). The coverslip was placed in the PMMA chamber (Figure 4.1, step 2), and the edges of the coverslip were fixed with adhesive tape (Figure 4.1, step 2). 200 µL of a 2.5 % agarose solution without imidazole or with imidazole (Table 4.11) was carefully poured into the inlet of the chamber with a pipette on a 35 °C hot plate (Figure 4.1, step 3), so that the thin hydrogel applied by spin coating could equilibrate with the buffer of the 2.5 % agarose solution and remained hydrated.

The wells of the PMMA chamber (Figure 4.1, step 4, right) were then immediately covered with a total of ∼60 µL of lipid/oil solution to initiate lipid monolayer formation at the agarose-oil interface and to avoid dehydration of the spin-coated agarose in the wells of the PMMA chamber. Lipid hexadecane/silicone oil solution was placed into microfabricated recesses in a PMMA droplet incubation chamber (Figure 4.1, step 4, left).

A microcapillary glass needle was filled with ∼5 µL injection droplet buffer (Table 4.11) and mounted on a piezo-driven Nanoliter 2000 injector (World Precision Instruments). Aqueous droplets (~200 nL) were injected into the lipid/oil solution in the droplet incubation chamber (Figure 4.1, step 4, left). Formation of a lipid monolayer at the droplet-oil interface was enabled

by holding the PMMA chamber and droplet incubation chamber (Figure 4.1, step 4) at 35 °C for ~2 h. Individual aqueous droplets (Figure 4.1, step 5) were then transferred into the wells of the PMMA chamber using a 10 µL pipette to initiate the formation of the lipid bilayer (Figure 4.1) between the droplet and the agarose hydrogel.
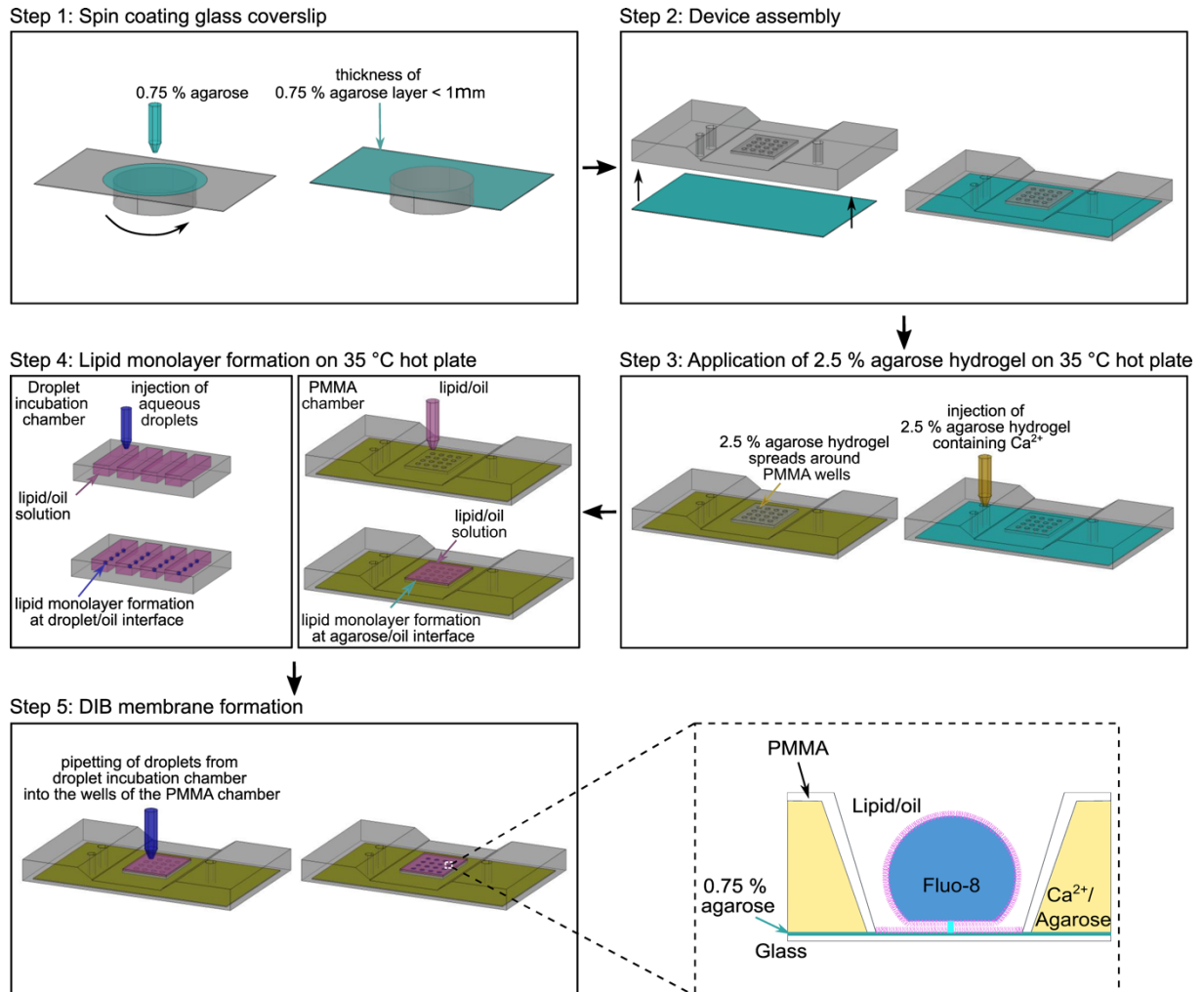

Figure 4.1: Flow chart of PMMA chamber assembly and DIB membrane formation. *Step 1: A glass coverslip is spin-coated with an 0.75 % agarose hydrogel. Step 2: The spin- coated coverslip is mounted in a custom-made PMMA microscopy chamber. Step3: 2.5 % low melt agarose solution is added into the inlet port of the PMMA chamber on a 35 °C hot plate. Step 4: Lipid monolayers are formed around aqueous droplets at a buffer/oil interface (left) and on the agarose hydrogel/oil interface (right). Step 5: Individual aqueous droplets are pipetted into the wells of the PMMA chamber to form a lipid bilayer upon the contact of the two lipid monolayers. Dark green, 0.75 % agarose; yellow, 2.5 % agarose containing Ca^{2+} ions; magenta, lipid/oil phase; pink, lipid; dark blue, aqueous droplet buffer containing Ca^{2+}-sensitive dye and protein; cyan, transmembrane protein reconstituted into the DIB membrane.*

4.4 Microscopic techniques

4.4.1 Atomic force microscopy

To assess the thickness and texture of the hydrogel agarose films used for DIB production, glass coverslips were prepared as described in section 4.3 and imaged in deionized water using a Nanoscope 5 multimode-8 AFM system with SNL-10 cantilevers (Bruker) in tapping mode.

4.4.2 Hoffmann modulation contrast microscopy

After transferring droplets from the droplet incubation chamber into the wells of the custom-made PMMA chamber (section 4.3), the formation of self-assembled lipid bilayers was examined using Hoffmann modulation contrast microscopy (Eclipse TS100 Nikon) under a 10 x MC1 HMC N.A. 0.25 objective (Nikon). DIB membrane images were captured with a color video camera (TK-C9511EG, 752 x 582 Pixels, JVC).

4.4.3 Total internal reflection fluorescence microscopy

4.4.3.1 Imaging Ca^{2+}-flux through individual protein channels in droplet interface bilayer membranes

Using total internal reflection inverted fluorescence microscopy (Ti-E Nikon, Figure 4.2), Ca^{2+} ion flux through transmembrane protein channels reconstituted into the DIB membrane was measured by monitoring the fluorescence emission of the Ca^{2+}-sensitive dye Fluo-8 under a 488 nm laser (P_{max} = 100 mW, Visitron). For this purpose, a microfabricated PMMA chamber containing DIB membranes (section 4.3) was mounted in a microscope specimen holder and the edge of a DIB membrane was focused using a 10 x N.A.0.25 air objective (Nikon) under epifluorescence illumination with a GFP filter set (AHF). The same edge of the DIB membrane was finely focused with a 100 x oil immersion TIRF objective (Apochromat N.A.1.49, Nikon) under the same microscopy settings. Subsequently, the DIB membranes (Fluo-8) were visualized under 488 nm laser light (8 - 10 mW) reflected from a dichroic mirror (QuadLine, laser splitter, zt405/488/561/640rpc, AHF). To observe the activities of individual channels, the TIRF angle and EMCCD camera gain (e.g., EM gain multiplier setting: 285) were adjusted so that open ion channels appeared as high-contrast fluorescent spots on a dark background. The spots, corresponding to Ca^{2+}-flux through single transmembrane protein channels, had to remain in focus and have a round shape, with high intensity in the center and gradually

decreasing towards the periphery. Finally, fluorescent emission of Fluo-8 was collected through the 100 x oil TIRF objective, transmitted through a Quad-Band TIRF-Filter 446/523/600/677 HC (AHF), and recorded by a back-illuminated electron-multiplying CCD camera (iXon Ultra 897, 512 × 512 pixels, Andor) at a frame rate of 47.51 s^{-1}. The pixel size was 0.16 μm.
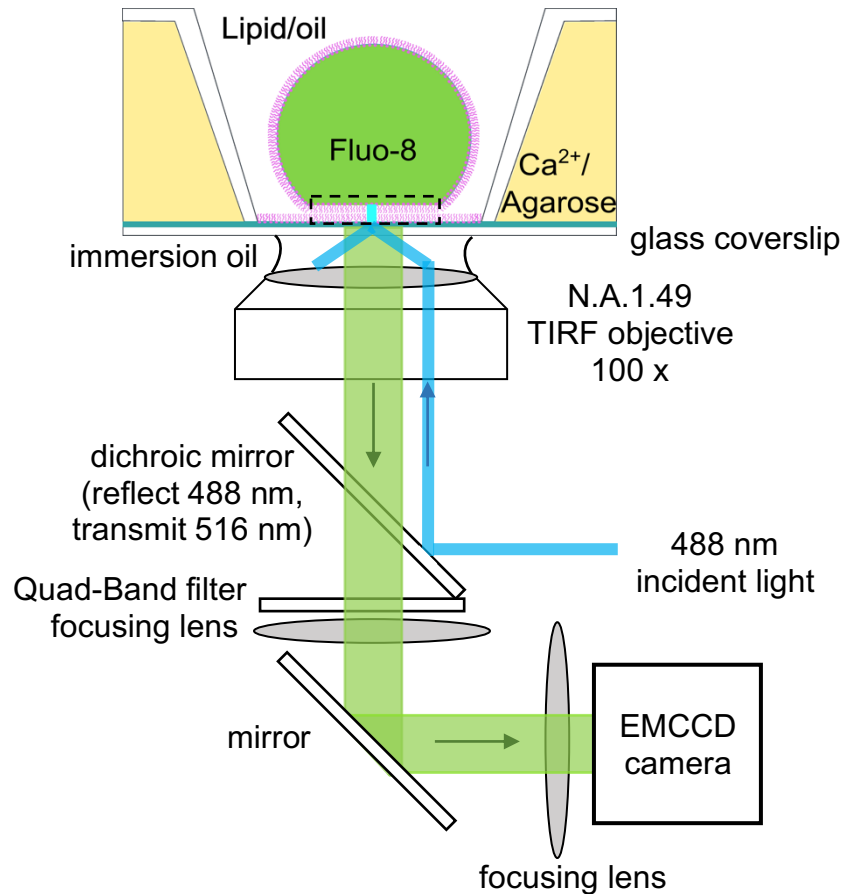

Figure 4.2: Schematic setup for imaging DIBs and fluorescence detection of Fluo-8 using TIRF-M. *At TIRF angle, 488 nm laser light is completely reflected at the bottom of the glass coverslip. The evanescent field of total reflected laser penetrates the spin-coated agarose film and illuminates the DIB membrane (marked with dashed line). The fluorescence of the Ca^{2+}-sensitive dye Fluo-8 is recorded at the vicinity of the membrane with an EMCCD camera.*

4.4.3.2 Imaging of fluorescently labeled single TOM-CC molecules in droplet interface bilayer membranes

To track the movement of Cy3-labeled TOM-CC molecules in DIB membranes, TIRF-M was used in a similar way as described in section 4.4.3.1 (Figure 4.3). The droplets contained about ~0.5 nM Cy3-labeled TOM-CC (section 4.2.5) in place of the TOM-CC molecules and Fluo-8. Again, the custom-made PMMA chamber containing DIB membranes was placed on a

specimen holder and a 10 x N.A.0.25 air objective (Nikon) was used to find the area of the lipid bilayer under epifluorescence illumination using a Cy3 HC filter (AHF). For visualization of single Cy3-labeled TOM-CC molecules inserted in DIB membranes, the objective was changed to a 100 x oil TIRF objective (Apochromat N.A.1.49, Nikon), still under epifluorescence illumination using the Cy3 HC filter. The filter setting for laser excitation (561 nm, 20 - 26 mW, P_{max} = 100 mW, Visitron) was then changed from Cy3 HC to QuadLine laser beam splitter (zt405/488/561/640rpc, AHF). Finally, the fluorescence emission from Cy3-labled TOM-CC reconstituted into the DIB membrane was collected through the 100 x oil objective under the TIRF illumination mode, transmitted through a Quad-Band filter (446/523/600/677 HC, AHF) and recorded by a back-illuminated EMCCD camera (iXon Ultra 897, 512 × 512 pixels, Andor) for 1 min at a frame rate of 14.87 s^{-1}. The pixel size was 0.16 μm.
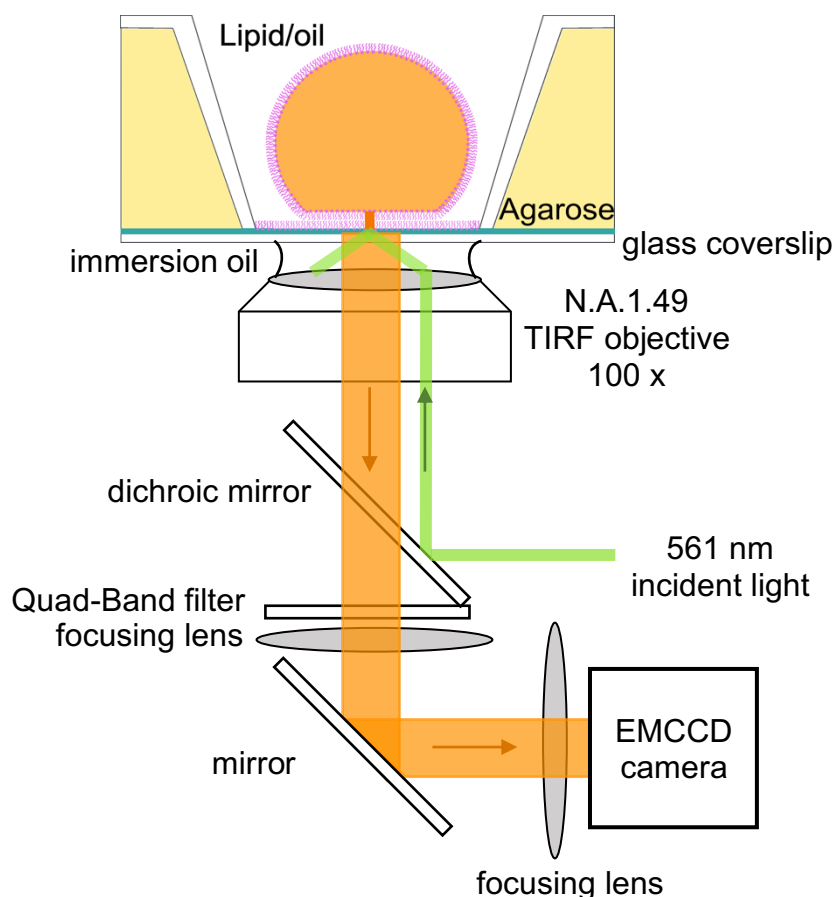

Figure 4.3: Schematic setup for fluorescence detection of Cy3-labeled TOM-CC in DIB membranes using TIRF-M. *At TIRF angle, 561 nm laser light is completely reflected at the bottom of the glass coverslip and its evanescent field illuminates the DIB membrane. The fluorescence of the Cy3-labeled TOM-CC is recorded with an EMCCD camera.*

4.4.3.3 Förster resonance energy transfer measurements

To investigate the interaction between mitochondrial presequence proteins and TOM-CC reconstituted in DIBs by Föster resonance energy transfer (FRET) measurements, DIB membrane preparation was essentially the same as described in section 4.3. Droplets contained ~0.5 nM Cy3-labeled TOM-CC (section 4.2.5) and ~2.5 nM Cy5-labeled mitochondrial presequence proteins (section 4.2.6). TIRF-M was used in a similar way as described in section 4.4.3.2. (Figure 4.4), except that the two back-illuminated EMCCD cameras (iXon Ultra 897, 512 × 512 pixels, Andor) were used to record simultaneously fluorescence emissions of Cy3 and Cy5 dyes split by a TwinCam filter set (Figure 4.4) (Teledyne).
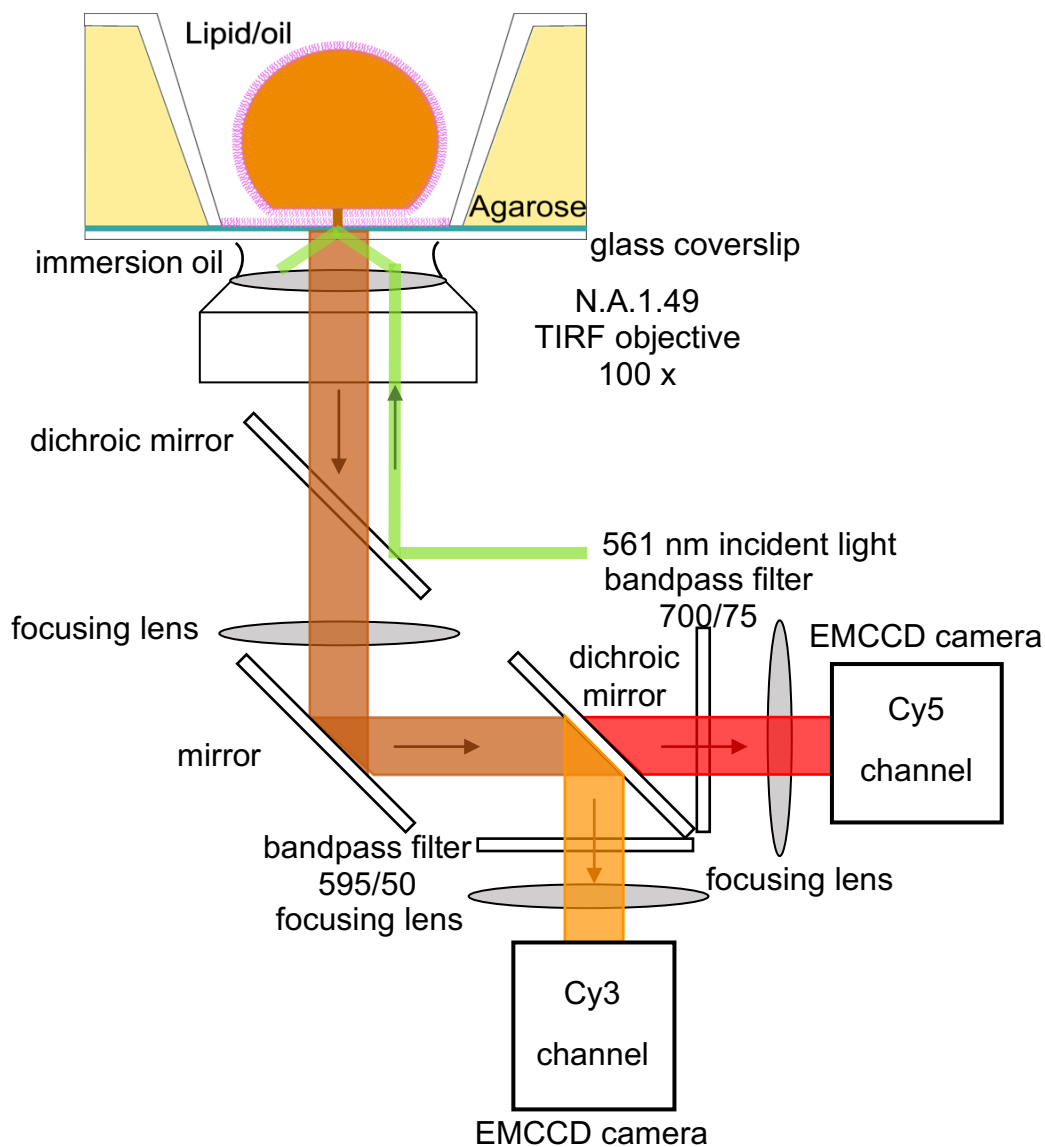

Figure 4.4: Schematic setup for fluorescence detection of Cy3-labeled TOM-CC and Cy5-labeled mitochondrial presequence proteins in DIB setup using TIRF-M. *At TIRF angle, the membranes are*

illuminated by 561 nm laser light in TIRF mode. Fluorescence of Cy3-labeled TOM-CC and Cy5-labeled mitochondrial presequence proteins is recorded simultaneously using two EMCCD cameras.

4.5 Data analysis

4.5.1 Tracking of fluorescence spots

To track and analyze the spatiotemporal dynamics and channel activities (Figure 4.5) of individual TOM-CC, Cy3-labeled TOM-CC, Tom40, OmpF, and -hemolysin molecules, respectively, a customized fully automated analysis routine was implemented in Matlab (The Mathworks, USA) in collaboration with Dr. Marcel Hörning (University of Stuttgart). The effect of fluorescence bleach was corrected by applying a standard fluorescence bleach correction procedure (Vicente et al., 2007). First, a double exponential decay was obtained by least-square fitting of an image series (average frame intensity $\langle I(t)_{raw} \rangle$) to:

$$f(t, a_k) = a_1 \exp(a_2 t) + a_3 \exp(a_4 t) \tag{1}$$

where t is the frame index (time) and a_k are the fitting parameters. The image time series were then corrected according to

$$I(t) = I_{raw}(t) / f(t, a_k) \tag{2}$$

where $I(t)$ is the intensity as a function of time t. No filter algorithm was applied. For single-molecule tracking, the initial spatial position of $\boldsymbol{x_0} = (x_0, y_0)$ of a fluorescence spot was manually selected and the fluorescence intensity of the fluorescent spot was fitted within a defined region of interested (ROI) according to

$$G_{2D}(\boldsymbol{x}, \boldsymbol{\mu}, p_k) = p_1 + p_{2,3}(\boldsymbol{x} - \boldsymbol{\mu}) + A exp(-(\boldsymbol{x} - \boldsymbol{\mu})^2 / 2\sigma^2) \tag{3}$$

The parameters $p_{2,3}$ considered possible local illumination gradients; $\boldsymbol{x} = (x, y)$ is the ROI with the fluorescence intensity information, A and σ are the amplitude and width of the Gaussian, p_k are parameters that characterize the background intensity of the ROI, and $\boldsymbol{\mu} = (x_0, y_0)$ defines the position of the Gaussian. The latter was used to update the position of ROI for the next image. The ROI size (typical widths: 30 - 60 pixels) was related to the size of the fluorescent

spot and the distance between adjacent spots. Spots whose fluorescence signal overlapped in time with neighboring spots were not considered because of the risk of confusing these spots.
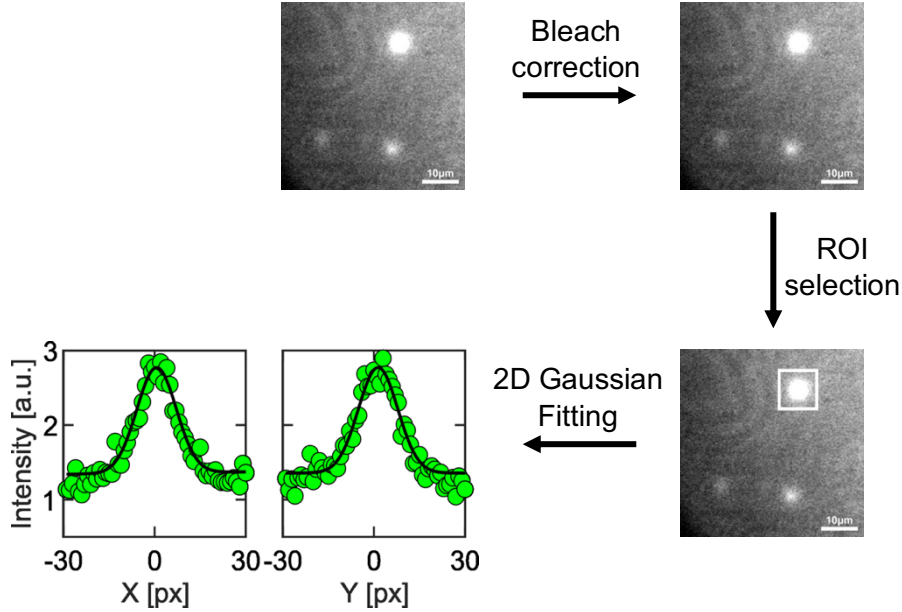

Figure 4.5: Flowchart for the analysis of TIRF image series. *An original TIRF image series was corrected by applying standard fluorescence bleach procedures. A ROI of a fluorescent spot (white square: 60 x 60 pixels, eq. (2)) was selected, and the fluorescence intensity profile was fitted to a two-dimensional symmetric Gaussian function with planar slope (eq. (3)). The obtained Gaussian fitting profile revealed the fluorescence intensity and position corresponding to the analyzed fluorescence spot.*

4.5.2 Determination of positional accuracy

The positional accuracy Δx of transmembrane protein channels as observed in section 4.5.1, was assessed according to (Thompson et al., 2002; Selvin et al., 2008):

$$\langle(\Delta x)^2\rangle = \frac{s^2 + a^2/12}{N} + \frac{8\pi s^4 b^2}{a^2 N^2} \tag{4}$$

where *s* is the width of the 2D Gaussian function fitting (eq. (3)) a fluorescent spot (Figure 4.5), *a* is the pixel size (here: 0.16 μm), *N* is the total number of photons in the spot, and *b* is the background noise. The units of Δx, *s* and *a* are μm. All parameters are functions of time.

The total photon number *N* was estimated from the measured intensities recorded by back-illuminated EMCCD cameras according to (Hirsch et al., 2013):

$$N = I_{int}/F \qquad (5)$$

where F is the conversion factor between the measured intensities and the photon number, and I_{int} is the intensity integral of the fluorescent spot (eq. (3)). I_{int} was calculated as follows:

$$I_{int} = 2\pi\sigma^2 A \qquad (6)$$

where σ and A are the width and the amplitude of 2D Gaussian function (eq. (3)), respectively.

The background noise b of the image was calculated according to:

$$b = I_b/F \qquad (7)$$

where I_b is the average background intensity of the image.

To obtain the conversion factor F, a series of background images were recorded by the back-illuminated EMCCD camera (iXon Ultra 897, 512 × 512 pixels, Andor), under the condition of gradually increasing light source intensity. The variance $(B_{var})^2$ of background intensity of the image was calculated as follows:

$$(B_{var})^2 = \frac{\sum(I(x_i, y_i) - \bar{I})^2}{n - 1} \qquad (8)$$

where $\bar{I}$ is the mean background intensity of the image, $I(x_i, y_i)$ is the background intensity of each pixel in the image, and n is the total number of the pixels in the image. Moreover, $\bar{I}$ and $(B_{var})^2$ are related to the average number of background photons p in (eq. (9)) and (eq. (10)) according to the (Hirsch et al., 2013) as:

$$\bar{I} = F \cdot p + I_0 \qquad (9)$$

$$(B_{var})^2 = 2F^2 \cdot p + v_0 \qquad (10)$$

where I_0 is the offset of the camera in darkness, and v_0 is the intrinsic variance from detector to readout. Substituting $p = (\bar{I} - I_0)/F$ into eq. (10), the eq. (11) is obtained:

$$\left(B_{var}(t)\right)^2 = 2F \cdot (\bar{I}(t) - \bar{I}_0) + v_0 \tag{11}$$

Fitting $\left(B_{var}(t)\right)^2$ against $\bar{I}(t)$ using the eq. (11) reveals the conversion factor F. A typical relation between background variance $\left(B_{var}(t)\right)^2$ and mean background intensity $\bar{I}(t)$ is shown in Figure 4.6.
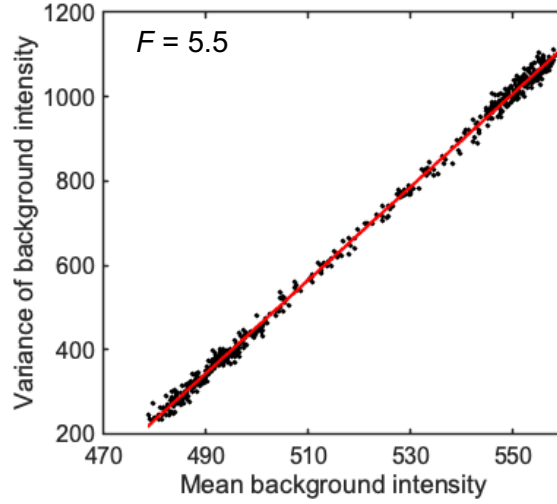

Figure 4.6: Mean intensity - variance plot for F factor estimation. Each black dot represents mean and variance of the intensity of an individual pixel for 550 frames across a single data set recorded by the EMCCD camera (iXon Ultra 897, 512 × 512 pixels, EM gain multiplier setting: 285, Andor) used in this work. The data set was taken with different light intensities. The measured intensities represent the camera readout. Readout rate, 47.5 s $^{-1}$. Estimated conversion factor F, 5.5.

4.5.3 Calculation of diffusion coefficients

The lateral diffusion constants D of freely moving single molecules in DIBs were obtained individually for spots within the respective high and intermediate amplitude range by linear regression of the time delay τ and the mean square displacement of the spots according to (Einstein, 1905) as:

$$D = \frac{\langle |r(x, y, \tau) - r(x_0, y_0, \tau)|^2 \rangle}{4\tau} \tag{12}$$

The largest time delay $\tau_{max} = 0.5$ s was iteratively decreased to suffice the coefficient of determination $R^2 \geq 0.9$ and to avoid the influence of sub-diffusion or insufficient amount of

data. Molecules with diffusion coefficients less than $D_{\min} = 0.01$ µm^2 s^{-1} were defined as non-diffusive considering the spatiotemporal limitations of the experimental setup and resolution of the fitted two-dimensional Gaussian function, since most led to $R^2 << 0.9$. The calculation of the mean μ and standard deviation σ of the diffusion constant was done using the log-transformation due to its skewed normal distribution, as

$$\mu_{log} = \frac{1}{N}\sum_{i=1}^{N} log(D_i) \tag{13}$$

and

$$\sigma_{log} = \sqrt{\frac{1}{N}\sum_{i=1}^{N}\left(log(D_i) - \mu_{log}\right)^2} \tag{14}$$

where N is the number of diffusion constants obtained for one experimental condition. The back-transformation was calculated then as

$$\mu = exp\left(\mu_{log} + 0.5 \cdot \sigma_{log}^2\right) \tag{15}$$

and

$$\sigma = \sqrt{\mu^2\left(exp(\sigma_{log}^2) - 1\right)} \tag{16}$$

respectively, following the Finney estimator approach (Finney, 1941). The standard error of mean (*SEM*) considering a confidence interval of 95 % was calculated as

$$SEM = \frac{1.96\,\sigma}{\sqrt{N}} \tag{17}$$

5 Results

The TOM-CC protein channel in the outer mitochondrial membrane is the major entry port for nuclear-encoded proteins from the cytosol into mitochondria (for review, see Wiedemann and Pfanner, 2017; for review, see Pfanner et al., 2019). Proteins entering the mitochondrial matrix require a transient interaction of TOM-CC with the mitochondrial inner membrane protein translocase TIM23 (Figure 3.1) (Chacinska et al., 2005; Gevorkyan-Airapetov et al., 2009; Kuzmenko et al., 2011; Shiota et al., 2011). Based on the single-molecule tracking experiments (for review, see Appelhans and Busch, 2017), the formation of a TOM-TIM23 supercomplex may immobilize the TOM complex in the mitochondrial outer membrane. However, the spatiotemporal dynamics of the TOM-CC have not yet been studied in the context of its function. Single-molecule electrophysiology and structural work (see section 3.3) have not yet yielded any information on this point. In this section, it will be investigated whether and how the lateral movement of TOM-CC in a well-defined planar membrane system affects the channel activity of TOM-CC *in vitro*.

5.1 Functional integration of individual TOM-CCs into droplet interface bilayer membranes
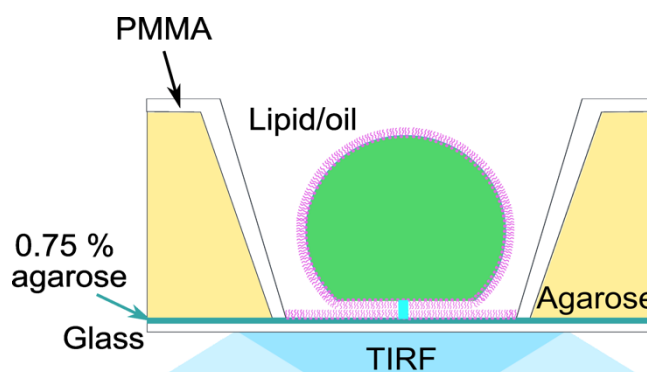

Figure 5.1: Scheme of a droplet interface lipid bilayer. *A DIB membrane is formed by the contact of an aqueous droplet coated with a Langmuir-Blodgett lipid (DPhPC) film in a lipid/oil (DPhPC/Hexadecane and silicone oil) phase and a lipid monolayer on an ultrathin agarose hydrogel. A transmembrane protein channel (cyan) spontaneously reconstitutes from the side of the aqueous droplet into the DIB membrane. Pink, lipid; green, aqueous droplet.*

Due to the complexity of biological membrane and its peripheral structures, it is often difficult to decipher the interplay between the nature of lateral mobility and protein function *in vivo*. However, this could be circumvented by reconstituting isolated membrane proteins in well-defined synthetic lipid bilayers (for review, see Tanaka and Sackmann, 2005). Droplet-interface bilayer (DIB) membranes have been shown to be an efficient platform for single-molecule biophysical analyses of membrane proteins (for review, see Bayley et al., 2008; Huang et al., 2015; Wang et al., 2019a). Therefore, the DIB membrane also seemed to be suitable for studying the channel permeability and spatiotemporal dynamics of TOM-CC. DIB membranes are formed by self-assembly of lipid molecules at a water-oil interface (Figure 5.1). To study the movement of proteins and the activities of individual channels in these membranes, TIRF microscopy, as used in this work, proved to be the method of choice.

To investigate the biophysical properties of TOM-CC protein channels, TOM-CC was first purified from *N. crassa* mitochondria and fluorescently labeled. Subsequently, mitochondrial presequence protein (Su9-MBP) was fluorescently labeled. DIB membrane formation was optimized and validated after reconstitution of TOM-CC. Subsequently, the binding of TOM-CC to Su9-MBP was investigated using Förster resonance energy transfer (FRET) measurements to ensure that the integration of individual TOM-CCs into DIB membranes was functional.

5.1.1 Isolation and fluorescence labeling of TOM-CC

TOM-CC was isolated from *N. crassa* mitochondria carrying a version of the Tom22 subunit with a hexahistidine tag at the C-terminus (section 4.2.2, Figure 5.2A), using Ni-NTA affinity (Figure 5.2B) and anion exchange chromatography (Figure 5.2C). Special attention was paid to a protein concentration as high as possible and a low detergent concentration (close to the CMC) in order to achieve sufficient insertion rates in DIB membranes and to avoid solubilization of the membrane by detergent. Optimal results were obtained with protein concentrations > 0.5 mg/ml and n-dodecyl-β-D-maltoside (DDM) of 0.1 % (w/v). Analysis of purified protein by SDS-polyacrylamide gel electrophoresis (SDS-PAGE) followed by Coomassie Blue staining revealed all known subunits of the TOM core complex, Tom40, Tom22, Tom7, Tom6 and Tom5 (Figure 5.2D). The small subunits Tom7, Tom6 and Tom5 were not separated by SDS-PAGE.
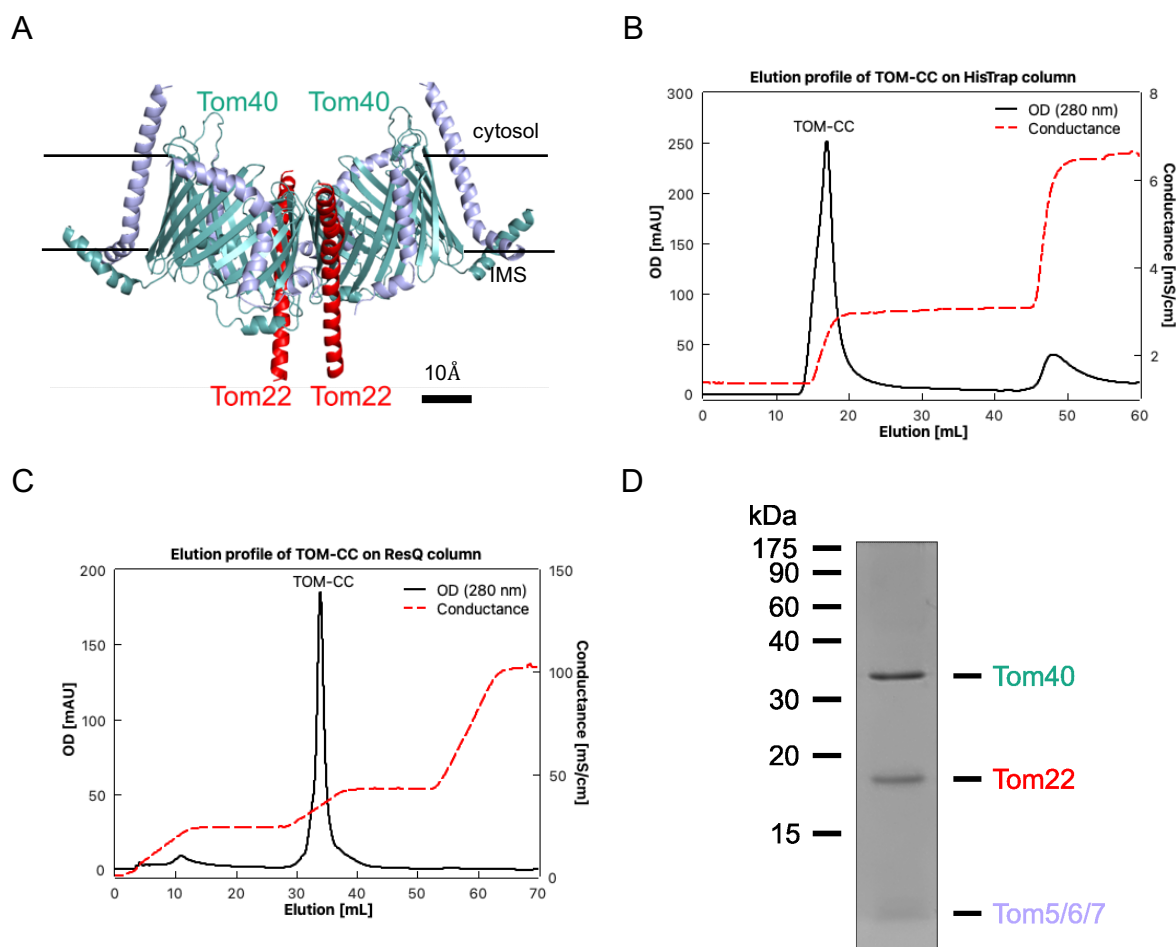
Figure 5.2: Purification of TOM core complex. *A) Atomic model based on the cryo-EM map of N. crassa TOM core complex (side view, EMDB EMD-3761(Bausewein et al., 2017)). B) Elution profile of detergent-solubilized outer mitochondrial membrane proteins (~2 g) loaded onto a Ni-NTA affinity column. 6xHis tagged TOM-CC was eluted with 300 mM imidazole elution buffer (Table 4.5). C) Elution profile of the TOM core complex loaded on an anion exchange column (ResQ). Fractions of B) containing TOM-CC were loaded onto the column and TOM-CC was eluted through a linear salt gradient between 220 and 400 mM KCl (Table 4.5). D) SDS gel of isolated TOM-CC stained with Coomassie Blue. The gel reveals all subunits of the complex, i.e. Tom40, Tom22, Tom7, Tom6 and Tom5.*

To investigate the binding of TOM-CC to mitochondrial presequence proteins, TOM-CC was fluorescently labeled with Cy3 maleimide dye (Section 4.2.5) at its two cysteines in Tom40 (Figure 5.3A). To ensure complete removal of the unbound dye, TOM-CC was bound to Ni-NTA resin via its His-tag at the Tom22 subunit and washed with sufficient buffer. After elution with imidazole, the Cy3-labeling of TOM-CC was validated by SDS-PAGE under 555 nm light (Figure 5.3B).
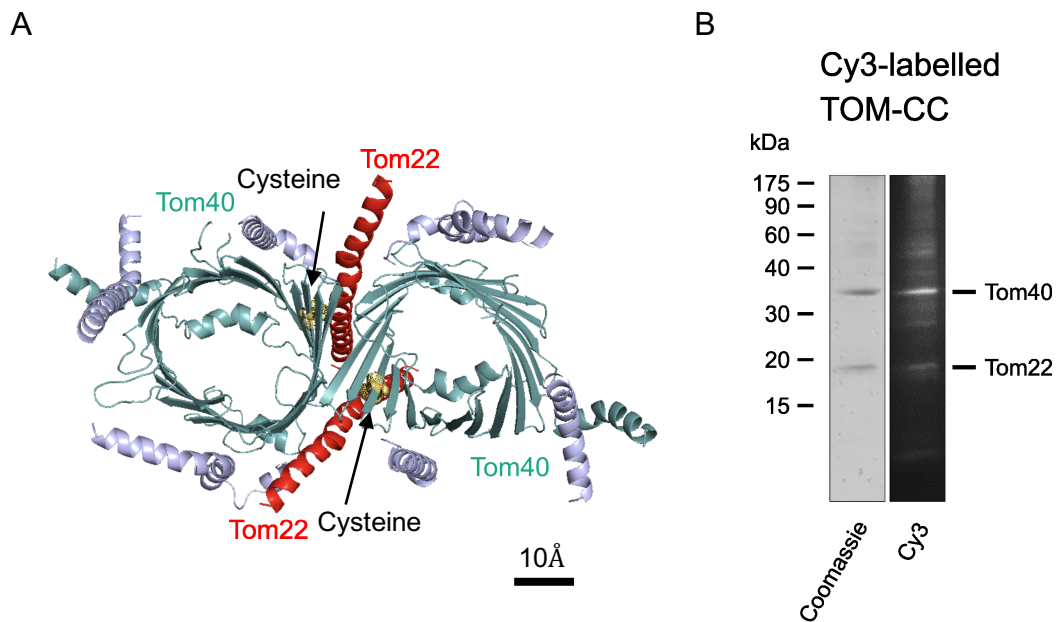
Figure 5.3: Fluorescent labeling of TOM-CC. *A) Atomic model based on the cryo-EM map of N. crassa TOM core complex (EMDB, EMD-3761 (Bausewein et al., 2017)). Each Tom40 contains one cysteine. The yellow dots represent the cysteine position on Tom40. The thiols of the cysteines were fluorescently labeled with Cy3-maleimide dye. B) SDS gel of Cy3-labeled TOM-CC analyzed by Cy3 fluorescence ($\lambda_{ex} = 555\,nm$) and Coomassie Blue staining, respectively. Free Cy3-maleimide dyes are virtually absent.*

5.1.2 Fluorescence labeling of mitochondrial presequence protein

To investigate the binding of Cy3-labeled TOM-CC to mitochondrial presequence protein using Förster resonance energy transfer (FRET) measurements, a model presequence protein (Su9-MBP) consisting of the sorting sequence of F0-ATPase subunit 9 (Su9) (Rojo et al., 1995) fused to maltose-binding protein (MBP) (Lebendiker and Danieli, 2017) was fluorescently labeled with Cy5-maleimide dye (section. 4.2.6). The unconjugated Cy5 dyes were separated from the Cy5-labeled Su9-MBP using a gel filtration PD-10 desalting column. Examining the purity of Cy5-labeled Su9-MBPs (Figure 5.4), the fluorescent labeled protein samples were validated by SDS-PAGE under 638 nm light, followed by Coomassie Blue staining.
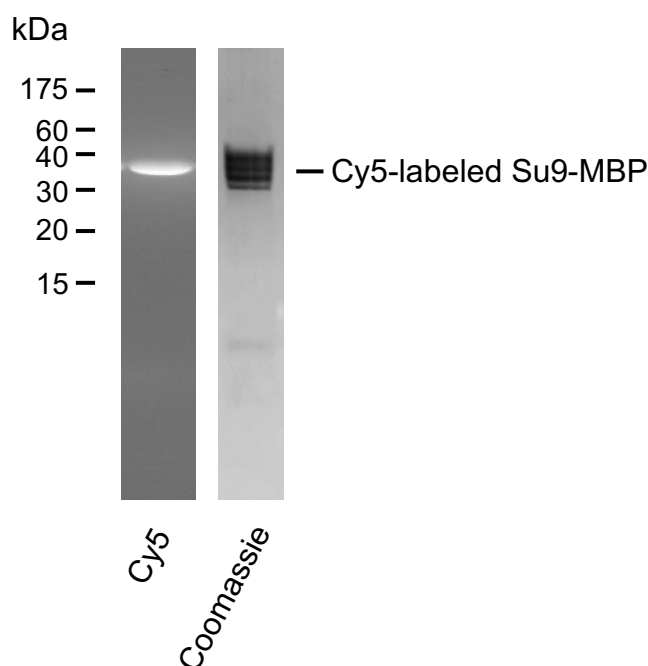
Figure 5.4: Fluorescent labeling of Su9-MBP. *SDS gel of Cy5-labeled Su9-MBP was visualized by Coomassie Blue staining and Cy5 fluorescence, respectively. No free Cy5-maleimide dyes were detected under the 638 nm excitation.*

5.1.3 Optimization of the hydrogel composition for supported droplet interface bilayer membranes

The texture of the hydrogel supporting DIB membranes is critical for both lateral mobility and channel activity of TOM-CC to be studied by single-molecule TIRF microscopy (Figures 4.2 and 5.1). A well-formed hydrophilic phase of the hydrogel is a prerequisite for membrane formation at the water/oil interface. In addition, sufficient thickness of the hydrogel plays an important role in preventing reconstituted membrane proteins from becoming immobilized by interaction with the supporting glass coverslip (Figure 5.1). To obtain efficient TIRF signals of the DIB membrane, hydrogel layers larger than 200 nm must be avoided.

To address these issues, low melting point agarose was chosen as the hydrogel because it has been shown to be highly suitable for spin-coating glass coverslips for the fabrication of DIB membranes (Leptihn et al., 2013; Huang et al., 2015; Rosholm et al., 2017). Based on previous studies (Wang et al., 2018), the thickness was adjusted to ∼50 nm using a concentration of 0.75 % (w/v) unmodified low melting point agarose and 50 % (w/v) Ni-NTA modified agarose by varying the agarose temperature, volume, and angular frequency of spin coating (section 4.3). Because the Ni-NTA-modified agarose was custom synthesized for spin coating,

significantly higher concentrations were required to increase the probability that His-tagged membrane proteins would be permanently entrapped in DIB membranes.

A typical AFM image of an agarose hydrogel used to support the DIB membrane is shown in Figure 5.5. It shows that the agarose layer is ~40 nm deep, which met all subsequent experimental requirements.
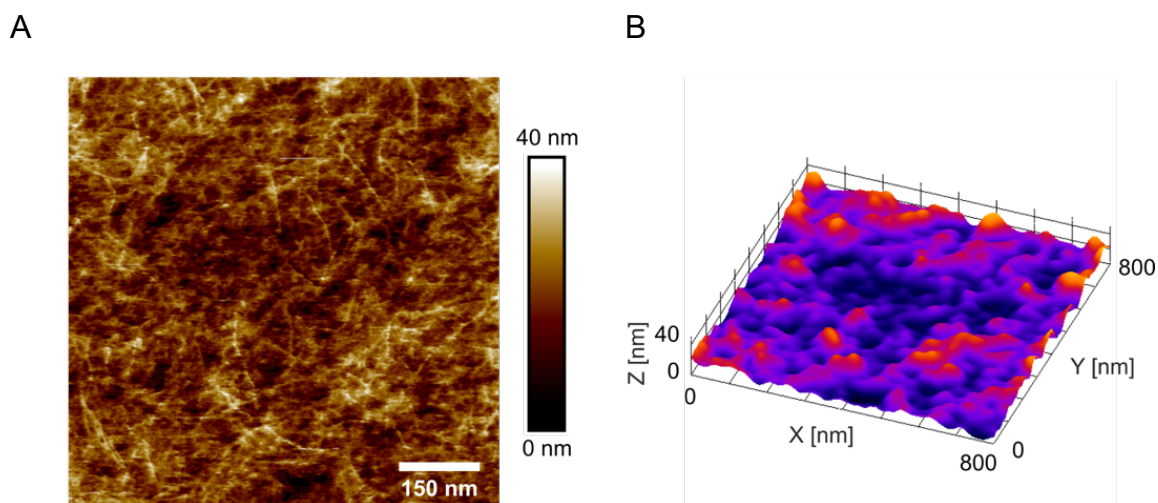
A   B

Figure 5.5: AFM image of an agarose hydrogel used for TIRF imaging of supported DIB membranes. *A) Representative AFM image of unmodified agarose spin-coated onto a glass coverslip. The brighter fiber-like structures are entangled with each other to form a network. The mesh size of the network distributes from ~10 nm to 100 nm. B) Surface representation of the original AFM image indicating a hydrogel thickness of ~40 nm.*

5.1.4 Preparation and visualization of droplet interface bilayer membranes

In addition to an optimal agarose hydrogel layer under the DIB membrane (section 5.1.3), lipid molecules also play an important role in the formation of stable DIB membranes.

Here, 1,2-diphytanoyl-sn-glycero-3-phosphocholine (DPhPC) was chosen as the lipid, because it has highly branched hydrophobic alkyl chains (Redwood et al., 1971; Lindsey et al., 1979) and is most commonly used for DIB membrane formation (for review, see Bayley et al., 2008; Huang et al., 2015; Rosholm et al., 2017). The cylindrically shaped DPhPC molecules spontaneously assemble to a dense packing state at equilibrium which with minimal packing defects (Venkatesan et al., 2018). Nevertheless, lipids remain in liquid phase at low temperatures (Baba et al., 1999; Venkatesan et al., 2018), such as 1,2-dioleoyl-sn-glycero-3-

phosphocholine (DOPC) and 1-palmitoyl-2-oleoyl-sn-glycero-3-phosphocholine (POPC) (Venkatesan et al., 2018) could also be used.
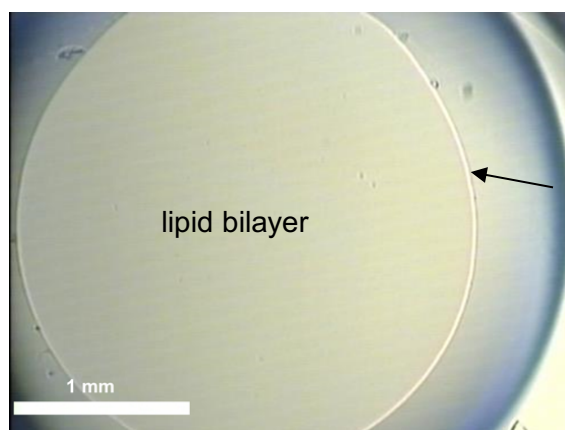

Figure 5.6: Visualization of a DIB membrane using Hoffman contrast microscopy. The central region surrounded by the light circle boundary (arrow) is the DIB membrane. The edge (arrow) of the DIB membrane formed by DPhPC on a 0.75 % agarose hydrogel separates the contacted lipid bilayer from the rest of the aqueous droplet.

Using DPhPC as a lipid, DIB membranes (Figure 5.6) supported by ultrathin agarose hydrogels (Figure 5.5) were formed according to previous published procedures (section 4.3) and adjusted for reconstitution of TOM-CC (Figure 5.2). Optimal formation of membranes and protein reconstitution occurred at a temperature of 30 °C, and at a TOM-CC concentration in the droplets of 4 µg/mL. The composition of the hydrophobic oil phase proved to be a very important parameter. The best results were obtained with 9.5 mg/mL DPhPC in hexadecane/silicone oil at a volume ratio of 1:1. The DIB membranes were stable for at least up to one day.

5.1.5 Visualizing TOM-CC binding to mitochondrial presequence proteins using Förster resonance energy transfer measurements

To ensure that subsequent exploration of channel activity and spatiotemporal dynamics of TOM-CC in the DIB membrane was meaningful, it was investigated whether TOM-CC *functionally* incorporated into the DIB membranes.
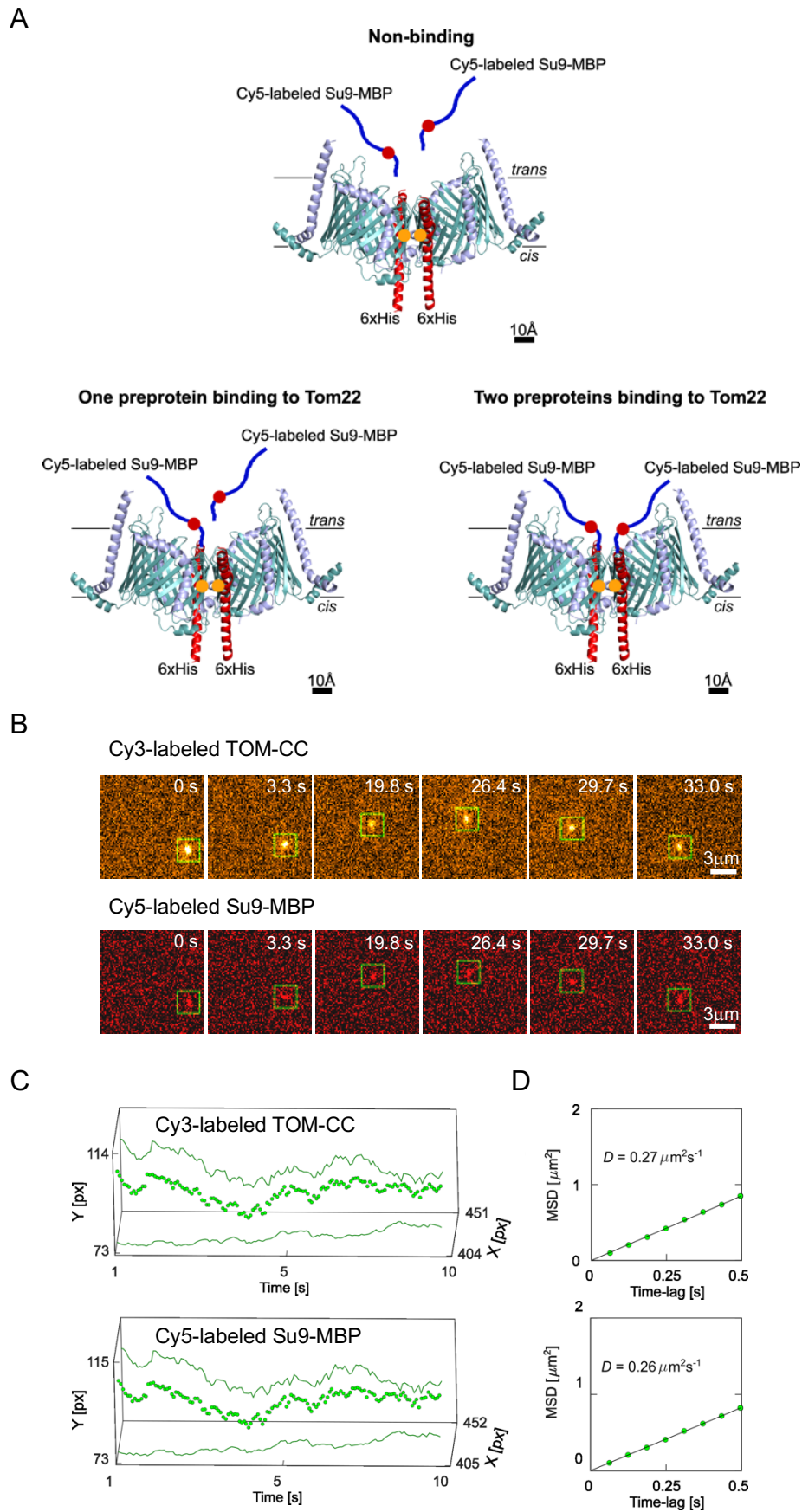
Figure 5.7: Binding of Cy3-TOM-CC to Cy5-Su9-MBP measured by sm-FRET. *A) Cy3-TOM-CC and Cy5-Su9-MBP were used to optically study the binding of TOM-CC (protein concentration in droplet*

~0.5 nM) reconstituted in DIB membrane to Su9-MBP (protein concentration in droplet ~2.5 nM). Membranes were excited at a wavelength of λ_{Cy3}^{ex}=561 nm (20 - 24 mW). Fluorescence emission was simultaneously measured with two synchronized cameras at λ_{Cy3}^{em}= 595 $\pm$ 25 nm or λ_{Cy5}^{em} =700 $\pm$ 37 nm. When Cy5-Su9-MBP was bound to Cy3-TOM-CC (r < Förster radius r_0 = 5 nm (Joo and Ha, 2008)), the energy of Cy3 emission was significantly transferred to Cy5. The positions of Cy3 and Cy5 in TOM-CC and Su9-MBP are marked in red (Cy3) and orange (Cy5). B) Representative TIRF microscopy images of an agarose-supported DIB membrane with a Cy3-TOM-CC molecule that bound a Cy5-Su9-MBP protein. Images were acquired for 33 seconds at a frame rate of 14.5 s^{-1}. The positions of Cy3- and Cy5-labeled molecules overlap within $\pm$ 2.4 pixels, indicating binding of Su9-MBP to TOM-CC. trajectories of Cy3-TOM-CC and Cy5-Su9-MBP corresponding to B) in an interval of 10 seconds. Plotting the entire trajectory was not possible due to a weak signal-to-background ratio and inaccurate determination of positions. D) Lateral diffusion coefficients of Cy3-TOM-CC and Cy5-Su9-MBP. Diffusion coefficients were determined from the mean square displacement (MSD) as a function of time. The largest time delay 0.5 s was iteratively decreased to suffice the coefficient of determination $R^2 \geqslant$ 0.9. Pixel size [px], 0.16 μm.

To this end, the binding of TOM-CC (Figure 5.3B) to Su9-MBP (Figure 5.4), a model protein composed of the presequence of mitochondrial ATP synthase subunit 9 and maltose-binding protein, was investigated by Förster resonance energy transfer (FRET) measurements using TIRF-M (section 4.4.3.3). Two cameras were used to simultaneously record donor emission fluorescence from Cy3-labeled TOM-CC and acceptor emission fluorescence from Cy5-labeled Su9-MBP at 561 nm laser excitation (Figure 5.7A). First, Cy3-labeled TOM-CC was inserted into an agarose-supported DIB membrane (Figure 5.6). Proper insertion of TOM-CC was given if the Cy3 signal remained in focus. Functional insertion was then tested by FRET between Cy3- TOM-CC as donor and Cy5-Su9-MBP as acceptor. Cy5-Su9-MBP bound to Cy3-TOM-CCs should show an FRET signal in the Cy5 camera upon excitation of Cy3 at wavelength of 561 nm.

A typical result is shown in Figures 5.7B and C. Figures 5.7B top and bottom show focused fluorescent spots representing Cy3-TOM-CC and Cy5-Su9-MBP over time. Both signals overlap in time and position. This indicates that TOM-CC is bound to Su9-MBP. To further support this conclusion, the fluorescence intensity profiles of Cy3-TOM-CC and Cy5-Su9-MBP were fitted to two-dimensional symmetric Gaussian functions with planar slopes. The positions of each Cy3-TOM-CC and Cy5-Su9-MBP spot were determined based on the center of the 2D Gaussian peak. Figure 5.7C shows that the determined x,y positions of Cy5-Su9-

MBP match those of Cy3-TOM-CC over time. Cy3-TOM-CC and Cy5-Su9-MBP yielded diffusion constants of $D_{Cy3} \simeq 0.25 \pm 0.08 \ \mu m^2 \ s^{-1}$ and $D_{Cy5} \simeq 0.24 \pm 0.07 \ \mu m^2 \ s^{-1}$, respectively (Figure 5.7D, mean $\pm$ SEM, $n = 10$). These results suggest that TOM-CC reconstituted functionally in DIB membranes. The DIB system established here was thus suitable to further investigate the channel activity and spatiotemporal dynamics of TOM-CC in lipid membranes.

5.2 Simultaneous investigation of channel activity and lateral mobility of single-molecule TOM-CC channels in droplet interface bilayer membranes

In section 5.1 it was shown that TOM-CC functionally integrates into an agarose supported DIB membrane. The DIB membrane system established here was then considered suitable to optically visualize the channel activity of individual TOM-CCs and to investigate whether and, if so, how the channel activity of TOM-CCs correlates with their lateral movement in the membrane.

To achieve this goal, DIB membranes were now prepared by contacting aqueous droplets coated with a lipid monolayer in a lipid/oil phase and a lipid monolayer on an agarose hydrogel (as described above, Figure 5.1) in the presence of Ca^{2+} ions (0.66 M) on the *cis* side of the DIB membrane, while Ca^{2+}-sensitive fluorescent dyes (Fluo-8, 7 μM) are present on the *trans* side. Ca^{2+} ion flux through individual TOM-CCs was measured by observing Fluo-8 emission in close proximity to the membrane using TIRF microscopy in the absence of membrane potential to avoid voltage-dependent TOM-CC gating (Figure 5.1). In contrast to the classical approach of single molecule tracking of fluorescently labeled proteins (Manzo and Garcia-Parajo, 2015) , an almost instantaneous update of fluorophores in the vicinity of TOM-CC nanopores could be observed, and the observation time for spatiotemporal tracking of single molecules could be up to several minutes. This is because the aqueous droplet contains a reservoir of Fluo-8 dyes. When the Fluo-8 molecules are bleached or diffused away, new Fluo-8 molecules can diffuse from the bulk of the droplet into the vicinity of the DIB membrane. The Ca^{2+} concentrations in the hydrogel were chosen to be relatively high to ensure a strong ion gradient across the membrane and thus sufficient ion flux through individual ion channels for appropriate fluorescence signal to background ratios.

In the following sections, I first describe how the channel activity of individual TOM-CC molecules can be monitored by optical means. Subsequently, it will be shown how the same fluorescence signal can be used to track individual TOM-CC in the membrane.

5.2.1 Visualization of the TOM-CC to reveal its opening and closing channel activity

In order to characterize the open-closed channel activity of individual TOM core complexes, the DIB membranes were illuminated with a 488 nm laser under TIRF mode (section 4.4.3.1). To monitor the rapid change in channel activity of TOM-CC molecules (Poynor et al., 2008), a back-illuminated electron-multiplying CCD camera was used to monitor Fluo-8 emission in close proximity to the membrane at a frame rate of 47.5 s^{-1} and an exposure time of 19 ms. The intensity of fluorescent spots was expected to correspond to the Ca^{2+} ion flux through individual TOM-CCs channels (Figure 5.8).
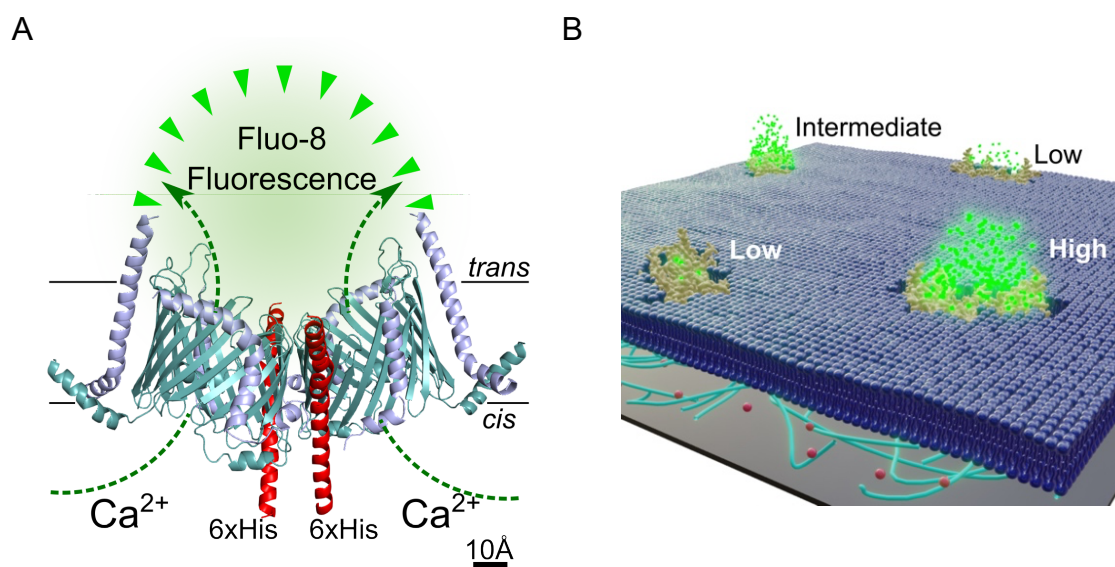

Figure 5.8: Scheme for imaging the ion channel activity of single TOM-CC molecules. *A) The ionic pathway through the two aqueous β-barrel Tom40 pores is used to optically study the open-closed channel activity of individual TOM-CCs. The cis side of the membrane contained Ca^{2+}-ions (0.66 M), while having at the trans side a Ca^{2+}-sensitive fluorescent dye (Fluo-8) and KCl (1.32 M) to balance the membrane osmotic pressure. The high Ca^{2+} content is necessary to induce high calcium flux through the TOM-CC pores and to provide reliable optical signals. Ca^{2+}-ion flux through individual TOM-CCs from cis to trans is driven by a Ca^{2+} concentration gradient, established around the two Tom40 pores, and measured by monitoring Fluo-8 emission in close proximity to the membrane using TIRF microscopy. Due to the higher osmolality at trans side, water flows from cis to trans side. Grey green, Tom40; red, Tom22; light purple, Tom7, Tom6 and Tom5. B) Different channel activities of TOM-CC*

in an agarose-supported DIB membrane. The level of the fluorescence (high, intermediate, and low intensity) correlates with corresponding permeability states of a TOM-CC molecule. Green dots, fluorescent Ca^{2+}-Fluo-8; red dots, Ca^{2+} ions.

Figure 5.9A shows a typical TIRF image of a DIB membrane with TOM-CC. It displays three fluorescent spots of high (S_H), intermediate (S_I) and low (S_L) intensity. The fact that the TOM-CC is a dimer with two identical β-barrel pores (Bausewein et al., 2017; Araiso et al., 2019; Tucker and Park, 2019; Wang et al., 2020) suggests that the high and intermediate intensity levels correspond to two conformational states (S_H and S_I) with two pores and one pore open, respectively. The low intensity level may represent a conformation (S_L) where both pores are closed with residual permeation for calcium. Therefore, TOM-CC molecules with two pores or one pore open appear as high-contrast fluorescent spots on a dark background. In contrast, no contrasting fluorescent spots are observed in membranes without TOM-CC or with two-pores closed TOM-CC.

To quantify the channel activity of TOM-CC and validate that TOM-CC switches between three different states of ion permeability, individual fluorescent spots were selected, and fluorescence intensity was determined. First, a time series of the individual TIRF images was acquired for 1 min and then corrected for fluorescence bleach. Figure 5.9B shows the average background intensity of 512 x 512 pixels TIRF images over time. The curve follows a typical double exponential decay (Vicente et al., 2007). After bleach correction, the amplitudes of the individual spots were determined by fitting their intensity profiles to a two-dimensional symmetric Gaussian function with planar slope to account for possible local illumination gradients in the bleach-corrected background (Figure 5.9C). Based on the analysis of $N > 5.3$ x 10^5 images, the time evolution of the amplitude signals (Figure 5.9D) shows that the TOM-CC does not occupy only one of the permeability states S_H, S_I, and S_L, but can switch between these three permeability states with time.
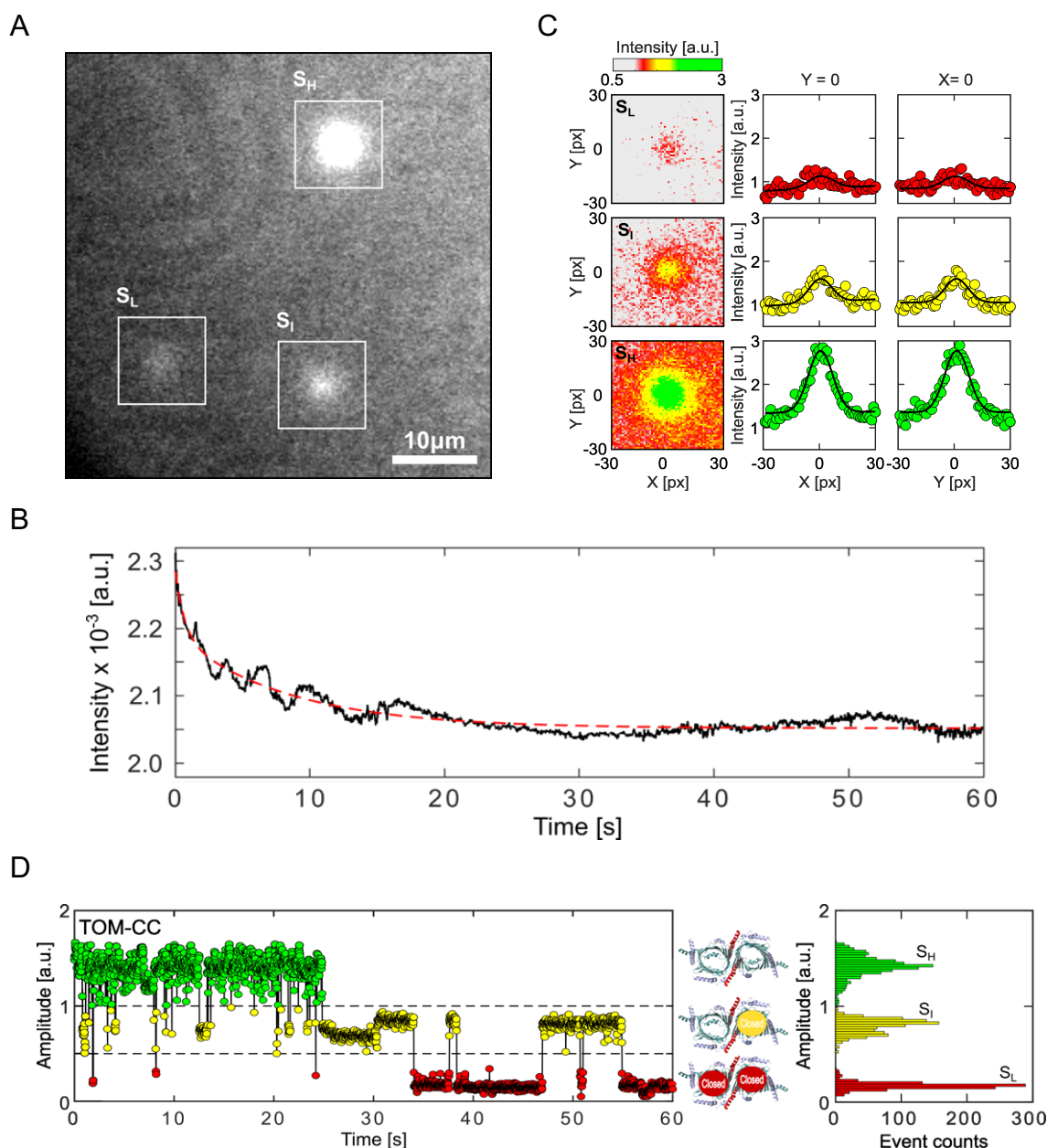
Figure 5.9: Visualizing the two-pore channel activity of TOM-CC. *A) Typical image (N > 5.3 x 10⁵)
of an unmodified agarose-supported DIB membrane with TOM-CC channels under 488 nm TIRF-
illumination. The white squares mark spots of high (S_H), intermediate (S_I) and low (S_L) intensity. The
TIRF image has not been corrected by fluorescence bleach. B) Average intensity of a background image
used to compensate for fluorescence bleach. Black line, average total intensity of a typical TIRF image
series (512 x 512 pixels) as a function of time; red dashed line, a double exponential decay obtained by
least-square fitting of the black curve. For the bleach correction, the TIRF image series were divided
by the obtained double exponential decay. The data corresponds to the whole TIRF image series shown
in Figure 5.9A. C) Fitting the fluorescence intensity profile of the three spots marked in A) to two-
dimensional Gaussian functions. Red, yellow, and green intensity profiles represent TOM-CC in S_L, S_I
and S_H demonstrating Tom40 channels, which are fully closed, one and two channels open, respectively.*

53

Pixel size, 0.16 μm. D) Fluorescence amplitude trace of the two-pore β-barrel protein channel TOM-CC. The TOM-CC channel switches between S_H, S_I, and S_L permeability states over time. Inserts, schematic of N. crassa TOM core complex with two pores open in S_H (top), one pore open in S_I (middle), and two pores closed in S_L (bottom) (EMDB, EMD-3761(Bausewein et al., 2017)); Fluorescence amplitude histogram of the two-pore TOM-CC demonstrates three distinct peaks, corresponding to the S_H, S_I, and S_L states. a.u., arbitrary unit.

5.2.2 Visualization of the TOM-CC to reveal the correlation between the permeability states and lateral mobility

Lateral mobility (e.g. free, restricted or directed diffusion) is an important factor for the organization and function of biological membranes and its components (for review, see Owen et al., 2009; Spector et al., 2010; Alenghat and Golan, 2013; for review, see Kusumi et al., 2014; Heine et al., 2016; for review, see Jacobson et al., 2019). In some cases, the transient anchoring of mobile membrane proteins thereby precedes protein-induced signaling events, as shown for CFTR (Haggie et al., 2006) and presynaptic calcium channels (Schneider et al., 2015). It is also well accepted that there is a direct correlation between activity and rotational membrane diffusion for cytochrome oxidase (Kawato et al., 1981) and sarcoplasmic reticulum ATPase (Thomas and Hidalgo, 1978; Hoffmann et al., 1979).

In this section, I asked whether, and if so, how the mode of mobility affects the channel activity of TOM-CC and its permeability states S_H, S_I and S_L. To this end, I simultaneously tracked the open-closed activity and position of individual TOM-CC molecules in the membrane over time (Figure 5.10 A). Based on the fluorescence signals shown in Figure 5.9C and a conversion factor between the measured intensities and the photon number of 5.5 (Figure 4.6), the positional accuracy was in the range between 5 to 10 nm (section 4.5.2). This accuracy was important for analyzing the diffusion behavior of single TOM-CC molecules (Martin et al., 2002; Ober et al., 2004).
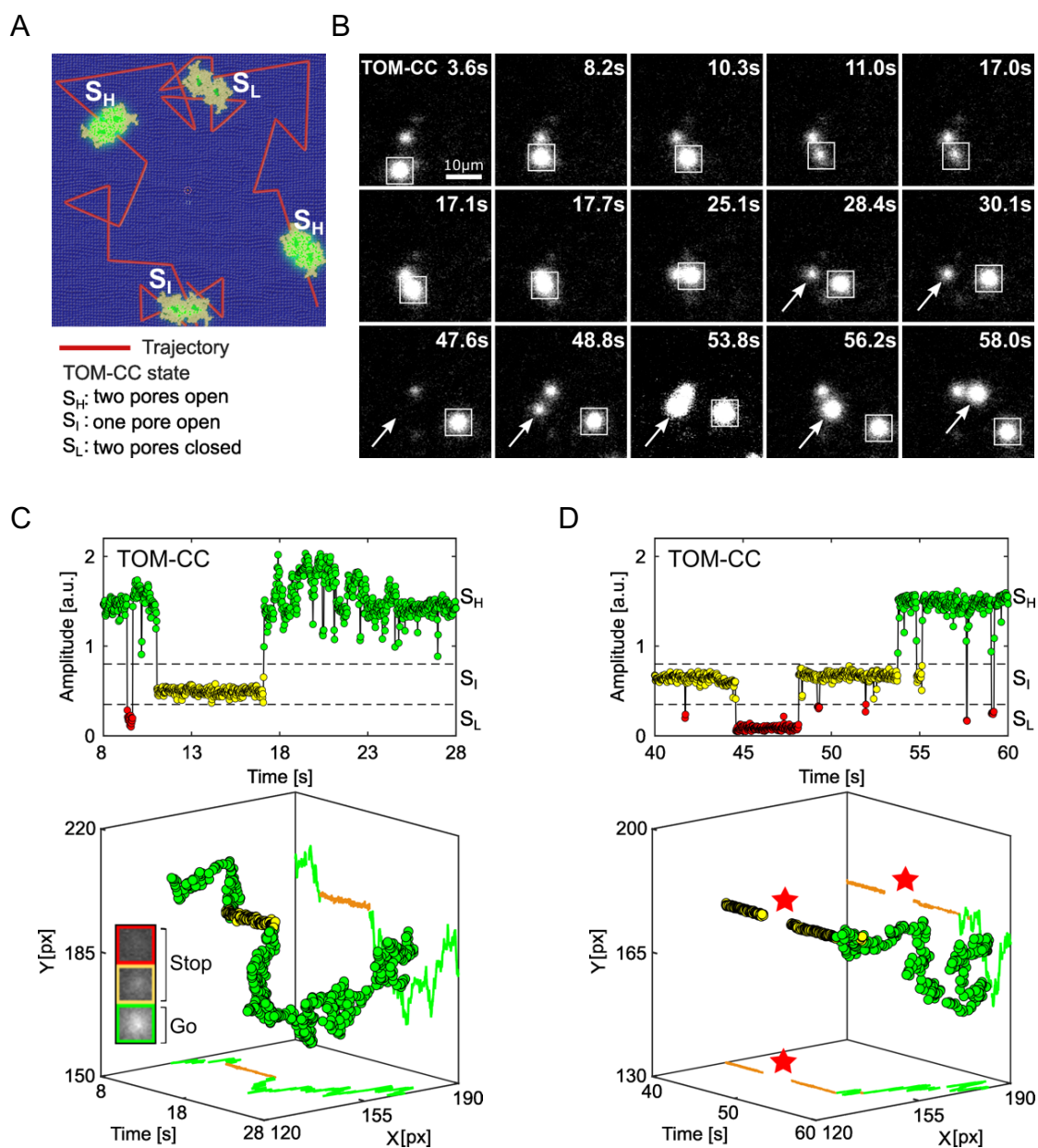
Figure 5.10: Lateral mobility correlates with the channel activity of TOM-CC. *A) Scheme for imaging both position and channel activity of single TOM-CC molecules. B) Representative TIRF microscopy images of three TOM-CC molecules reconstituted in a DIB membrane supported by unmodified agarose, acquired in a time period of 60 s. The square-marked spot displays lateral motion, interrupted by a transient arrest between t = 11.0 s and t = 17.0 s. The arrow-marked spot corresponds to a non-moving TOM-CC until t = 48.8 s. Afterwards, it starts moving. Both moving spots show high fluorescence intensity (S_H); the non-moving spots display intermediate (S_I) or dark (S_L) fluorescence intensity. C and D) Fluorescent amplitude trace and corresponding trajectory of the square- and arrow- marked TOM-CC as shown in Figure 5.10B highlighted for two different time windows. Plots on top show the change of amplitude over time, and plots on the bottom show the respective spatiotemporal dynamics for the three states. The straight lines in the trajectories indicate that the TOM-CC molecules are in a non-moving state, while the curves in the trajectories indicate that the TOM-CC molecules in mobile state.*

Comparison of the trajectories of single TOM-CC molecules with their corresponding amplitude traces reveals a direct correlation between stop-and-go movement and open-closed channel activity. Lateral diffusion of TOM-CCs in the DIB membrane is interrupted by temporary arrest, presumably due to transient linkage to the underlying agarose hydrogel. Although weak intensity profiles in S_I do not allow accurate position determination, the fluorescent spots disappear and reappear at the same spatial x,y coordinates (red stars). The higher amplitude (c, top) between t = 17.1 s and t = 25.1 s is due to the overlap between two adjacent spots. Green, TOM-CC is freely diffusive in S_H; yellow and red, immobile TOM-CC in S_I and S_L.

Figure 5.10B, which includes a series of TIRF images, shows that the opening and closing channel activity of individual TOM-CCs is coupled to lateral movements in the membrane: For the spot marked with a square, the fluorescence intensity is high in the time periods from 3.6 s to 10.3 s and 17.1 s to 58.0 s. The fluorescence intensity is intermediate in the period from 11.0 s to 17.0 s. This indicates the TOM-CC protein channels are inactive when the TOM-CC are immobilized. The spot marked with the arrow shows the same behavior as the spot marked with the square.

To further demonstrate the coupling between the lateral mobility and channel activity of TOM-CC molecules, the trajectories of individual TOM-CC molecules and their corresponding fluorescence amplitude traces were plotted, as shown in Figure 5.10C and Figure 5.10D. Both figures show that the position of fluorescent spots does not change when TOM-CC is in intermediate S_I or low S_L permeability state. Although weak intensity profiles do not allow accurate determination of the position of TOM-CC in the membrane plane, Figure 5.10D clearly shows that TOM-CC does not move in S_L; disappearance and reappearance of the fluorescent spot, switching from S_I to S_L and back to S_I, occurs at virtually the same spatial x,y-coordinates. In contrast, the trajectories of TOM-CC in high S_H permeability state demonstrate free diffusion. Further evidence of channel activity associated with lateral mobility of TOM-CC molecules is shown in Figure 5.11.
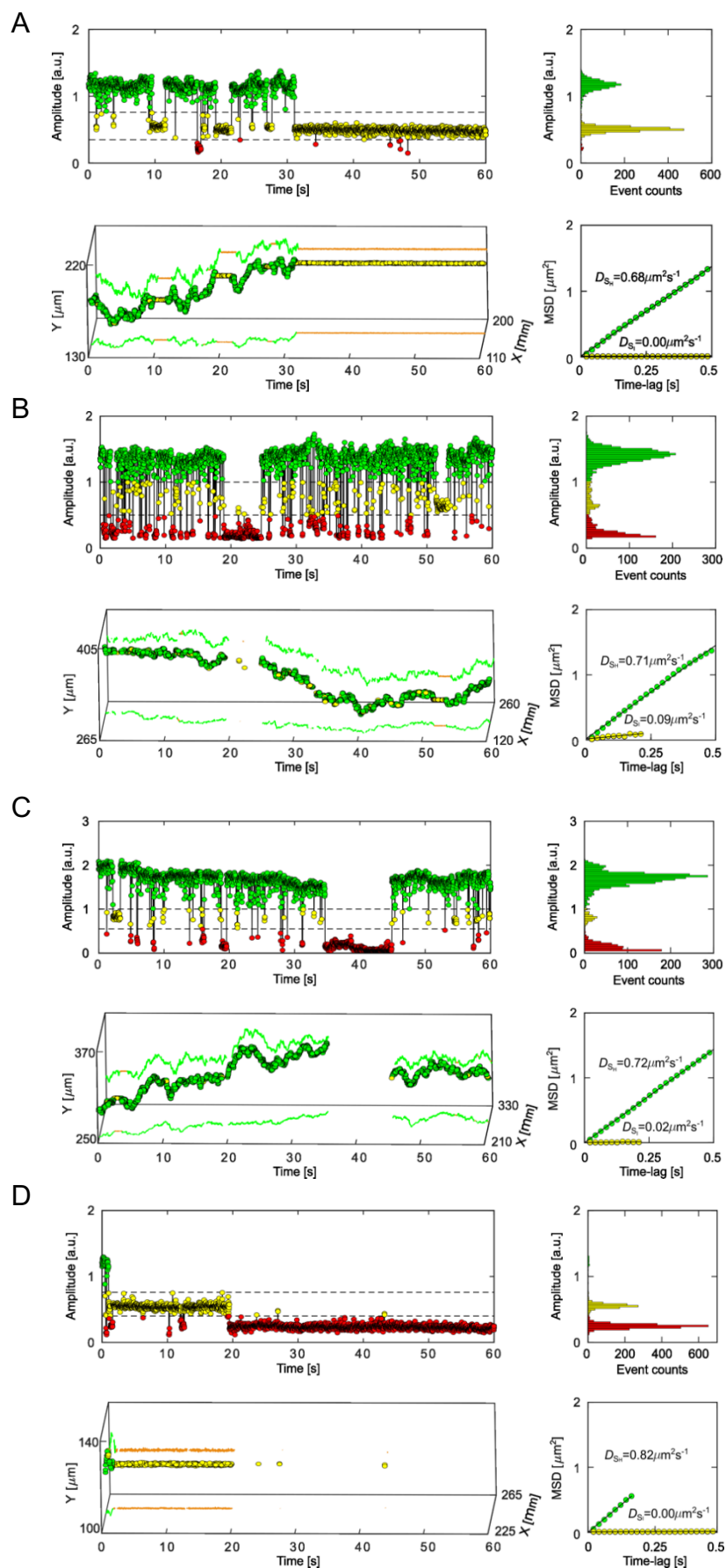
Figure 5.11: Lateral mobility correlates with the open-closed channel activity of TOM-CC. *A, B, C and D) Representative fluorescent amplitude traces of individual TOM-CC channels recorded in DIB*

57

membranes supported by unmodified agarose. The fluorescent amplitude traces (upper left) and corresponding amplitude histograms (upper right) show three distinct ion permeation states (S_H, green; S_I, yellow; S_L, red). The trajectories (bottom left) display two mobility states, moving (green) and non-moving (yellow). The time evolution of amplitude signals shows that the TOM-CC does not occupy only one of the permeability states S_H, S_I and S_L, but can switch between these three permeability states over time. The amplitude recordings and trajectories indicate that the open-closed channel activity of TOM-CC correlates with the lateral mobility of the complex. When there was no change in the x,y-coordinates (yellow straight line) of the TOM-CC trajectories, TOM-CC channels were in S_I and S_L permeability state. The mean square displacement (MSD, bottom right) increases linearly with time when TOM-CC is in S_H state. The MSD does not change with time for TOM-CC in the S_I state. Due to limited resolution, trajectory points and MSD-plots are not shown for TOM-CC in the low permeation state S_L. Pixel size [px], 0.16 μm. a.u., arbitrary unit.

To find out the mode of lateral mobility, the mean square displacements (MSD) of the TOM-CC molecules were plotted against time (Figure 5.11). Since the MSD scales linearly with time, it can be concluded that TOM-CC follows the law of Brownian motion. Following this mode of diffusion, the diffusion coefficients of the TOM-CC (Figure 5.11) were determined from time-averaged mean squared displacements as $D(S_I) = D(S_L) \leq D_{min} = 0.01$ μm²s⁻¹ and $D(S_H) \simeq 0.85 \pm 0.16$ (*mean* ± *SEM*, *n* = 46) in states S_I and S_H, respectively. TOM-CC molecules, that revealed diffusion constants less or equal than D_{min}, were defined as immobilized.

The results show that the TOM-CC molecules are in the active state (S_H) during the free diffusion mode and in the inactive state (S_I and S_L) during the immobile mode. The diffusion coefficient $D(S_H)$ in diffusive mode corresponds to typical values of mobile Tom40 (D_{Tom40} ~0.5 μm² s⁻¹) and Tom7 (D_{Tom7} ~0.7 μm² s⁻¹) in native mitochondrial membranes (Sukhorukov et al., 2010; Kuzmenko et al., 2011). It is comparable to that of transmembrane proteins in plasma membranes lined by cytoskeletal networks (for review, see Jacobson et al., 2019). The diffusion coefficient $D(S_L)$ of TOM-CC in S_L state could not always be reliably determined due to its extremely low intensity level. The mean square displacement (MSD $\langle r^2 \rangle$) of TOM-CC calculated over delay times longer than ~1 s typically showed subdiffusive behavior with $\langle r^2 \rangle \propto \tau^\alpha$ and $\alpha < 1$ (Figure 5.12), which was fully in line with the observed *stop-and-go* behavior.
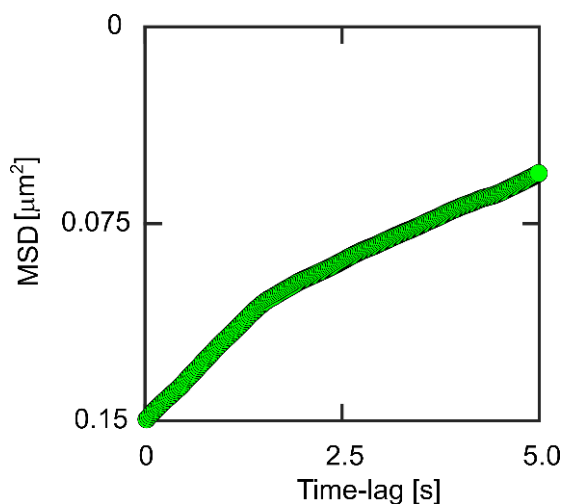
Figure 5.12: Subdiffusion of TOM-CC in DIBs. *The mean square displacement (MSD) increases linearly with time when TOM-CC is in S_H state tracked for short periods of time $\tau < \tau_{max} = 1.56\, s$ but shows non-linear behavior for $\tau > \tau_{max}$, indicating confined or restricted diffusion caused by interactions with the agarose hydrogel adjacent to the membrane. τ_{max} was given by the mesh size of the agarose hydrogel below the DIB membrane. MSD against τ was calculated from the data shown in Figure 5.11A.*

5.3 Structural subunits of TOM-CC acting as 'mechanosensitive switches' for channel opening

In section 5.2, it was shown that TOM-CC channels can switch between three different ion permeability states and that these permeability states correlate with lateral movement of TOM-CC in the membrane. Since the two Tom22 subunits in the center of the TOM-CC (Figure 3.2) protrude significantly from the membrane plane into the intramembrane space (IMS), I hypothesized that Tom22 acts as a mechanosensitive switch that determines the lateral mobility of the TOM-CC, thereby causing transitions between open (S_H) and closed (S_I and S_L) conformations of the two TOM-CC pores.

Before testing this hypothesis, the lateral mobility of fluorescently labeled TOM-CC itself was first examined to rule out the influence of Ca^{2+}-Fluo-8 fluorescent clouds on the positioning of TOM-CC molecules. Subsequently, Ca^{2+} ion flux through monomeric Tom40, and two unrelated protein channels (bacterial OmpF and α-hemolysin) were monitored over time. Tom40, OmpF and α-HL do not contain a subunit that protrudes on the cis side of the DIB membrane. To provide further evidence that Tom22 can act as a mechanosensitive switch, the

supporting agarose layer was modified with functional Ni-NTA groups to specifically bind TOM-CC to the hydrogel via this receptor. Finally, the coupling between the channel activity and lateral mobility of TOM-CC was statistically analyzed.

5.3.1 Lateral mobility of fluorescently labeled TOM-CC

Ca^{2+} flux though individual TOM-CC pores were measured by monitoring Fluo-8 emission in close proximity to the membrane using TIRF microscope, showing instantaneous opening and closing activity of TOM-CC and its corresponding lateral movement. Since the Ca^{2+}-Fluo-8 fluorescent cloud in the vicinity of the TOM-CC channel did not directly come from TOM-CC itself, TOM-CC was covalently labeled with Cy3-maleimide (Figure 5.3) to verify that TOM-CC itself shows '*stop-and-go'* dynamics.

Labeled TOM-CCs (section 4.2.5) were reconstituted into a DIB membrane. To avoid excessive background noise due to non-integrated Cy3-TOM-CC, the concentration of Cy3-TOM-CC in the aqueous droplet was optimized to ~0.5 nM. Due to the limited number of Cy3 maleimide dyes labeled on TOM-CC, the acquisition time was set to a maximum of 1 minute to avoid photobleaching.

As shown in Figure 13A, individual Cy3-TOM-CC molecules can be tracked in the membrane over time as sharp fluorescent spots. One freely moving TOM-CC molecule stops at the same spatial x,y position when it crosses the same position a second time, indicating a specific molecular trap or anchor point at this position below the membrane. Thus, Cy3-TOM-CC shows a similar *stop-and-go* behavior as unlabeled TOM-CC channel (Figure 5.10B).

To further validate the '*stop-and-go'* behavior of Cy3-TOM-CC in DIB membranes, trajectories obtained from additional n = 15 molecules were recorded (section 4.5.1). Figures 5.13B - E show the trajectories of four molecules. They show again that TOM-CC changes between moving and non-moving states over time.
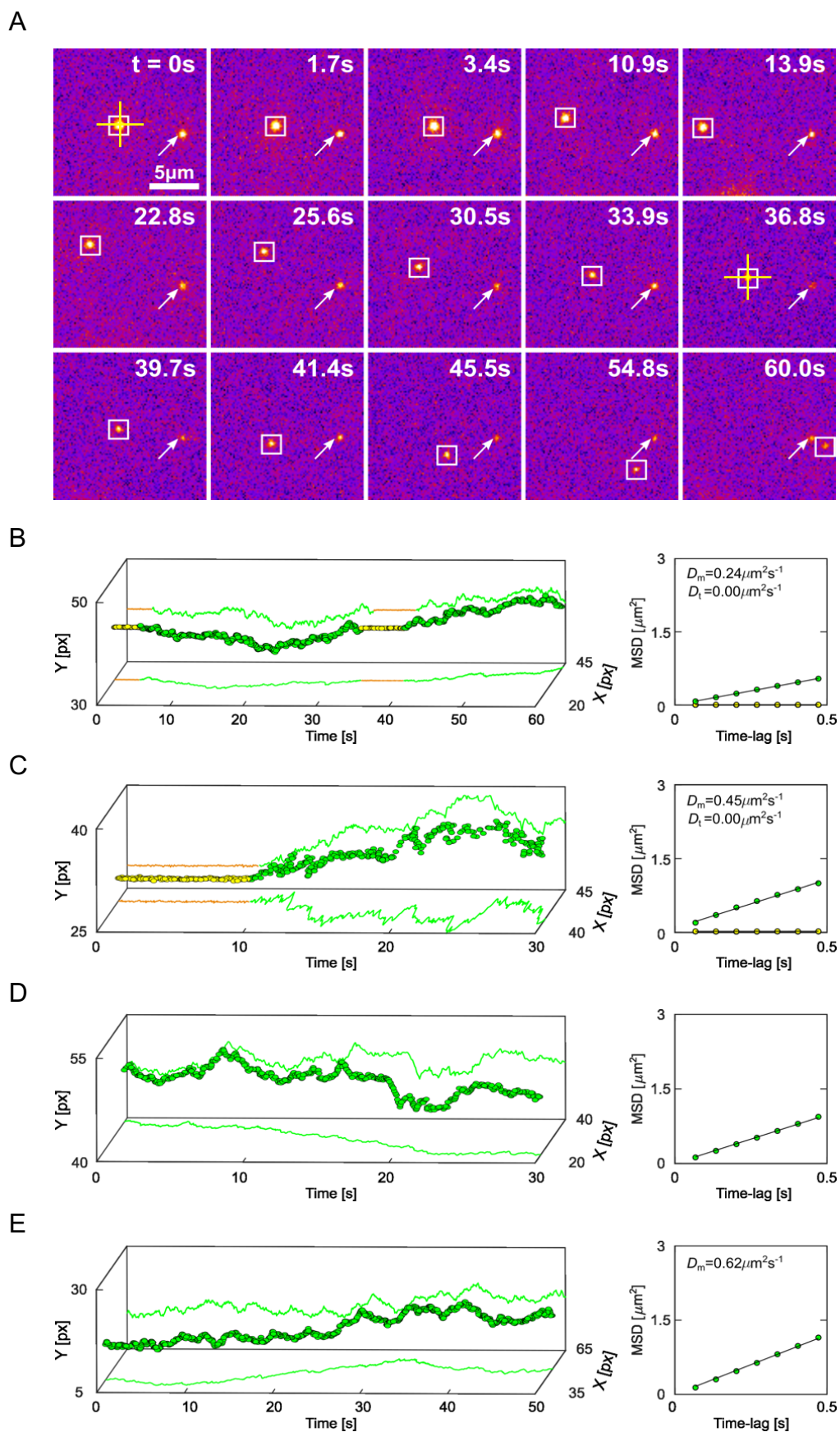
A

B

C

D

E

Figure 5.13: Tracking fluorescent-labeled TOM-CC in DIB membranes. *A) Representative TIRF microscopy images of a DIB membrane with two Cy3-labeled TOM-CC molecules (n = 15) taken from*

61

a time series of 60 s. Individual image frames of the membrane were recorded under 561 nm laser light at a frame rate of 14.87 s⁻¹ and an exposure time of 31 ms. The square-marked spot displays lateral motion, interrupted by a transient arrest between t = 0 s and t = 3.3 s, and between t = 33.9 s and t = 39.4 s. The arrow-marked spot corresponds to a non-moving TOM-CC. Raw image data are shown. Grey scales of individual images are transformed into pseudo color images to better display movement of fluorescently labeled TOM-CC molecules. B) Trajectory and diffusion coefficients of the square marked Cy3-TOM-CC in Figure 5.11A. C, D and E) Trajectories and diffusion coefficients of additional Cy3-TOM-CCs. The yellow straight lines in the trajectories indicate TOM-CC molecules in a non-moving state, while the green curves in the trajectories indicate moving TOM-CC. The mean square displacement (MSD, bottom right) increases linearly with time for moving TOM-CCs. The MSD does not change with time for non-moving TOM-CCs. Note that the freely moving TOM-CC molecule in Figures 5.13A and B stops at the same spatial x,y-position when it sweeps this position a second time, indicating a specific molecular trap or anchor point at this position (yellow cross) below the membrane. Pixel size [px], 0.16 μm.

In good agreement with the diffusion coefficients of unlabeled TOM-CC molecules (Figure 5.11), diffusion constants of $D_{Cy3} \simeq 0.36 \pm 0.08$ μm² s⁻¹ (mean ± SEM, $n = 15$) and $D_{Cy3} \leq D_{min} = 0.01$ μm²s⁻¹ for moving and transiently trapped particles were obtained, respectively (Figures 5.13B - E, right).

5.3.2 Visualizing the correlation between channel permeability and lateral mobility of Tom40

In contrast to TOM core complex (Figure 5.2A), its channel forming subunits Tom40 (Figure 5.14A) are entirely embedded in lipid membranes.

To prove the hypothesis that lateral mobility and thus permeability of the core complex are regulated by the interaction of Tom22 with structures below the membrane, Tom40 was isolated from *N. crassa* mitochondria (section 4.2.3). Figure 5.14B shows the elution profile of Tom40 in n-octyl-β-D-glucopyranoside (OG) containing buffer eluted from a Ni-NTA column. Tom22 is eluted with 300 mM imidazole in A1 buffer (Table 4.6). Analysis of the fractions corresponding to the first peak by SDS-PAGE followed by Coomassie blue staining shows virtually pure Tom40 (Figure 5.14C).

Subsequently, isolated Tom40 proteins were reconstituted into DIB membranes supported by unmodified agarose (Figure 5.8) and analyzed by TIRF microscopy the same way as TOM-CC (Figure 4.2).
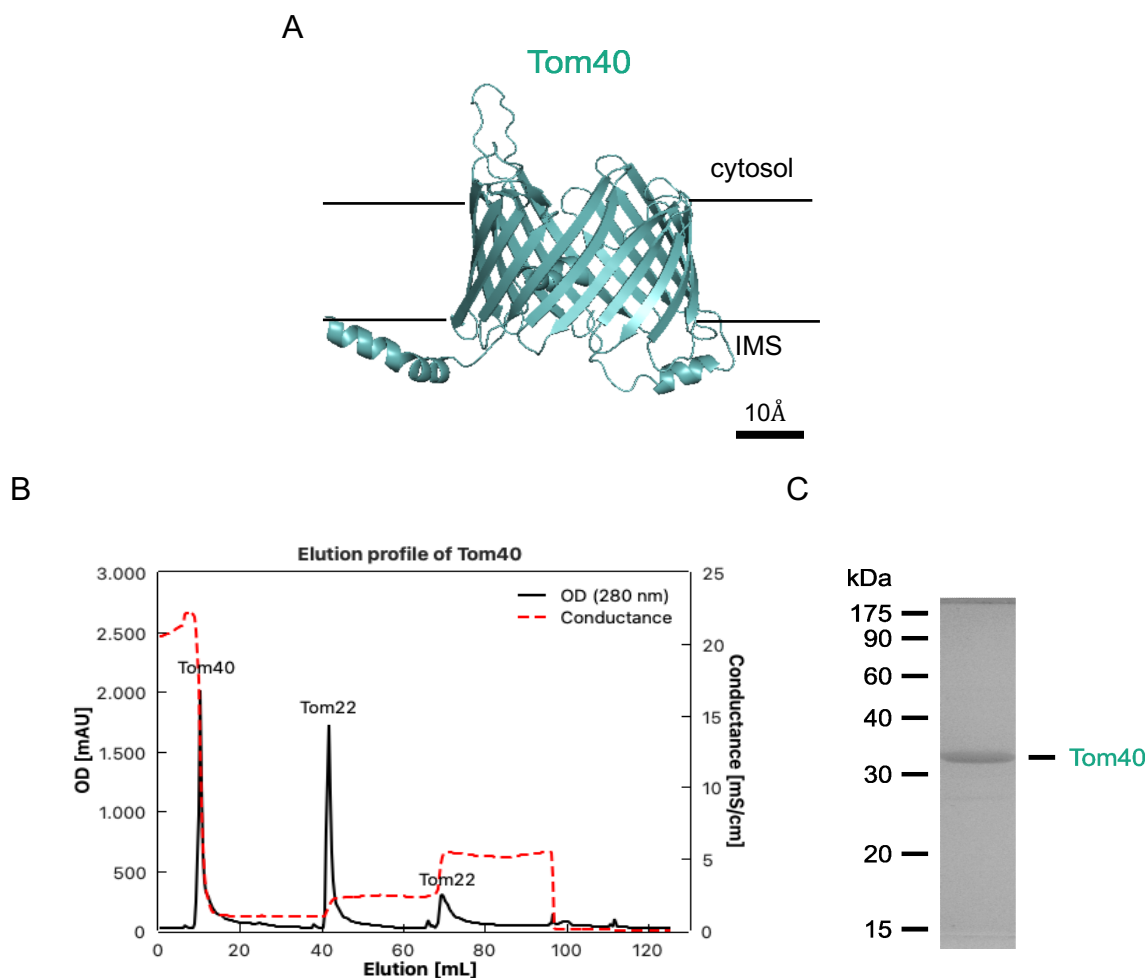

Figure 5.14: Purification of Tom40. *A) Side view of the cryo-EM structure of β-barrel N. crassa Tom40 (EMDB, EMD-3761; (Bausewein et al., 2017, 2020)). Tom40 forms a transmembrane β barrel with 19 antiparallel β-strands. B) Mitochondrial membranes (~2 g) were solubilized in n-dodecyl-β-D-maltoside (DDM) and loaded onto a Ni-NTA column at 1 mL/min in 0.1 % (w/v) n-dodecyl-D-maltoside, 10 % (w/v) glycerol, 20 mM Tris (pH 8.5) and 1 mM PMSF. Tom40 was eluted from the column at 0.05 mL/min in 3 % (w/v) n-octyl-β-D-glucopyranoside, 2 % (v/v) DMSO and 20 mM Tris (pH 8.5). Tom40 was separated from the other subunits and eluted in the first peak. Tom22 were eluted successively in the second and third peaks with 300 mM and 1 M imidazole, respectively. C) Analysis of purified Tom40 by SDS-PAGE and Coomassie Blue staining. The gel reveals the Tom40 band.*

Tom40 molecules appeared as high-contrast fluorescent spots (Figure 5.15A). In order to quantify the channel activity and lateral mobility of Tom40, TIRF images were corrected for fluorescence bleach and fluorescence spots were fitted to 2D symmetric Gaussians described in

section 4.5.1. The trajectories of Tom40 (Figure 5.15B) show the most elementary mode of mobility expected for homogeneous membranes: simple Brownian translational diffusion.

Further examples are shown in figures 5.16A - D. The fluorescence amplitudes are constant over time. This indicates that the DIB membrane does not fluctuate significantly in the evanescent field which is responsible for excitation of the Fluo-8 dyes near the membrane. In addition, unlike TOM-CC, none of the Tom40 protein channels exhibit gating transitions between specific permeability states. Tom40 shows only one permeability state. The trajectories indicate free diffusion. In contrast to TOM-CC, Tom40 movement does not appear to be disrupted by brief periods of transient arrest.

Consistent with typical values for monomeric proteins in homogenous lipid membranes (Koppel et al., 1981; Ramadurai et al., 2009), the lateral diffusion coefficient of Tom40 was determined as $D_{Tom40} \simeq 1.49 \pm 0.21$ μm^2 s^{-1} (mean $\pm$ SEM, $n = 20$). This result supported the initial hypothesis that the non-membrane domains of Tom22 are responsible for the transient arrest of TOM-CC in agarose-supported bilayers, as the Tom7, Tom6, and Tom5 subunits are also fully embedded in the membrane (Figure 5.2) (Bausewein et al., 2017, 2020) and are very unlikely interacting with the hydrogel below the DIB membranes.
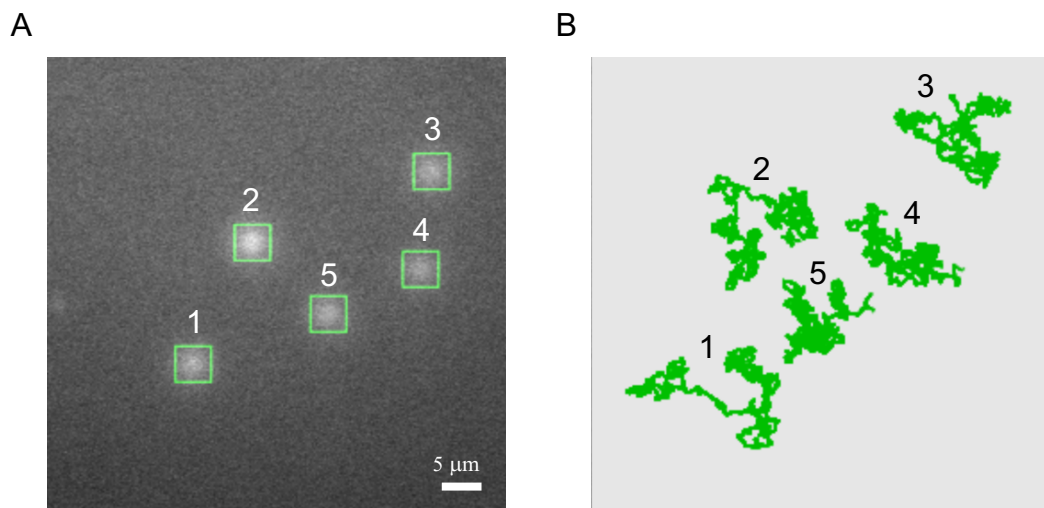

Figure 5.15: Fluorescence intensities and trajectories of Tom40 molecules reconstituted in DIB membrane. *A) TIRF image of single isolated Tom40 molecules acquired as described in Figure 4.2. The green square marked Tom40 molecules display almost identical Fluo-8 fluorescence intensities, indicating the same ion permeation state. B) Trajectories of Tom40. The trajectories were obtained from a 1-minute recording of the spots shown in (A). Tom40 molecules are freely moving. Pixel size, 0.16 μm; recording time, 1 min; frame rate, 47.5 s^{-1}.*
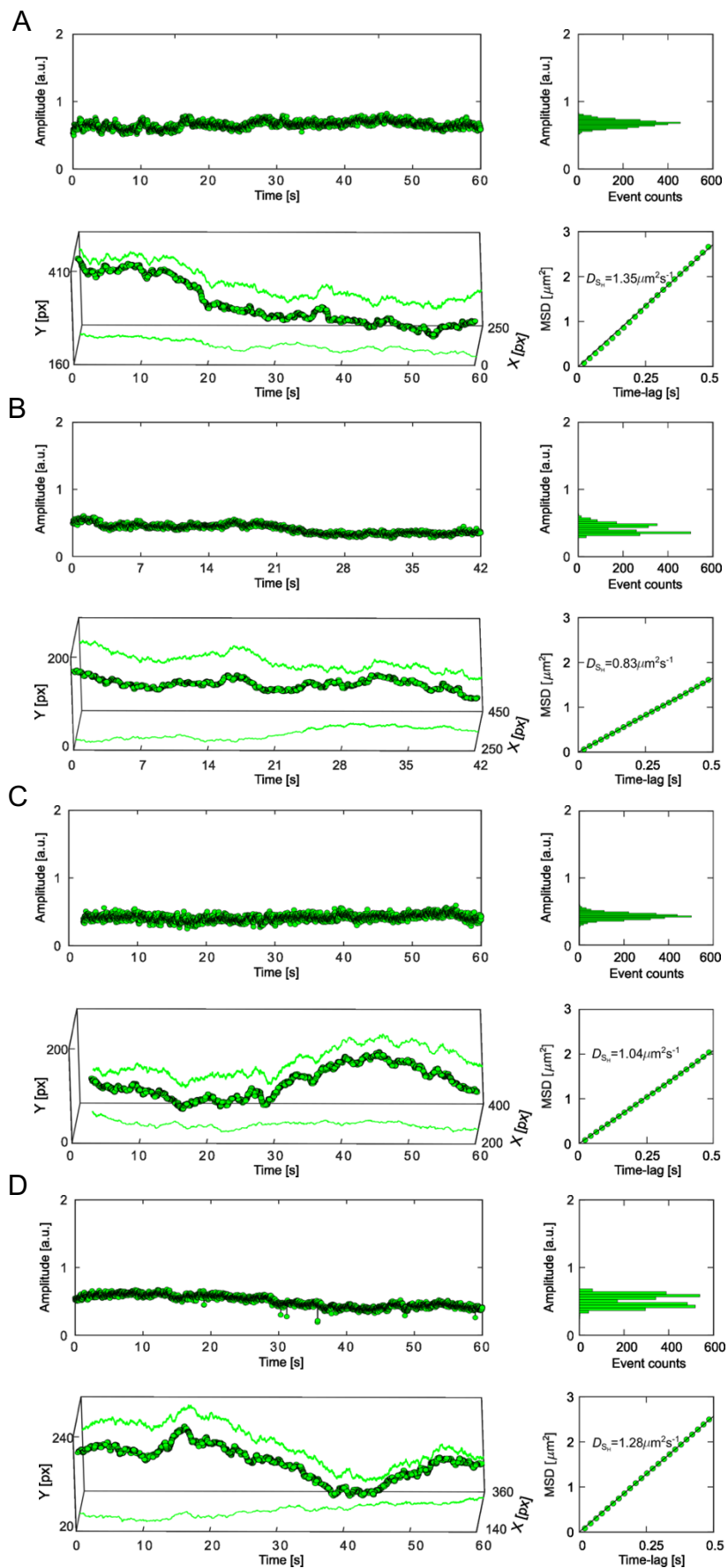
Figure 5.16: Lateral movement and channel activity of single Tom40 molecules. *A, B, C and D)*
Representative fluorescence amplitude traces (top left) and trajectories (bottom left) of individual

Tom40 channels recorded in agarose supported DIB membranes. Comparing the fluorescent amplitude of Tom40 with that of TOM-CC (Figure 5.9D, Figure 5.10C - D and Figure 5.11), the fluorescent amplitude of Tom40 is about half of the high fluorescent amplitude of TOM-CC. The fluorescence amplitude histograms (top right) show one peak, respectively, demonstrating that Tom40 has one permeation state. The mean square displacement (MSD, bottom right) of Tom40 increases linearly with time, indicating unrestricted motion. Pixel size [px], 0.16 µm; frame rate, 47.5 s⁻¹; a.u., arbitrary unit.

5.3.3 Visualizing the correlation between the permeability states and lateral mobility of OmpF

In addition to TOM-CC and Tom40 analyzed above (Figures 5.2A and 5.14A), a completely unrelated β-barrel protein (OmpF) (Benz, 2006) was studied in DIB membranes. Based on its structure, it was expected to behave similarly to Tom40 in DIB membranes and further support the conclusion made in the previous section.
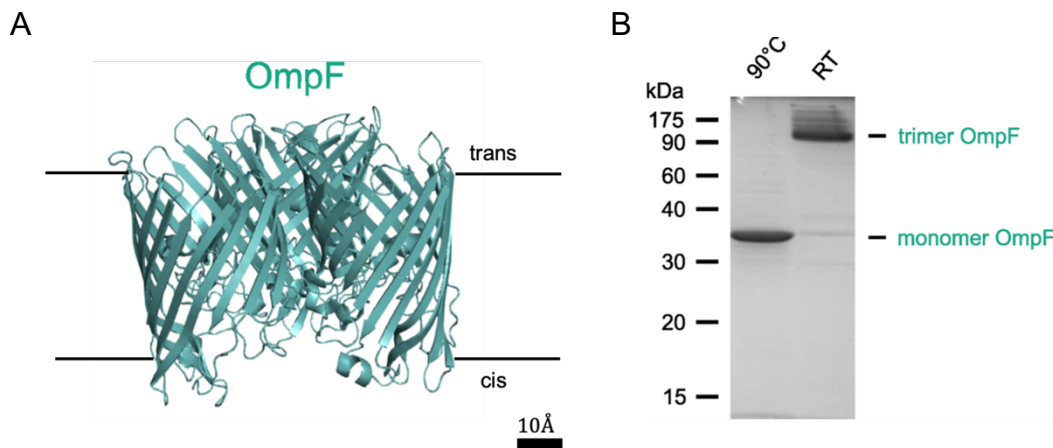

Figure 5.17: Purification of OmpF. *A) Atomic model of three β-barrel pores outer membrane protein F (OmpF) from E. coli (PDB, 1OPF, (Cowan et al., 1995)). Each monomer is folded as a 16-stranded β-barrel. B) Escherichia coli strain BE BL21(DE3) omp6, lacking both LamB and OmpC (Bieligmeyer et al., 2016) was used to isolate OmpF. Heated OmpF and non-heated OmpF were loaded onto a 14 % (w/v) acrylamide SDS gel followed by Coomassie Blue staining. When OmpF was heated to 90°C, the oligomer disassociated into monomers.*

In contrast to TOM-CC, OmpF forms a three-pore channel (Figure 5.17A) which is fully embedded in the membrane. Nevertheless, the structure of one of its β-barrel pores with 16 β-strands is similar to that of Tom40 with 19 β-strands (Cowan et al., 1992, 1995; Bausewein et al., 2017). The inner barrel contains an α-helical segment that stabilizes the β-barrel pores.

66

Furthermore, the inner pore size of OmpF (~0.7 nm x 2.2 nm) (Cowan et al., 1995; Kefala et al., 2010) is similar to that of Tom40 (~1.1 nm x 3.2 nm) (Hill et al., 1998; Bausewein et al., 2017).

OmpF was isolated from *E. coli* (section 4.2.4). The isolated OmpF was analyzed by SDS-PAGE (Figure 5.17B). At 90°C, it dissociates into monomers, while at room temperature it retains its three β-barrel pore structure, consistent with previous work (Nakae et al., 1979). Subsequently, the purified OmpF was reconstituted in DIB membranes (Figure 5.1) and examined by TIRF microscopy in the same manner as TOM-CC and Tom40 (Figure 4.2). The channel activity and lateral mobility of OmpF were analyzed as described in section 4.5.1. As shown in Figure 5.18A, the fluorescent spots of OmpF show similar intensities.
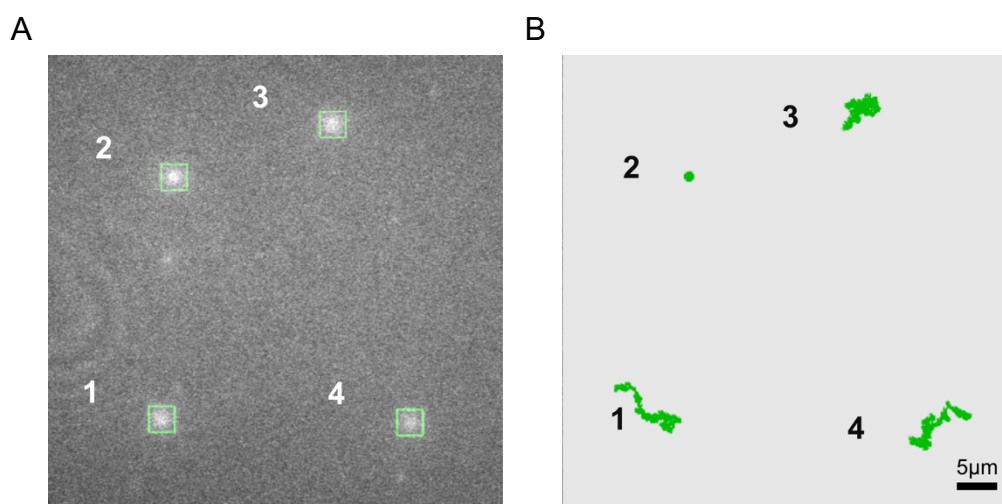

Figure 5.18: Fluorescence intensities and trajectories of OmpF in a DIB membrane. *A) TIRF image of isolated OmpF molecules acquired as described in Figure 4.2. The OmpF molecules marked with green squares show almost the same Fluo-8 fluorescence intensity. They occupy the same ion permeation state. B) Trajectories of OmpF. OmpF channels are freely moving (#1, #3, #4) and non-moving (#2). The majority of OmpF are freely diffusing, which is consistent with the fact that OmpF is fully embedded in membranes and does not interact with the hydrogel below the DIB membrane. Recording time, 1 min; frame rate, 47.5 s^{-1}.*

Compared to Tom40 (Figure 5.15B), Figure 5.18B shows three freely diffusing OmpF molecules and one permanently trapped OmpF channel. In contrast to TOM-CC (Figure 5.9D), and in line with Tom40 (Figure 5.16), the corresponding fluorescence amplitudes of OmpF are constant over time. This indicates that the ion permeability of OmpF is not affected by motion or trapping.
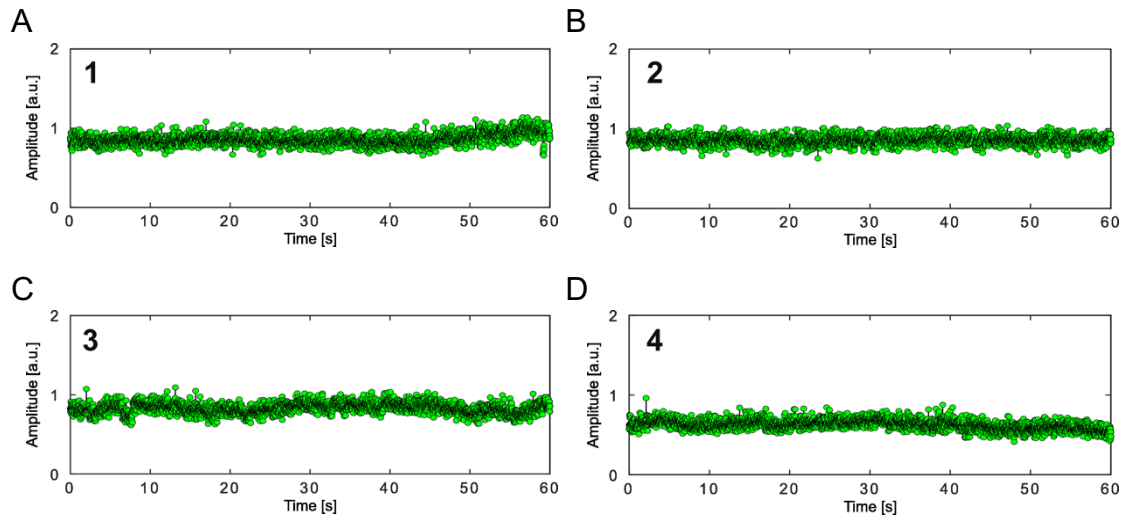
67

Figure 5.19: Moving and non-moving OmpF molecules show similar channel activity. *A, B, C and D) Fluorescent amplitude traces of OmpF channels #1 - #4 shown in Figure 5.18. The amplitude traces show that the channel activity of OmpF is similar for the moving (#1, #3 and #4) and non-moving (#2) OmpF molecules. It further demonstrates that the different mobility states did not trigger the OmpF channels gating transitions. A total of n = 125 moving and n = 21 permanently trapped molecules were analyzed. Original fluorescence intensities were recorded at a frame rate of 47.51 s^{-1}. a.u., arbitrary unit.*

Additional examples of freely moving and transiently trapped OmpF are shown in Figures 5.19 and 5.20. Again, the fluorescent amplitudes are constant over time. The lateral diffusion coefficient of freely moving OmpF was determined as $D_{OmpF} \simeq 1.16 \pm 0.07$ µm^2 s^{-1} (mean $\pm$ SEM, *n* = 42, Figures 5.19A, C, D and 5.20), again in agreement with typical values of multimeric proteins in lipid membranes (Koppel et al., 1981; Ramadurai et al., 2009).

Analysis of *n* = 171 OmpF molecules revealed that ~12 % were permanently trapped and ~15 % were transiently trapped (Figure 5.18B and Figure 5.21). The majority of 63 % were freely diffusing, consistent with the fact that OmpF is fully embedded in the membrane (Benz, 2006). A stochastic stop did not appear to be associated with a change in intensity (Figure 5.18B and Figure 5.21) and thus with the closing of one of its pores. Since the data for OmpF were recorded in the same manner as for TOM-CC, this result suggests that the experimental setup established in this work was not responsible for the opening and closing of the TOM-CC channels.
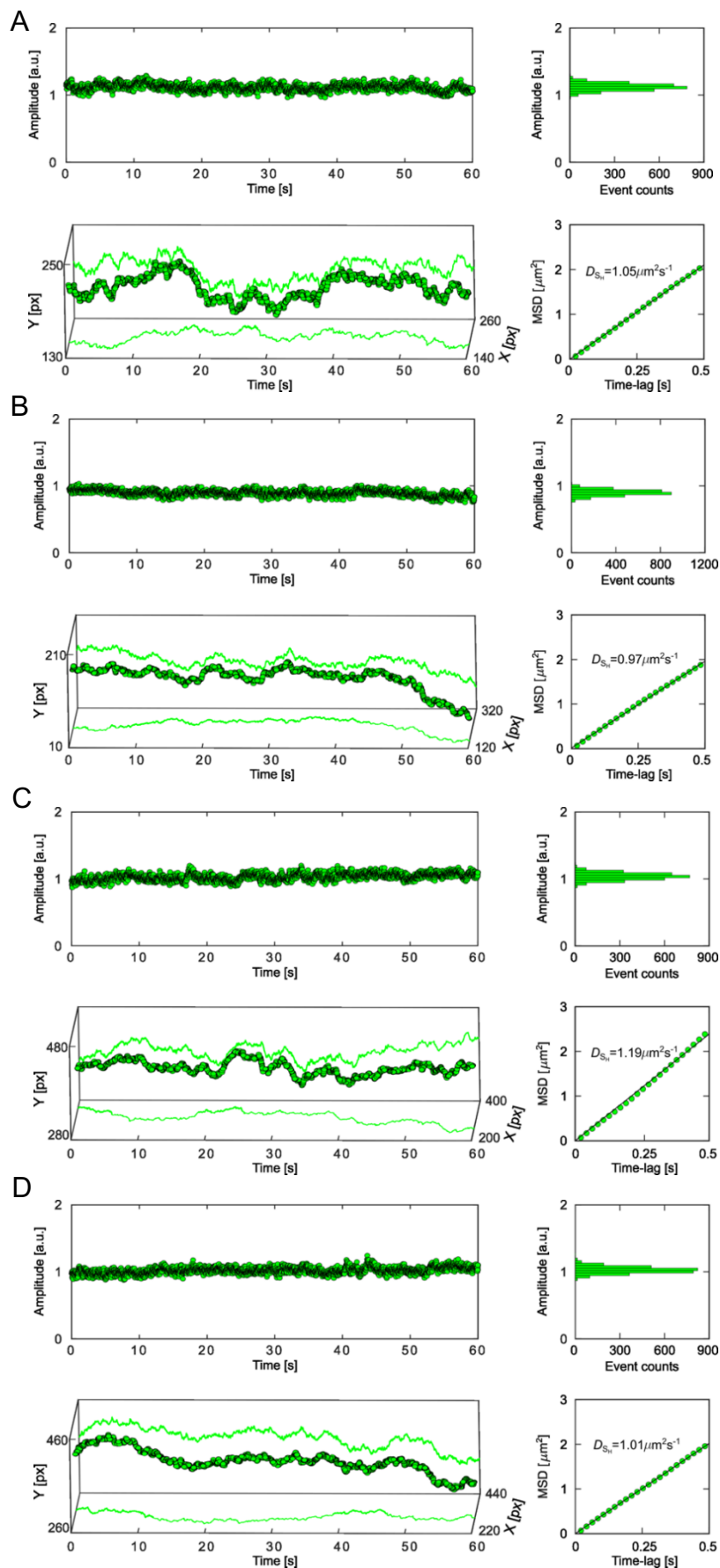
Figure 5.20: Moving OmpF molecules show constant channel activity over time. *A, B, C and D)*
Representative fluorescent amplitude traces and trajectories of individual OmpF channels (n = 125)

69

recorded in DIB membranes. The amplitude tracing (top left) and its corresponding histogram (top right) indicate one ion permeation state, even though OmpF has three pores. The corresponding trajectories (bottom left) indicate free diffusion. The mean square displacement (MSD, bottom right) increases linearly with time, indicating diffusion coefficients of ~1 $\mu m^2 s^{-1}$. Pixel size [px], 0.16 μm; a.u., arbitrary unit; frame rate of 47.51 s^{-1}.
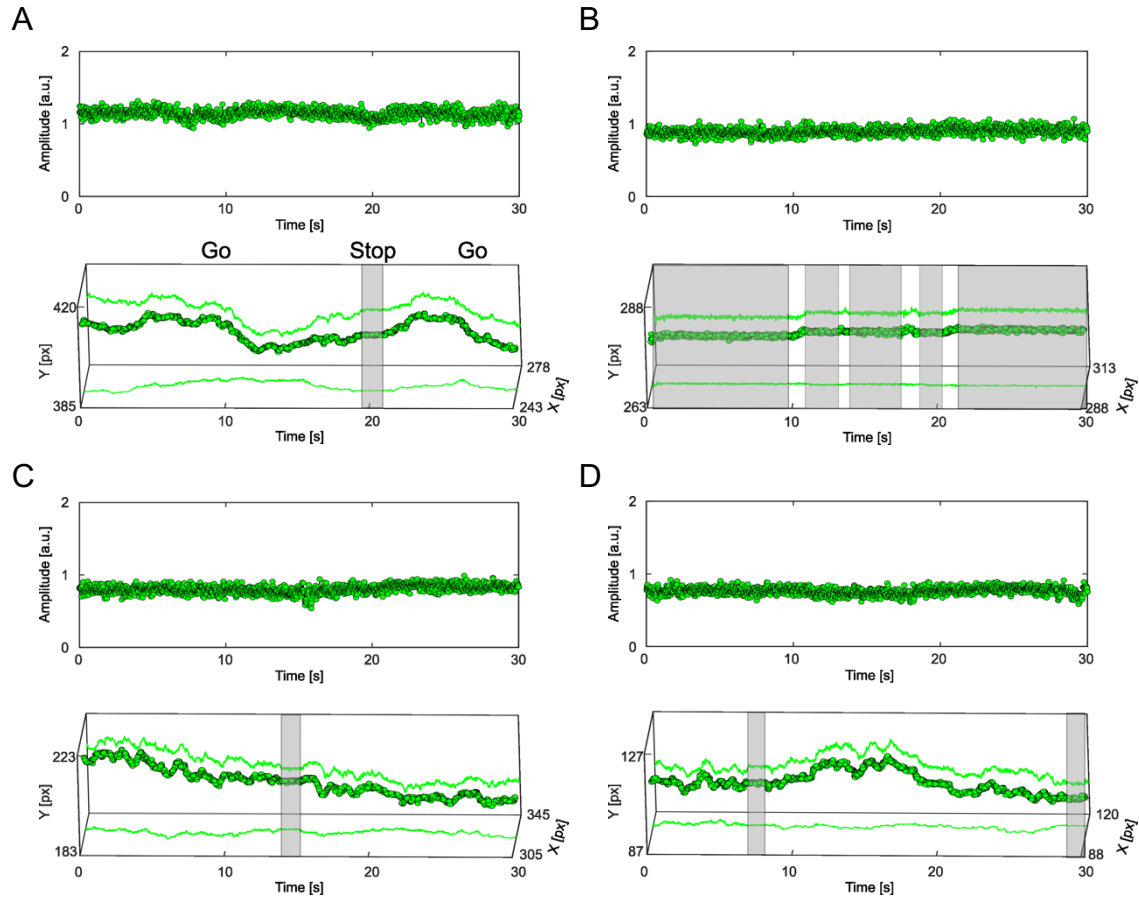
Figure 5.21: Stop-and-go movement does not influence OmpF channel activity. *A, B, C and D) Representative fluorescent amplitude traces and corresponding trajectories of transiently trapped OmpF channels (n = 25) recorded in DIB membranes. OmpF shows only one amplitude level, regardless of whether it is in motion or trapped. The trajectory segments corresponding to the time periods of trapped, non-moving molecules are marked in grey. Pixel size [px], 0.16 μm; a.u., arbitrary unit; frame rate of 47.51 s^{-1}.*

5.3.4 Visualizing the correlation between the permeability states and lateral mobility of α-hemolysin

A classical ion channel used as a standard in electrophysiological experiments is the bacterial toxin α-hemolysin (αHL) of the human pathogen *Staphylococcus aureus* (Kasianowicz et al., 1996; Gu et al., 1999; Braha et al., 2000; Howorka et al., 2001; Stoddart et al., 2010). It is

secreted by the bacterium as a water-soluble monomer with a β-hairpin that assembles into heptamers in eukaryotic membranes, forming transmembrane β-barrel pores (for review, see Bhakdi and Tranum-Jensen, 1991; Song et al., 1996; Sugawara et al., 2015). A αHL has a length of 10 nm and ranges from 1.4 to 4.6 nm in diameter (Figure 5.22A) (Song et al., 1996). Based on the electrophysiology experiments, it is well-established that αHL is stable and highly conductive at both low and high voltages (Menestrina, 1986). Therefore, in addition to Tom40 and OmpF, αHL was also used as a reference for TOM-CC. Again, in contrast to TOM-CC, the Ca^{2+} flux through an open hemolysin pore was assumed to be constant over time.
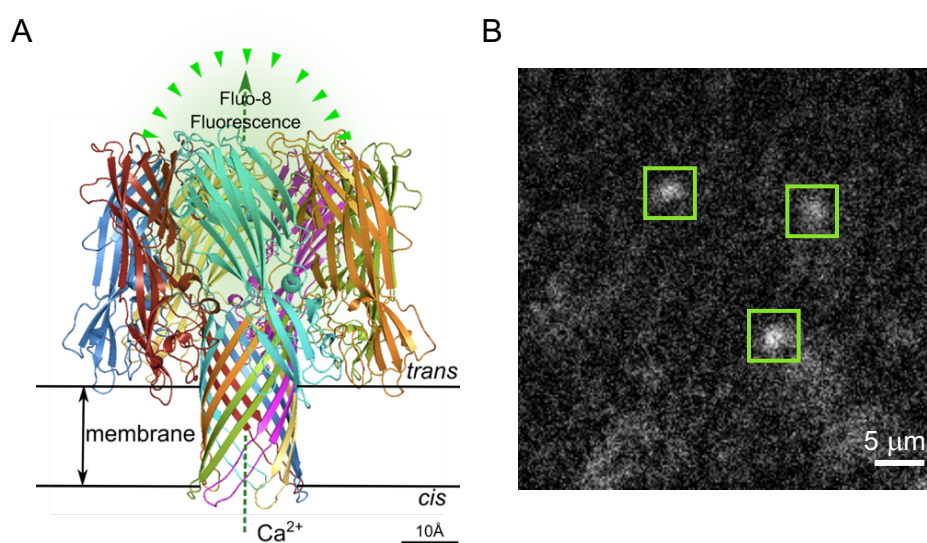
Figure 5.22: Tracking single hemolysin molecules and imaging their ion channel activity. A) Atomic model based on the X-ray crystallography of Staphylococcus aureus hemolysin (PDB, 7AHL, Song et al., 1996). The ionic pathway through the one aqueous β-barrel hemolysin pore is used to optically study its ion permeability. B) TIRF image of hemolysin molecules in a DIB membrane. The green square marked spots show almost identical fluorescence intensities.

α-Hemolysin (Figure 5.22A) was reconstituted in DIB membranes as described for TOM-CC, Tom40 and OmpF, and Ca^{2+}-flux through individual pores was measured by monitoring Fluo-8 fluorescence emission adjacent to the membrane (Figure 5.22A). Surprisingly, the Fluo-8 signal corresponding to α-hemolysin (Figure 5.22B) was much weaker and noisier than that of TOM-CC, Tom40, and OmpF. Nevertheless, as expected, α-hemolysin occupied only one ion permeability state (Figures 5.23A - D, top left). The trajectories showed Brownian translational diffusion (Figures 5.23A - D, bottom left), indicating that the molecules with the transmembrane β-barrel pore entered the DIB membranes first, while the crown of the protein remained on the side of the aqueous droplet. The diffusion coefficient of hemolysin was determined as $D_{αHL} \simeq 0.57 \pm 0.06$ μm^2 s^{-1} (mean $\pm$ SEM, $n = 30$, Figure 5.23).
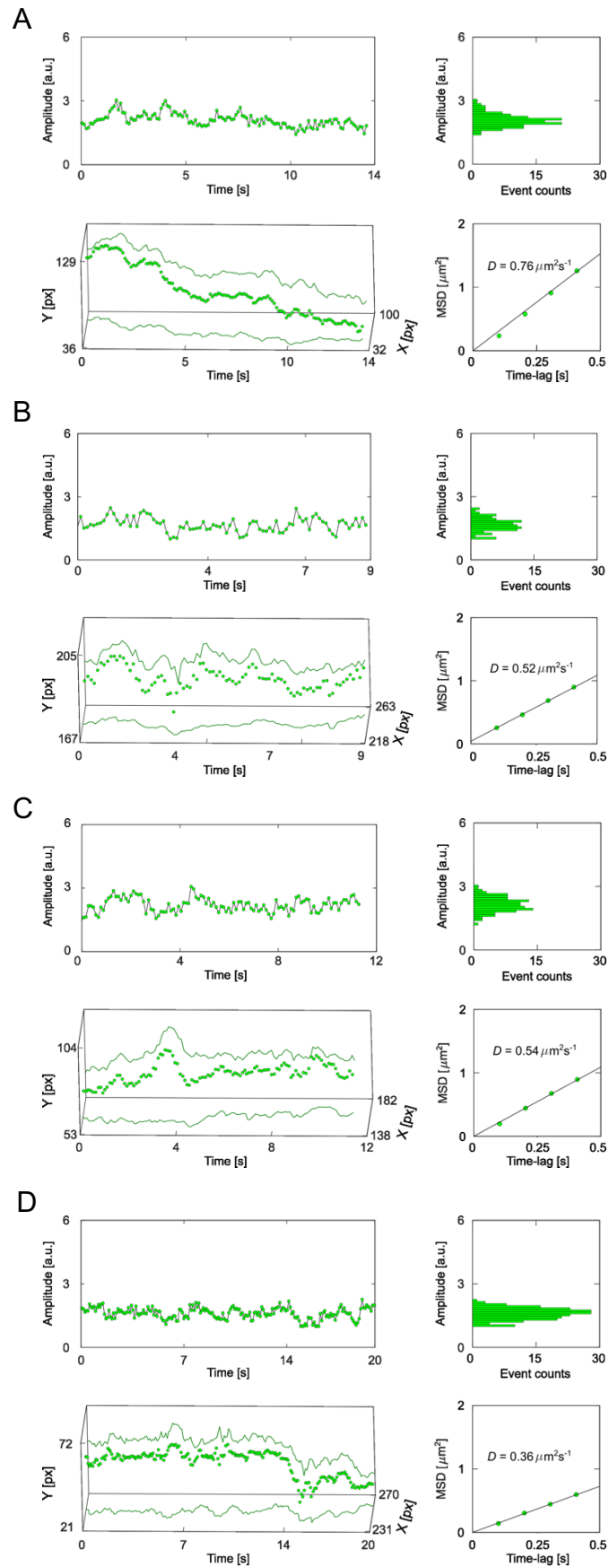
Figure 5.23: Moving hemolysin molecules show constant channel activity over time. *A, B, C and D)*
Representative fluorescent amplitude traces (top left) and trajectories (bottom left) of individual

hemolysin channels (n = 30) recorded in DIB membranes. Fluorescent amplitude traces of hemolysin channels show only one clear amplitude level, although amplitudes are slightly changing over time. Trajectories present that hemolysins are always moving over time. Fluorescence amplitude histogram of the hemolysin (top right) shows one peak, also demonstrating that hemolysin occupied only one permeation state; the mean square displacement (MSD, bottom right) increases linearly with time, proving that hemolysin is always in freely diffusing state. Pixel size [px], 0.16 μm. a.u., arbitrary unit.

5.3.5 Visualizing the effect of controlled TOM-CC immobilization on channel activity

To address the question of whether Tom22 acts as a "light switch" regulating the opening/closing probability of the TOM-CC, the agarose hydrogel under the membrane was replaced with Ni-NTA-modified agarose to fix Tom22 via a C-terminal histidine tag (Figure 5.24A). Binding of 6xHis-Tom22 to Ni-NTA was expected to result in permanent anchoring of the TOM-CC in the hydrogel, leading to closure of its Tom40 pores. Binding of two Tom22 subunits to Ni-NTA-modified agarose should cause closure of two Tom40 pores. Binding of one Tom22 to Ni-NTA should result in the closure of one Tom40 pore. If Tom22 did not bind to Ni-NTA, it would be diffusive and both Tom40 channels would be open. In this case, closure was expected to occur only when Tom22 transiently interacted with the agarose hydrogel.

Figure 5.24B shows a fluorescence amplitude trace and trajectory of TOM-CC immobilized by Ni-NTA agarose below the DIB membrane. The amplitude trace shows two amplitude levels corresponding to the intermediate and low ion permeability states S_I and S_L of the TOM-CC. The trajectory shows that the position does not change over time, indicating that the TOM-CC is permanently immobilized. In contrast, the same experimental setup also revealed fluorescence amplitude traces with three amplitude levels (S_H, S_I and S_L) (Figure 5.24C). The corresponding trajectory showed that TOM-CC was moving in S_H but was temporarily trapped in S_I for 0.45 s, 0.63 s, and 3.41 s, respectively. Since the fluorescence signals of TOM-CC in S_L was too low, the TOM-CC in this state could not be tracked. Further results are shown in Figures 5.25 and 5.26. A total of $n = 137$ channels were analyzed. 83 were permanently trapped (Figure 5.25). 40 molecules were in motion or temporarily trapped (Figure 5.26). Remaining 14 molecules were in continuous motion. As expected, the diffusion coefficient of permanently immobilized TOM-CC was determined as $D(S_I)$ and $D(S_L) \leq D_{min} = 0.01$ μm^2 s^{-1} ($n = 83$). The diffusion coefficient of TOM-CC in moving state was $D(S_H) \simeq 0.34 \pm 0.06$ μm^2 s^{-1} (*mean ± SEM, n = 40*).
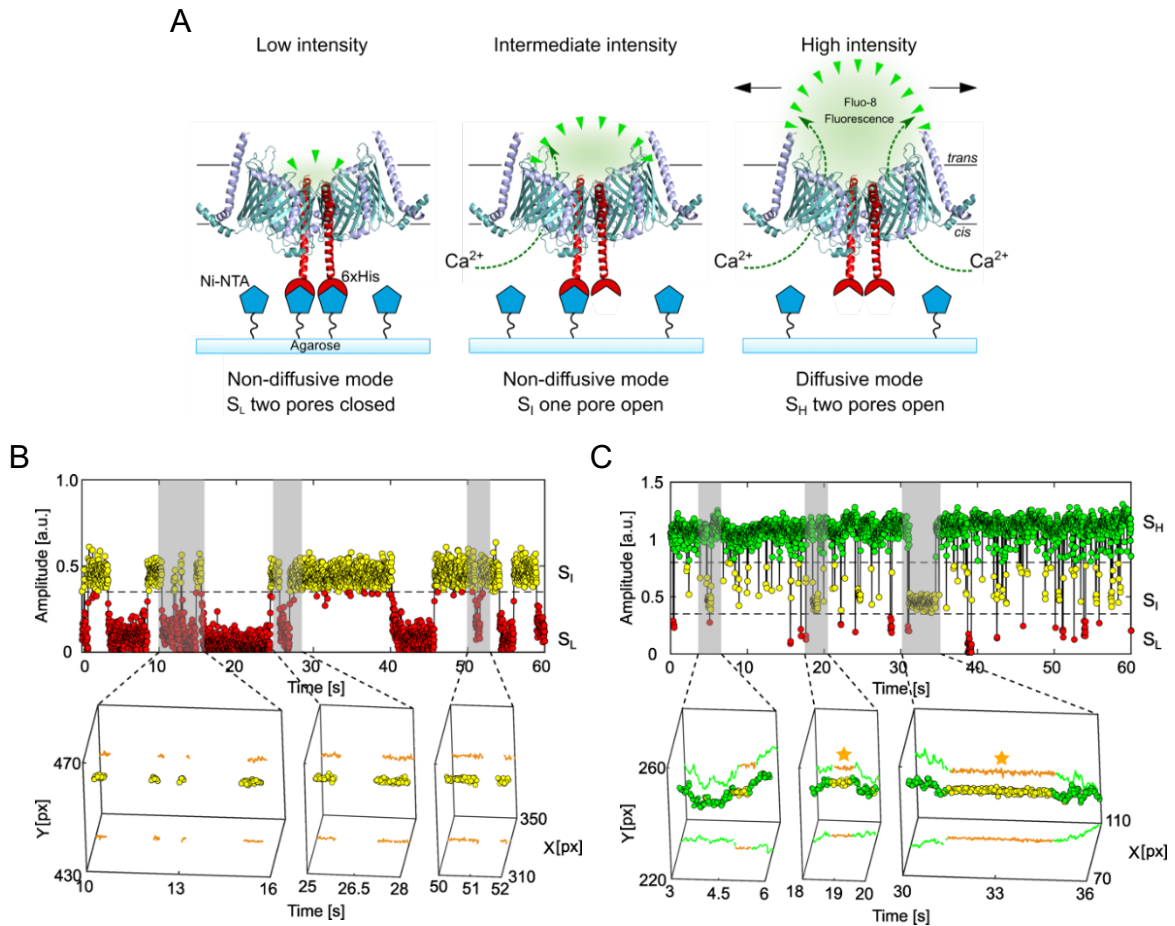
Figure 5.24: Controlled immobilization of TOM-CC causes channel closures. *A) Schematic representation of individual TOM-CC channels in DIB membranes supported by Ni-NTA-modified agarose. TOM-CC molecules can be permanently linked to the underlying hydrogel via His-tagged Tom22. Tethered and non-tethered TOM-CC molecules in closed (S_I and S_L) and open (S_H) states are indicated, respectively. This is due to the fact that Ca^{2+}-flux through the TOM-CC channel is blocked when the TOM-CC molecule is tethered to Ni-NTA agarose. B) Fluorescent amplitude trace (top) of a TOM-CC channel permanently tethered to Ni-NTA agarose. The trajectory segments (bottom) correspond to the time periods of the amplitude traces marked in grey. Non-diffusive, permanently immobilized TOM-CC is only found in S_I or S_L, indicating that tight binding of the His-tagged Tom22 domain (Figure 5.2A) to Ni-NTA agarose triggers closure of the β-barrel TOM-CC pores. C) Fluorescence amplitude trace (top) of a TOM-CC channel transiently and non-specifically entangled by Ni-NTA agarose. The trajectory segments (bottom) correspond to the time periods of the amplitude traces marked in grey. The movement of TOM-CC is interrupted twice at the same spatial x,y membrane position from $t_1 = 18.56$ s to $t_2 = 19.19$ s and from $t_3 = 31.14$ s to $t_4 = 34.55$ s (yellow stars). Consistent with the data shown in Figures 5.10 and 5.11, moving TOM-CC molecules in diffusive mode are found in the fully open S_H state; transient tethering causes the TOM-CC β-barrels to close. The color-coding is the same as in Figure 5.10. Frame rate, 47.5 s^{-1}; pixel size [px], 0.16 μm; a.u., arbitrary unit.*
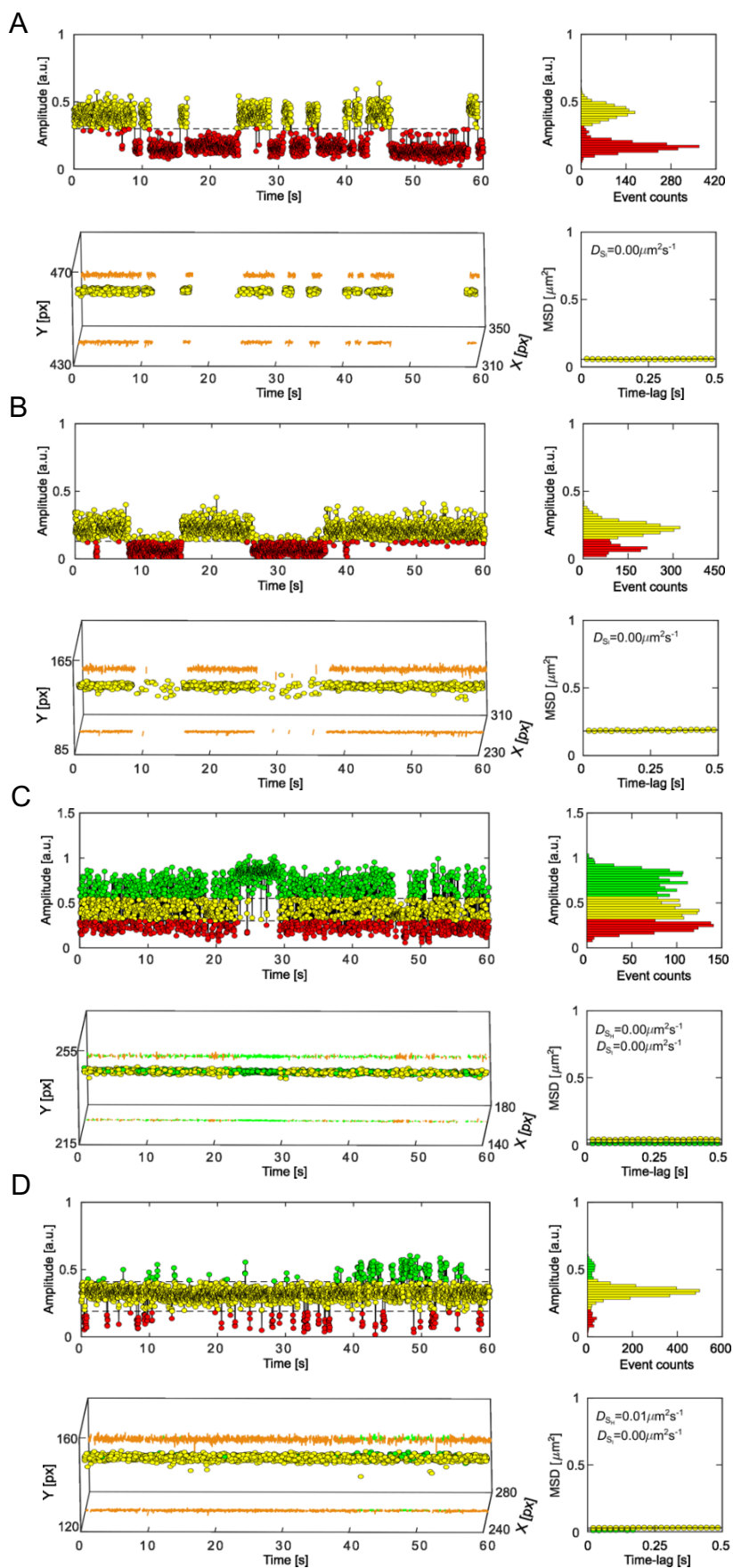
74

Figure 5.25: Controlled immobilization of His-tagged TOM-CC results in channel closures. *Representative fluorescent amplitude traces of individual TOM-CC channels (n = 83) recorded in DIB*

75

membranes. A, B, C and D) Particles are permanently trapped by Ni-NTA-modified agarose hydrogel below the DIB membrane. Fluorescent amplitude traces (upper left), amplitude histograms (upper right), trajectories (bottom left) and mean square displacement plots (MSD, bottom right) are similar to those shown in Figure 5.24B, respectively. In Figure 5.25C, the tethered TOM-CC showed frequent switching between three different permeation states (S_H, S_I and S_L). This may be due to Tom22 attempting to change conformation to maintain TOM-CC in a lower energy state. These trajectories demonstrated the same spatial x,y-position over time. Even though the TOM-CC molecules switched to S_L state and disappeared, they reappeared at the same spatial x,y-position. The mean square displacements (MSD) does not change with time for TOM-CC molecules. This is further indicating that TOM-CC molecules were permanently trapped. The color-coding is the same as in Figure 5.10. Frame rate, 47.5 s^{-1}; pixel size [px], 0.16 μm; a.u., arbitrary unit.

From these data, it can be concluded that most TOM-CC molecules (~ 60 %) could be permanently trapped by Ni-NTA-modified hydrogels under DIB membranes (Figure 5.25). As expected, most of the permanently trapped molecules were in the S_I or S_L state. This supported the hypothesis that the IMS domains of the two Tom22 receptors, located between the two Tom40 β-barrels, are involved in the mechanical regulation of the open and closed channel states of the TOM-CC. This hypothesis was further supported by the observation that TOM-CC molecules moved continuously in DIB membranes in the presence of imidazole which inhibited the permanent binding of 6xHis-Tom22 to Ni-NTA (Figure 5.27, $D(S_H) \simeq 1.35 \pm 0.14$ μm^2 s^{-1}, *mean ± SEM, n* = 30).

~ 30 % of molecules showed the same *stop-and-go* behavior (Figure 5.26) as those reconstituted into DIBs supported by unmodified agarose hydrogels (Figures 5.10 and 5.11). Another ~ 10 % of molecules were always moving and flickering (Figure 5.28) between S_H, S_I and S_L, which was not as expected as described above. This is likely due to TOM-CC having a non-functional Tom22 or reconstituted in DIB membranes with the IMS domain of Tom22 oriented toward the aqueous droplet side, which resulted in no interaction between TOM-CC and agarose hydrogel. Another unlikely explanation is that the correlation between open-closed channel activity and stop-and-go dynamics was not observed within these time windows.
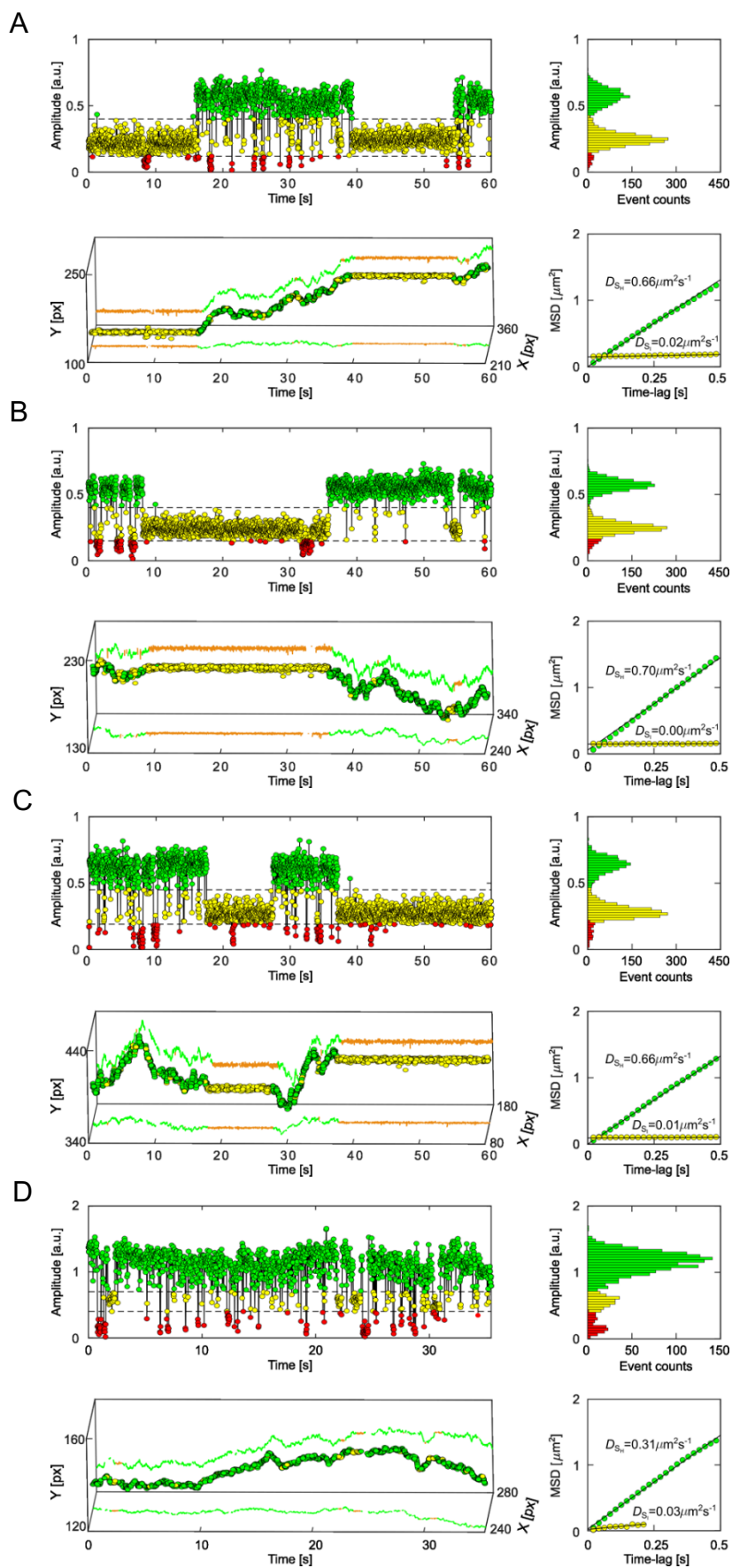
Figure 5.26: Lateral mobility and open-closed channel activity of transiently trapped TOM-CC molecules. *Representative fluorescent amplitude traces of individual TOM-CC channels (n = 40)*

recorded in DIB membranes supported by Ni-NTA agarose hydrogel. A, B, C and D) Particles are transiently trapped. Fluorescent amplitude traces (upper left), amplitude histograms (upper right), trajectories (bottom left) and mean square displacement plots (MSD, bottom right) are similar to those of TOM-CC molecules incorporated in unmodified agarose supported DIB membranes (Figures 5.10 and 5.11), respectively. The movement of TOM-CC molecules is occasionally interrupted by periods of transient anchorage. The moving TOM-CC molecules are found in the fully open S_H state (green); non-moving complexes in the inactive S_I (yellow) or S_L (red) states. The MSD is proportional to the time-lag when TOM-CC is in S_H state, but virtually constant in the S_I state. Frame rate, 47.5 s^{-1}; pixel size [px], 0.16 μm; a.u., arbitrary unit.
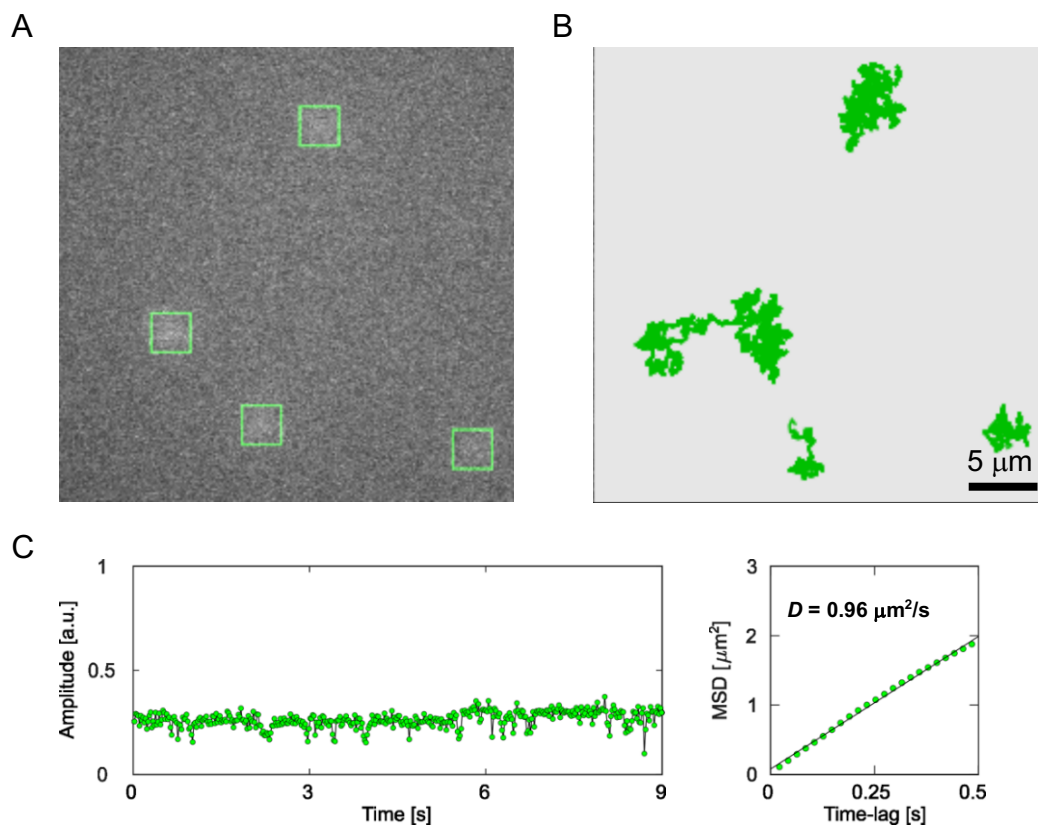
Figure 5.27: Lateral movement and channel activity of His-tagged TOM-CC molecules in DIB membranes supported by Ni-NTA agarose in the presence of imidazole. *A and B) Example TIRF image (left) and trajectories (right) of single TOM-CC molecules (n = 30). The green square marked TOM-CC molecules indicate identical fluorescent intensities. The trajectories undergo random walk, implying free diffusion. C) Fluorescence amplitude trace (left) of TOM-CC shows constant intensity, likely corresponding to conformational state S_H. The presence of imidazole prevents His-tagged TOM-CC from binding to Ni-NTA. The mean square displacement (MSD) increases linearly with time for TOM-CC. The low signal-to-noise ratio could be due to the blue color of the Ni-NTA hydrogel under the DIB membrane. Frame rate, 47.5 s^{-1}; a.u., arbitrary unit.*
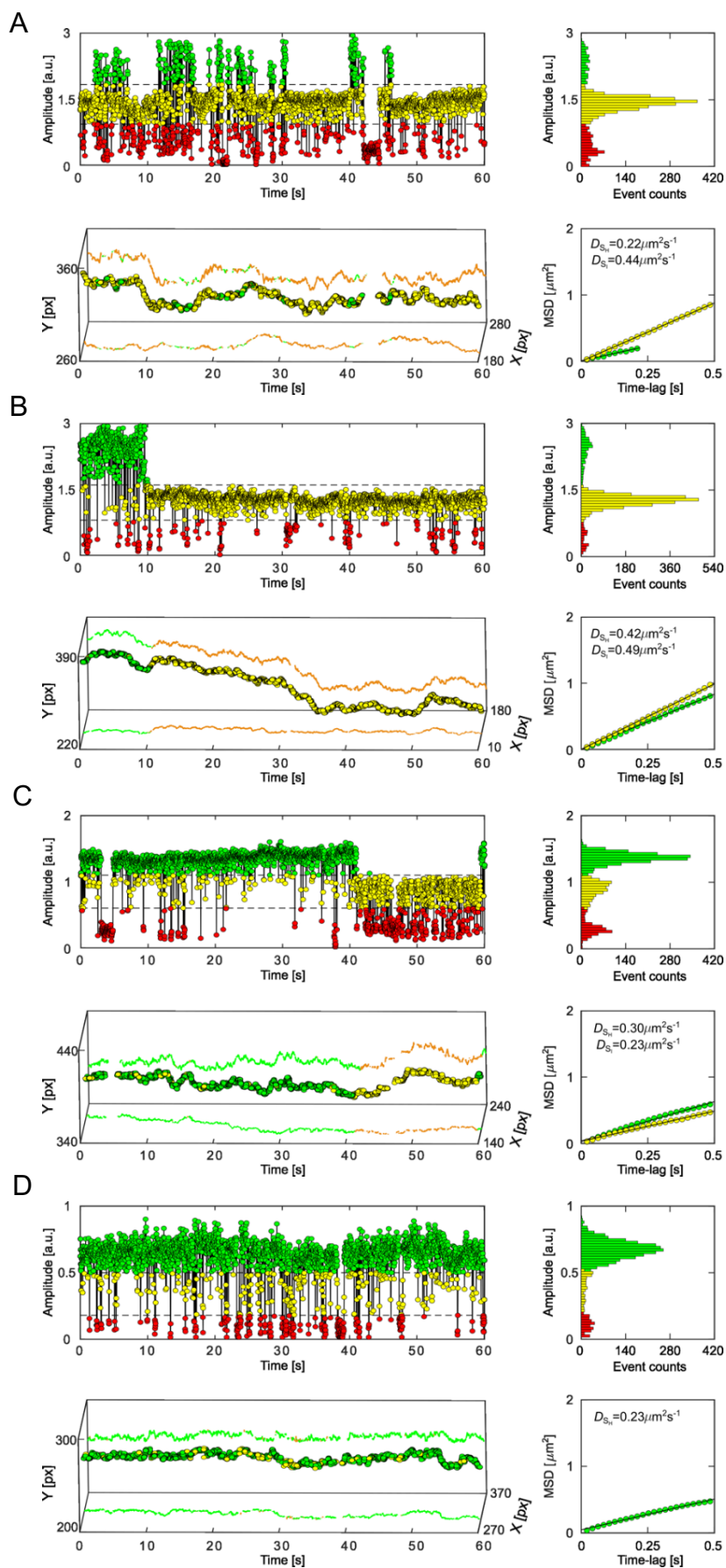
Figure 5.28: Lateral mobility and open-closed channel activity of atypical TOM-CC molecules in DIB membranes supported by Ni-NTA agarose hydrogel. *A, B, C and D) Fluorescent amplitude traces*

79

(upper left), amplitude histograms (upper right), trajectories (bottom left) and mean square displacement plots (MSD, bottom right) are shown. Particles (n = 14) are continuously moving and represent atypical TOM-CCs. These trajectories show that the spatial x,y-position are changing over time, indicating that TOM-CC molecules are freely moving in DIB membranes. The MSD increases linearly with time when TOM-CC is in S_H and S_I state. Color-coding, see Figure 5.10; frame rate, 47.5 s^{-1}; pixel size [px], 0.16 μm; a.u., arbitrary unit.

5.3.6 Statistical analysis of the correlation between lateral motion and TOM-CC channel activity

Based on the experimental results described for TOM-CC, Cy3-labeled TOM-CC, Tom40, OmpF, and αHL, it was intriguing to conclude that physical or chemical anchoring of the IMS domain of Tom22 results in immobilization of TOM-CC and consequent closure of its Tom40 channels. To further strengthen this conclusion, statistical data are provided in this section.
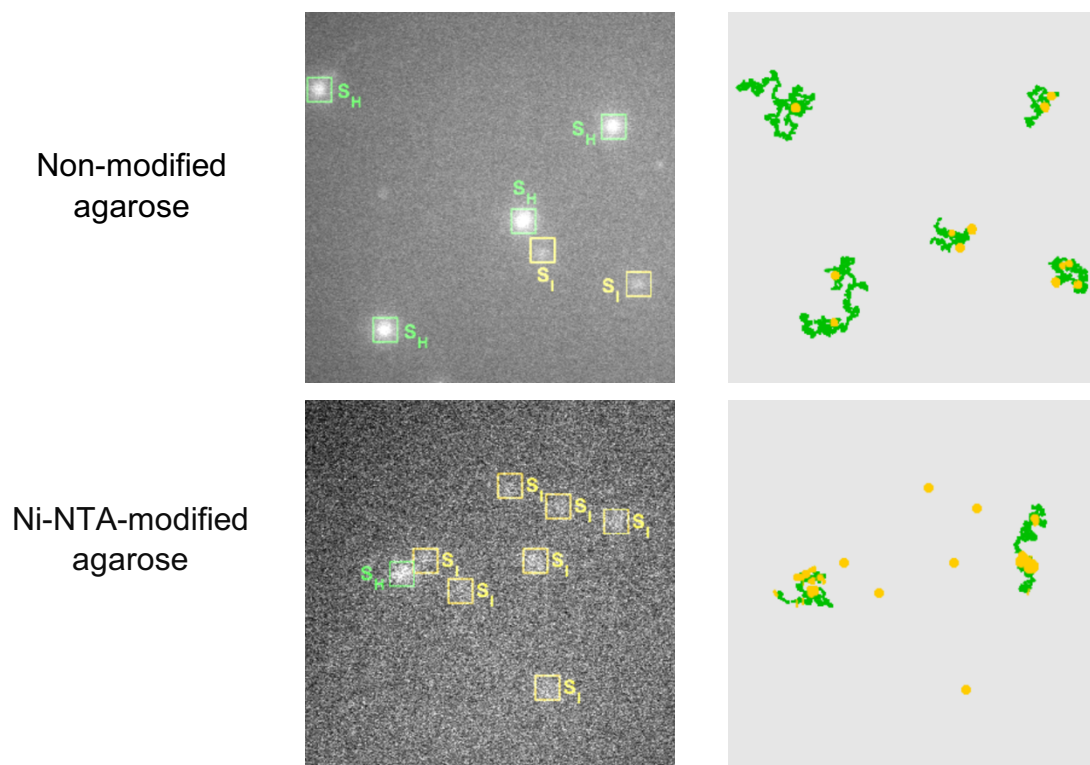
5.29: Comparison of transiently and permanently trapped TOM-CC molecules. TIRF images (left) and trajectories (right) of single His-tagged TOM-CC molecules in unmodified (top) and Ni-NTA-modified (bottom) agarose supported DIB membranes. The permanently tethered fraction of TOM-CC in Ni-NTA-modified agarose is significantly larger compared to the fraction in non-modified agarose over time. Individual spots are marked according to their conformational states; trajectories of trapped

TOM-CC molecules in S$_L$ are not shown. Original fluorescence intensities were recorded at a pixel size of 0.16 μm and at a frame rate of 47.51 s^{-1}.

DIB membranes (N_{DIB} > 50 x 10^6) supported by both hydrogels, unmodified and Ni-NTA-modified agarose, showed a significant number of non-diffusive TOM-CC molecules at S$_I$ and diffusive TOM-CCs at S$_H$ (representative example in Figures 5.11 and 5.26). Thus, 187 TOM-CC molecules were numerically sorted into diffusive $D > D_{min}$ = 0.01 μm^{2}s^{-1} and non-diffusive $D \leq D_{min}$ tethered groups. I then asked whether the molecules were in the fully opened S$_H$ or half-open S$_I$ state. Since weak intensity profiles did not allow accurate determination of the position of TOM-CC and thus the lateral diffusion coefficient D(S$_L$), I conducted classification analysis using only the parameters $D(S_H)$ and $D(S_I)$.

As shown in Figure 5.30 and Figure 5.31A, three main classes of lateral motion and channel activity could be defined:

i.   Transient anchorage: the first and major class I $\{I|D(S_H) > D_{min} \cap D(S_I) \leq D_{min}\}$ shows lateral mobility at S$_H$ only, while being tethered at S$_I$. Here, spatiotemporal *stop-and-go* dynamics of the TOM-CC correlate with channel activity (Figures 5.10, 5.11 and 5.26).

ii. Free diffusion: the second class II $\{II|D(S_H) > D_{min} \cap D(S_I) > D_{min}\}$ shows similar diffusivities at both states, S$_H$ and S$_I$ (Figure 5.28). The TOM molecules in this class are unlikely to have a functional Tom22 (Ahting et al., 2001; Shiota et al., 2015) or are incorporated into the membrane in a reverse orientation and therefore do not interact with the hydrogel. Another possible but unlikely explanation is a spatial void of agarose network preventing mechanoregulated interaction of Tom22 with the network within the observation time window.

iii. Permanent anchorage: the third class III $\{III|D(S_H) \leq D_{min} \cap D(S_I) \leq D_{min}\}$ represents events exhibiting permanently tethered TOM-CC molecules, which do not move in the membrane and are exclusively non-diffusive (Figure 5.25). Most molecules in this class are in S$_I$ and S$_L$. Those TOM-CC molecules, which briefly change from S$_I$ to S$_H$ and back to S$_I$ (Figures 5.25C - D), could diffuse in S$_H$ but are immediately recaptured and trapped by the hydrogel below the membrane, resulting in $D(S_H) \leq D_{min}$.
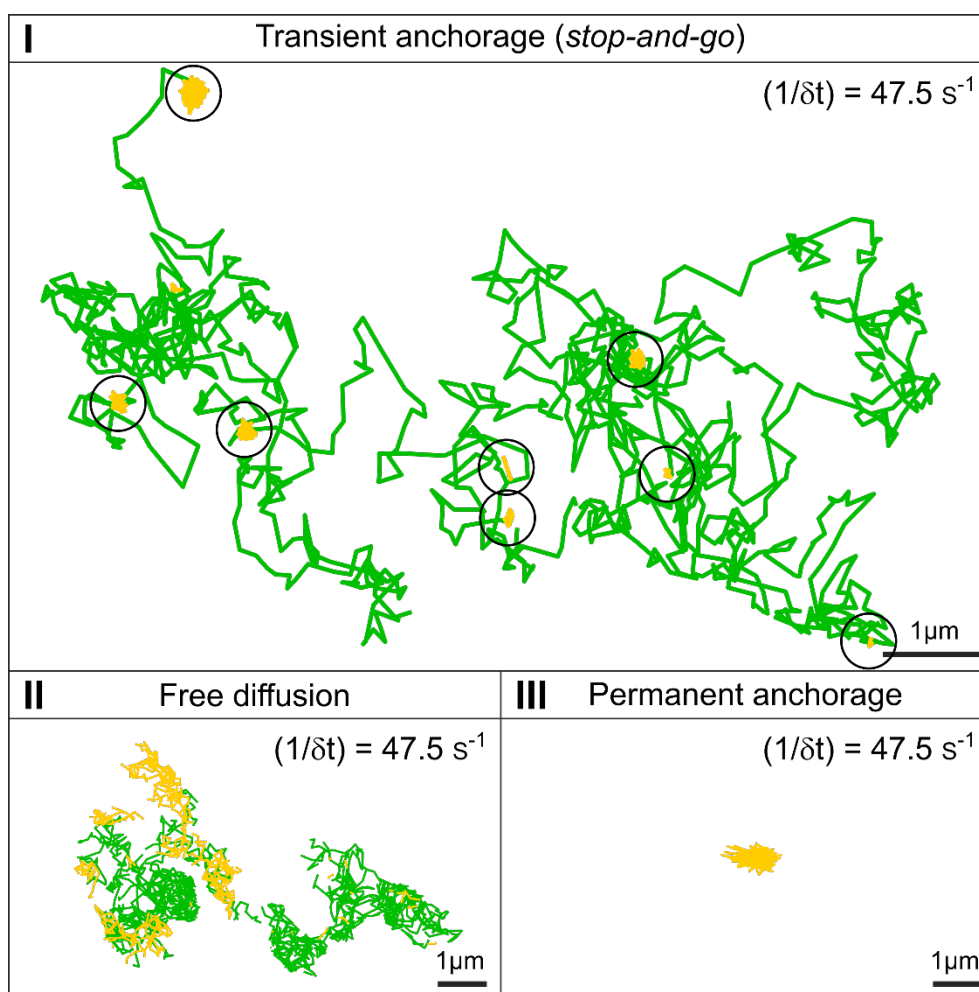
Figure 5.30: Trajectories for the main TOM-CC mobility modes. *Class I $\{I|D(S_H) > D_{min} \cap D(S_I) \leq D_{min}\}$, diffusion interrupted by periods of transient anchorage (sites of transient anchorage circled); Class II $\{II|D(S_H) > D_{min} \cap D(S_I) > D_{min}\}$, free diffusion; Class III $\{III|D(S_H) \leq D_{min} \cap D(S_I) \leq D_{min}\}$, permanent anchorage. Moving particles in S_H are shown in the trajectories in green; transiently or permanently tethered molecules in S_I are shown in yellow. Data were acquired for t = 60s. $D_{min} = 0.01 \mu m^2 s^{-1}$.*

Figure 5.31B shows state probabilities of TOM-CC in membranes supported by the two different hydrogels, non-modified and Ni-NTA-modified agarose. Diffusive molecules ($D > D_{min}$) in membranes supported both by non-modified and Ni-NTA-modified agarose show similar probabilities to be at one of the three permeability states (S_H, S_I and S_L). Diffusive TOM-CC molecules are significantly more often at S_H than at S_I and S_L. The permanently tethered fraction of TOM-CC (67 %) in Ni-NTA-modified agarose is ~2.4 times larger compared to the fraction (28 %) in non-modified agarose, consistent with the stronger interaction of Tom22 with the hydrogel, thereby permanently constraining lateral motion. In line with this, permanently tethered molecules ($D \leq D_{min}$) in both hydrogel-supported membranes stay at S_I during the

majority of time, and show only transient S_H and S_L occupancy. These statistics support the hypothesis that the C-terminal IMS domain of Tom22 plays a previously unrecognized role in mechanoregulation of TOM-CC channel activity by binding to immobile structures near the membrane.
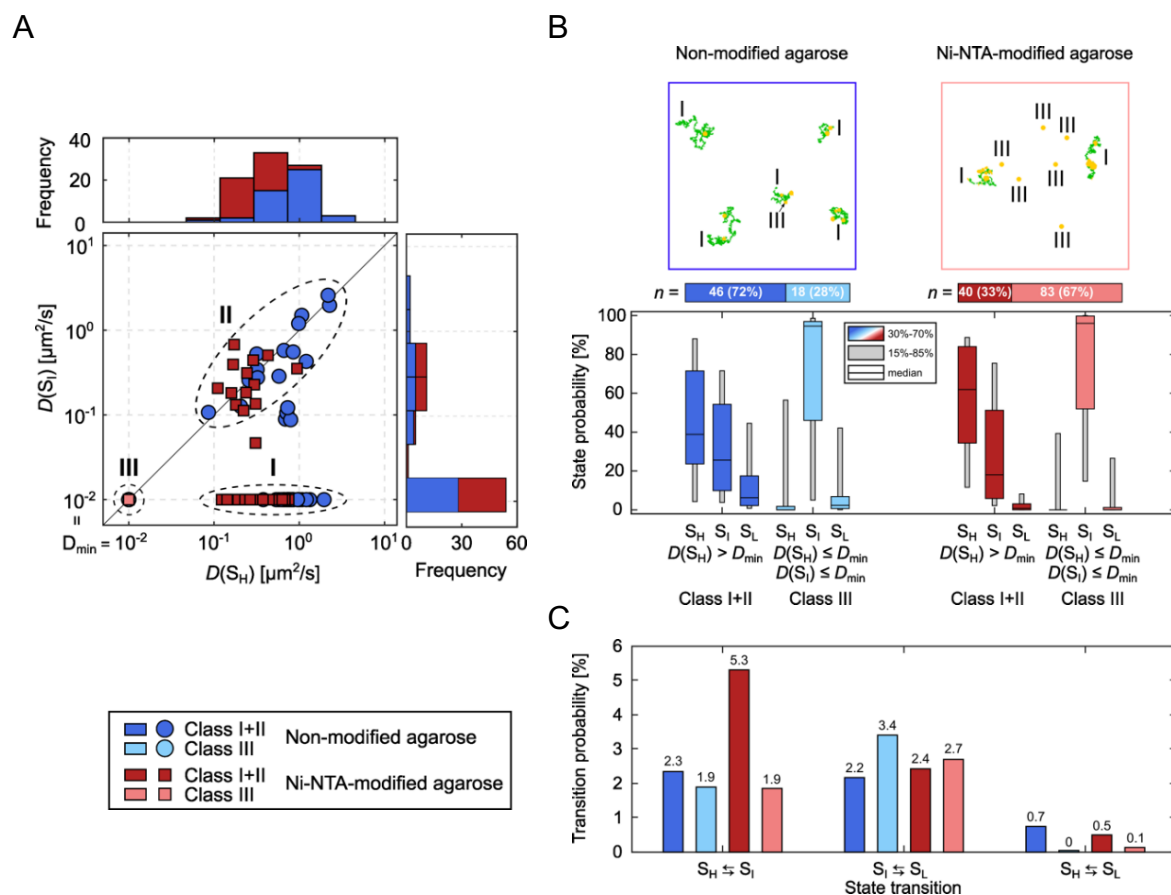
Figure 5.31: Statistics of correlation between channel activity and lateral mobility of TOM-CC. *A) $D(S_I)$ as a function of $D(S_H)$ individually plotted for all TOM-CC molecules in DIB membranes supported by unmodified (dark blue and light blue, n = 64) and Ni-NTA modified agarose (dark red and light red, n = 137). Frequency histograms of $D(S_H)$ and $D(S_I)$ are shown on top and right side, respectively. Three classes can be defined: a main class (I) of moving particles in S_H while being transiently tethered at S_I $\{I|D(S_H) > D_{min} \cap D(S_I) \leq D_{min}\}$, a second class (II) of freely moving particles in S_H and S_I $\{II|D(S_H) > D_{min} \cap D(S_I) > D_{min}\}$ and a third class (III) of permanently tethered molecules in S_I and S_L $\{III|D(S_H) \leq D_{min} \cap D(S_I) \leq D_{min}\}$. B) Example trajectories (top) and state probabilities (bottom) of non-permanently and permanently tethered TOM-CC in DIBs supported by non-modified and Ni-NTA-modified agarose. The probability of being in state S_H is higher for non-permanently (classes I and II, dark blue [n = 46] and dark red [n = 40]) than for permanently tethered molecules (class III, light blue [n = 18] and light red [n = 83]). The probability of being in state S_I is significantly higher for permanently (class III) than for non-permanently tethered particles (classes I*

and II). The data are represented as median; the confidence intervals are given between 15 % to 85 % and 30 % to 70 %. C) Absolute state transition probabilities classified by bidirectional state transitions as $S_H \leftrightarrows S_I$, $S_I \leftrightarrows S_L$, and $S_H \leftrightarrows S_L$. Diffusive TOM-CC molecules have a significantly higher transition probability for switching between S_H and S_I in DIBs supported by Ni-NTA-modified agarose (~5.3 %) than in non-modified agarose membranes (~2.3 %). This is consistent with the higher efficacy of TOM-CC-trapping by Ni-NTA-modified agarose compared to non-modified agarose. Classification of non-permanently and permanently tethered TOM-CC is shown at the left bottom.

Although diffusive TOM-CC molecules ($D > D_{min}$) are observed more often at S_H in Ni-NTA-modified agarose than in non-modified agarose supported membranes (Figure 5.31B), they show a lower stability at S_H having a significantly higher transition probability for switching between S_H and S_I (Figure 5.31C, ($S_H \leftrightarrows S_I$) $\simeq$ 5.3 % versus ($S_H \leftrightarrows S_I$) $\simeq$ 2.3 %). This is in line with the higher efficacy of TOM-CC-trapping by Ni-NTA-modified agarose compared to non-modified agarose. In contrast to unmodified hydrogel, Ni-NTA-modified agarose hydrogel can capture freely mobile TOM-CC via the IMS domain of Tom22 in two ways: on the one hand, by specific interaction and permanent anchoring with Ni-NTA, and, on the other hand, by collision and transient nonspecific anchoring. While a direct transition between S_H and S_L barely occurs in both systems, transitions between S_I and S_L are similarly often. This indicates that the two Tom40 β-barrel pores independently open and close within the time resolution (~20 ms) of our experiment. Only very few experiments ($n = 10$) showed fluorescence dots flickering between four intensity levels and thus permeability states (Figure 5.32). Whether these data correspond to trimeric TOM-CC with three Tom40 -barrel spores, as sometimes observed in yeast (Araiso et al., 2021), could not be conclusively determined.
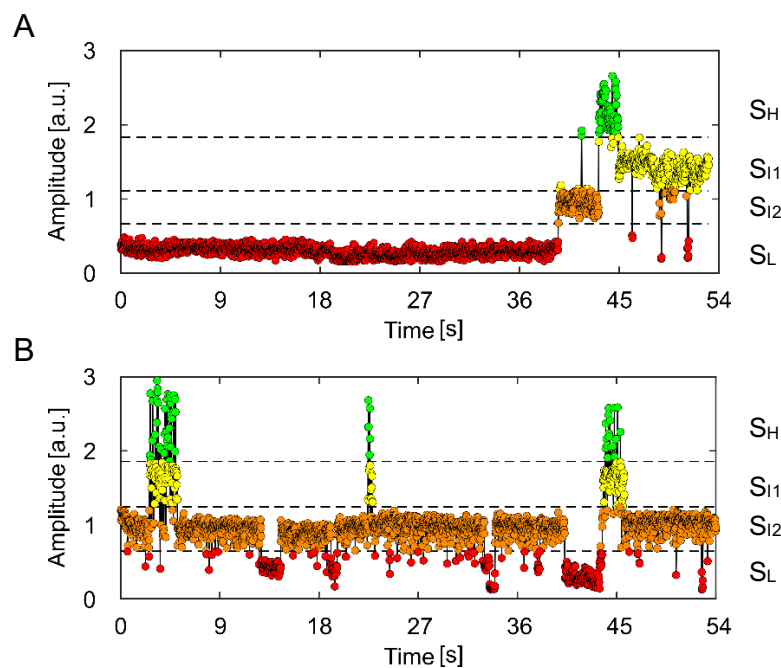
Figure 5.32: Lateral mobility and open-closed channel activity of rare TOM-CC molecules. *A) and B) Fluorescence amplitude traces of two exemplary TOM-CC channels (n = 10) with four permeation states recorded in DIB membranes. They show four different amplitude levels (S_H, S_{I1}, S_{I2}, S_L) corresponding to four different states of ion permeation. According to previous structural work based on chemical cross-linking (Araiso et al., 2021), the four permeability states would correspond to a TOM core complex containing three Tom40 pores. Green, three pores are fully open; yellow, two pores are fully open; orange, one pore is fully open; red, three pores are fully closed. Frame rate, 47.5 s^{-1}; a.u., arbitrary unit.*

6 Discussion

TOM-CC is the main entry portal for mitochondrial preproteins and small molecules crossing the outer mitochondrial membrane. Inward transport into the mitochondrial matrix and inner mitochondrial membrane is regulated by interactions with other mitochondrial protein translocation machineries (e.g., TIM23 and TIM22) and posttranslational modifications (Rapaport et al., 1998; Schmidt et al., 2011).

In this work, 211 individual TOM-CC molecules, 15 Cy3-labeled TOM-CC molecules, 20 Tom40 molecules, 171 OmpF molecules, and 30 α-hemolysin molecules were analyzed in DIB membranes in terms of lateral movement and channel activity, corresponding to approximately 1.27 million images. This sample number allowed the activity and mobility of these channels to be assigned with statistical confidence using nonparametric statistics. Even a visual review of the data was sufficient to provide an initial assessment of the reliability of the data. Moreover, this work shows that immobilization affects the channel activity of TOM-CC. Therefore, TOM-CC could be inherently mechanosensitive, with Tom22 acting as a "mechanosensitive switch" for opening and closing the channels.

6.1 Impact of Tom22 on the TOM-CC channel activity

The data collected for TOM-CC are consistent with the dimeric pore structure of TOM-CC, where three channel activity states correspond to one or two open or all closed pores, respectively. They show that the TOM-CC molecules can switch reversibly between the following ion permeation states: both channels are open (high permeable state, S_H), one channel is open (intermediate permeable state, S_I) and both channels are closed (low permeable state, S_L). Although the temporal resolution of the optical approach described in this work is much lower than in electrophysiological experiments (Kasianowicz et al., 1996; Sondermann et al., 2006; Ouldali et al., 2020), the temporal resolution of the optical system was sufficiently high to analyze the most important channel properties of TOM-CC. From a technical point of view, however, sampling rates up to 10 kHz would also be possible if fluorescence photons are counted by an avalanche photodiode (Schmidt et al., 2021).

In this section, I first discuss whether gating of TOM-CC between three permeability states is consistent with previous electrophysiological data for TOM-CC in free-standing lipid bilayers (Muro et al., 2003; Becker et al., 2005; Poynor et al., 2008). Then, the structure and function of the main subunits Tom40 and Tom22 are discussed to clarify which of them triggers channel gating.

Previous electrophysiological experiments have shown that both channels of *N. crassa* TOM-CC are fully open at low membrane potential |V| < 20 mV (Poynor et al., 2008). At higher voltage, TOM-CC switched to low conductance levels, indicating closure of its pores (Poynor et al., 2008). The predominant conductance states were a main open state S5, an intermediate state S3 and a low state S2 (Poynor et al., 2008). The S2 state (~0.36 nS in 1 M KCl, (Poynor et al., 2008) might correspond to the low permeability state S_L described in this work. The intermediate permeability state S_I could correspond to S3 (~0.67 nS in 1 M KCl, (Poynor et al., 2008). Finally, the fully open state S_H could correspond to S5 (~2.10 nS in 1 M KCl, (Poynor et al., 2008). Alternatively, S_H, S_I and S_L could also correspond to conductance state S5, S4 (~1.09 nS in 1 M KCl, (Poynor et al., 2008) and S1 (~ 0.16 nS in 1 M KCl, Poynor et al., 2008). However, since states S4 and S1 were not occupied by TOM-CC with high probability, the first hypothesis seems more likely. Final insights can only be obtained by simultaneous optical and electrophysiological recordings with single channels in a DIB membrane.

The two Tom40 subunits within TOM-CC (Figure 5.2A) are formed by two β-barrels. Both are composed of 19 β-strands each, similar to mitochondrial VDAC (Bayrhuber et al., 2008; Ujwal et al., 2008). A short α-helical segment (N-terminus) stabilizes the β-barrel pore (Naveed et al., 2009; Gessmann et al., 2011a) by interacting with β-strands 13 and 14 (Figure 6.1A) (Bausewein et al., 2017; Ornelas et al., 2023). A similar β-barrel stabilizing α-helical segment is also found in the pore of VDAC (Geula et al., 2012).

VDAC is known to undergo major conformational changes during voltage-dependent gating (Zimmerberg and Parsegian, 1986; Colombini et al., 1996; Song et al., 1998). Many studies have attributed these changes to movements of its N-terminal α-helical segment inside the pore (Guo et al., 1995; Mannella, 1998; De Pinto et al., 2008; Ujwal et al., 2008; for review, see Hiller and Wagner, 2009; Shoshan-Barmatz et al., 2010). This, however has been questioned recently. Although various stimuli such as voltage, pH and protein-protein interactions were thought to disrupt its interactions with the β-barrel wall (Ujwal et al., 2008), the VADC structure

showed that the N-terminal segment has extensive hydrophobic interactions and forms hydrogen bonds with the interior wall of the pore (adjacent to β-strands 8-19), facilitating its orientation (Ujwal et al., 2008; Teijido et al., 2012). In order to further tether the α-helical segment to the pore wall (Figure 6.1B), the cysteines at position 10 (Leu10Cys) and at position 170 (Ala170Cys) were introduced and then these two positions were cross-linked by the formation of a disulfide bond (Teijido et al., 2012). The Leu10Cys /Ala170Cys mutant protein showed the characteristic VDAC voltage gating where the wild type transitioned between open and multiple closed states (Teijido et al., 2012). This indicates that the α-helical segment does not move independently during channel gating. Given the structural similarity between VDAC and Tom40, it is therefore unlikely that the gating of TOM-CC can be explained by rearrangements of the N-terminal helix within the Tom40 pore. However, definitive proof must be obtained in the future, as in the case of VDAC by a combination of site-directed cross-linking and electrophysiology.
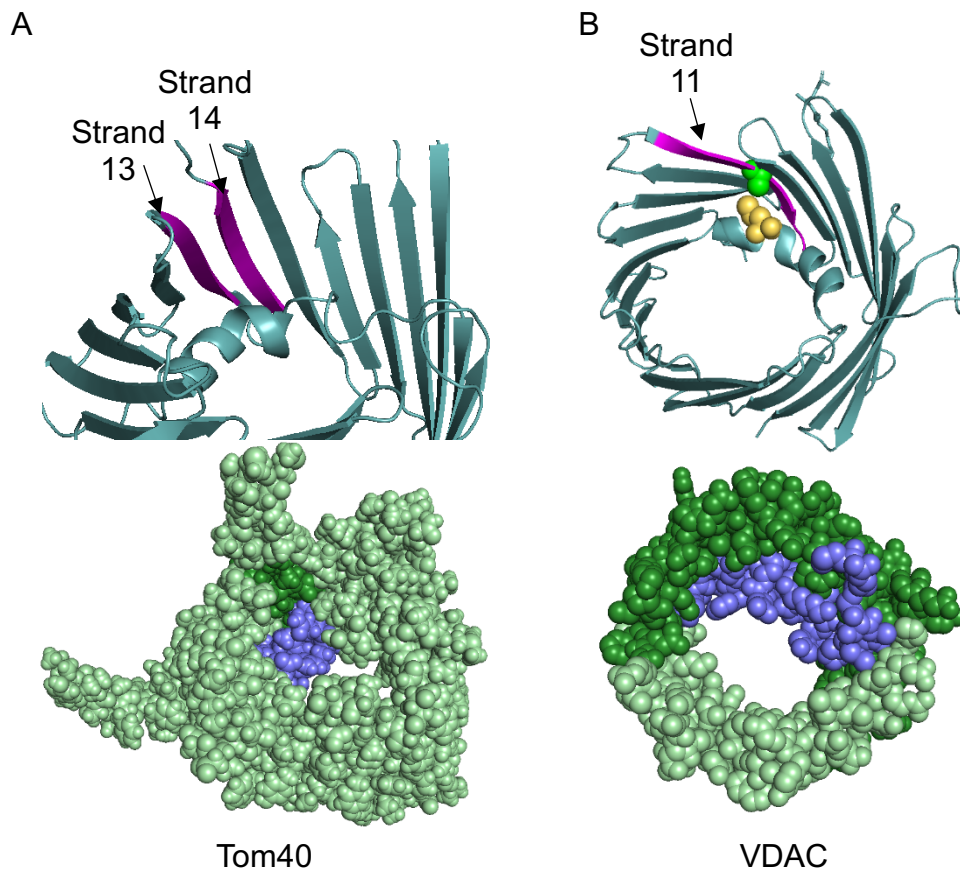

Figure 6.1: Schematic representation of Tom40 and VDAC pore. *A) The α-helical segment of Tom40 (EMDB, EMD-3761; top and bottom: blue; (Bausewein et al., 2017, 2020)) closely interacting with β-barrel strands 13 and 14 (top: magenta; bottom: dark green) is displayed. B) VDAC (PDB 3EMN; (Ujwal et al., 2008)) displaying interaction of its internal α-helical segment (blue) with β-strand 8-19*

(dark green). The cross-linking positions of amino acid residues Leu-10 and Ala-170 are displayed in yellow and green.

A previous comparison of the channel properties of wild-type and mutant TOM in *S. cerevisiae* revealed that the wild-type TOM channel is mainly in a closed state, whereas the mutant without Tom22 is mainly in an open state (van Wilpe et al., 1999). As observed for the mutant TOM in absence of Tom22, this work also found by optical means that ion flux through individual Tom40 channels was constant over time, implying that their pores were always open. This suggested that Tom22 is involved in channel gating of Tom40.

6.2 Impact of Tom22 on the TOM-CC lateral movement

Membrane protein movement can be restricted by nanoscopic domains in the membranes (Jacobson et al., 2007, 2019; for review, see Sezgin et al., 2017) and by peripheral structures of the intracellular and/or extracellular environment (for review, see Nicolson, 2014). The diffusion coefficients of these proteins are typically ten to hundred-fold lower than those of freely diffusing proteins (Sanderson, 2012).

The nanoscopic domains in membranes are typically formed by short-range transient ordering of lipids in the presence of a high concentration of membrane proteins (Jacobson et al., 2007). They are important, for example, for the immune recognition of specific polysaccharides on pathogens by the nanoclusters of lectin receptors (for review, see Dustin and Choudhuri, 2016).

Typical examples of proteins that are temporarily trapped in membranes by anchoring to peripheral structures are the integrins (Alberts et al., 2002). They connect the cytoskeleton inside the cell with the extracellular matrix. Transferrin receptors in the membrane are typically interacting with the actin filament skeleton 'fence' inside the cell (Sheetz, 1983; for review, see Kusumi et al., 2010; for review, see Jaqaman and Grinstein, 2012). Alternatively, transmembrane proteins can be fenced by protein 'pickets' anchored to the actin skeleton (Haggie et al., 2006; Morone et al., 2006; for review, see Kusumi et al., 2010; for review, see Jaqaman and Grinstein, 2012) (Figure 6.2).

In previous single-molecule tracking experiments, the lateral movement of mitochondrial outer and inner membrane proteins was studied (Sukhorukov et al., 2010; Kuzmenko et al., 2011;

Appelhans et al., 2012; for review, see Appelhans and Busch, 2017). Fluorescently labelled TOM subunits, such as Tom7, Tom20 and Tom40 fused with GFP and Halo/TMR, indicated freely moving and immobilized TOM populations. The lateral diffusion constants of mobile and immobile proteins ranged from 0.005 $\mu m^2 s^{-1}$ to 0.6 $\mu m^2 s^{-1}$ in mammalian mitochondria depending on the method of determination (FRAP and STP, Table 6.1) (Sukhorukov et al., 2010; Kuzmenko et al., 2011; Appelhans et al., 2012; for review, see Appelhans and Busch, 2017).
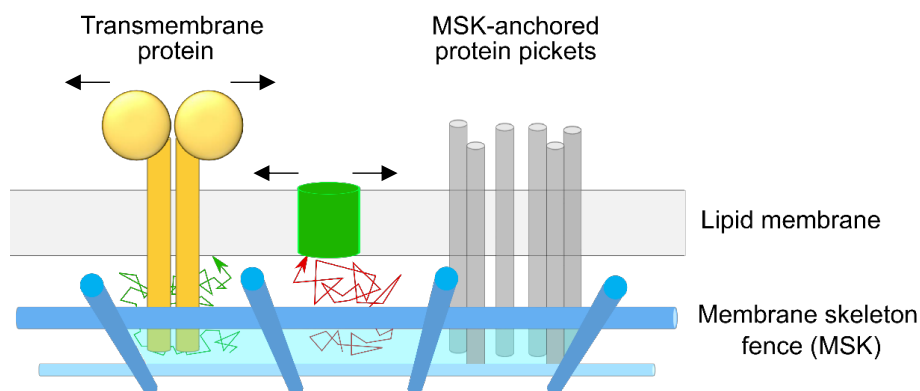
Figure 6.2: Fence-and-pickets model regulating transmembrane protein movement. *The lipid membrane (grey) of an eukaryotic cell can be separated into different compartments (cyan bar) by the membrane skeleton (MSK, blue) or picket proteins (dark grey) anchored to the MSK. Transmembrane proteins (TM) (yellow), which protrude from the lipid membrane, undergo confined diffusion (green and red trajectories) when they interact with pickets-proteisn or MSK. TM proteins entirely embedded in the membrane (green) are subject to confined diffusion only when they interact with the pickets.*

Table 6.1: Diffusion coefficients of mitochondrial proteins

		FRAP ($\mu m^2 s^{-1}$)	STP ($\mu m^2 s^{-1}$)	Reference
Tom7-GFP	mt membrane	0.6 ± 0.4	0.13 ± 0.025	(Sukhorukov et al., 2010; Appelhans and Busch, 2017)
Tom20-Halo/TMR	mt membrane	-	0.14 ± 0.014 [1] 0.005 ± 5E-4 [2]	(Appelhans et al., 2012)
Tom40-GFP	mt membrane	-	0.49	(Kuzmenko et al., 2011)
Tom40	DIB membrane	-	1.49 ± 0.16 [1]	this work
TOM-CC	DIB membrane	-	0.83 ± 0.16 [1] 0.01 [2]	this work

[1] mobile, [2] immobile

In this work, the diffusion coefficients of mobile TOM-CC and Tom40 in DIBs are higher than those of TOM subunits Tom7, Tom20 and Tom40 determined in native mitochondrial membranes (Table 6.1). There are several factors that can explain this difference:

i. Fluorescent GFP or Halo/TMR fused to Tom7, Tom20, or Tom40 decrease lateral diffusion in native mitochondrial membranes by increasing molecular mass and lateral friction in the membrane. In this work, the lateral diffusion of TOM molecules in DIB membranes was directly investigated by monitoring the Ca^{2+}-Fluo-8 fluorescence cloud in the vicinity of the TOM-CC channel without the need for fluorescent labeling.

ii. The lipid composition of native mitochondrial outer membranes (Table 6.2) is different from that of DIB membranes used in this work. The membranes were formed by fully saturated 16:0 DPhPC. The major lipids in mitochondrial outer membranes are phosphatidylcholine (PC), phosphatidylethanolamine (PE), phosphatidylinositol (PI), phosphatidylserine (PS), and phosphatidic acid (PA) (for review, see Horvath and Daum, 2013). PC and PE account for ~50 and 30% of total lipids, respectively, making them the most abundant lipid species (Daum and Vance, 1997; for review, see Horvath and Daum, 2013). About 40 % of their fatty acids are unsaturated (Table 6.3). These fatty acids (Table 6.3) in native outer mitochondrial membranes do not pack as tightly as 16:0 DPhPC in DIB membranes (Gennis, 1989). This reduces membrane viscosity (Seu et al., 2006; Hac-Wydro and Wydro, 2007), which in turn would lead to higher lateral protein mobility and diffusion coefficients according to Saffman-Delbrück theory (eq. (18)) (Saffman and Delbrück, 1975; Saffman, 1976; Ramadurai et al., 2010). However, the presence of longer fatty acid chains in native outer mitochondrial membranes (Table 6.3) can decrease the lateral mobility of proteins (Seu et al., 2006; Ramadurai et al., 2010) in a two-dimensional fluid according to:

$$D = \frac{k_B T}{4\pi\eta h}\left(\ln\left(\frac{\eta h}{\eta' R}\right) - \gamma\right) \tag{18}$$

where k_B is the Boltzmann constant, T is absolute temperature, h is the thickness of the bilayer, η is viscosity of the membrane, η' is viscosity of the outer liquid, R is the radius of the diffusing object, and γ is Euler's constant. In this model, D is logarithmically dependent on the radius of the diffusing object and inversely proportional to the thickness of the bilayer and viscosity of the lipid membrane. The eq. (18) was used to estimate the diffusion coefficients obtained by using the DIB optical setup. Here, the $k_B T = 4.11$ x 10^{-14} ergs, $\eta \approx$ 1.45 poise, $\eta' \approx 0.01$ poise, $h \approx 5$ x 10^{-7} cm (Saffman and Delbrück, 1975), $R_{\text{TOM-CC}} \approx 6.5$ x 10^{-7} cm (Bausewein et al., 2017) and $\gamma \approx 0.58$ were substituted into the eq. (18) at 25 °C.

The theoretical diffusion coefficient of 1.8 $\mu m^2 s^{-1}$ is in full agreement with those measured in this work (Table 6.1).

Table 6.2: Lipid composition of the outer mitochondrial membrane in weight percent

	Mammalian cells[1] (Rat liver)	Yeast[2] (*Saccharomyces cerevisiae*)
Phosphatidylcholine (PC)	54	46
Phosphatidylethanolamine (PE)	29	33
Phosphatidylinositol (PI)	13	10
Phosphatidylserine (PS)	2	1
Cardiolipin (CL)	<1	6
Phosphatidic acid (PA)	1	4

[1] Data are from (Daum and Vance, 1997), [2] data are from (Zinser et al., 1991)

Table 6.3: Fatty acid compositions of the outer mitochondrial membrane from the rat liver in weight percent.

	14:0	15:0	16:0	16:1	17:0	18:0	20:3	22:4	22:6
Outer mitochondrial membrane	0.4	27.0	4.1	21.0	13.5	13.5	1.1	15.7	3.5

Data are from (Gennis, 1989)

Table 6.4: Lipid composition of the outer mitochondrial membrane in weight percent

	Mammalian cells[1] (Rat liver)	Yeast[2] (*Saccharomyces cerevisiae*)
Phospholipid (mg/mg protein)	0.45	0.91
Sterols (mg/mg protein)	0.04	<0.01

Data are from (Daum and Vance, 1997)

iii. The protein density of TOM-CC in the DIB membranes of this work was lower than 100 molecules per μm^2, whereas in native outer mitochondrial membranes, typical protein densities are as high as $\sim 10^6$ per μm^2 (Table 6.4) resulting in anomalous subdiffusion as described by the power law:

$$\langle r^2(\tau) \rangle = D_\alpha \tau^\alpha \qquad (19)$$

where $\langle r^2(\tau) \rangle$ is the mean square displacement of protein complex, D_α is the generalized diffusion coefficient, τ is the elapsed time and $\alpha < 1$. At protein densities of less than 100 molecules per μm^2, the effect of protein displacement is small and subdiffusion could be ignored (Ramadurai et al., 2009) in the measurements of protein mobilities in this work. Therefore, the data describing protein diffusion in DIB membranes are in complete

agreement with the theory and experimental data recorded for TOM in native outer mitochondrial membranes.

From a molecular perspective, the different diffusion properties (mobile vs. immobile) could be due to different interactions of TOM with the inner mitochondrial membrane. It can be assumed that the specific interaction with the inner mitochondrial TIM23 translocase ($D_{Tim23-Halo/TMR} \simeq 0.04 \ \mu m^2 s^{-1}$) (Appelhans et al., 2012; for review, see Appelhans and Busch, 2017) leads to the immobilization of TOM in the outer membrane during protein import. Since purified Tom40 diffuses freely in DIBs at any time (Figure 5.16), unlike TOM-CC, it can be readily concluded that Tom22 is responsible for anchoring the complex to the agarose network under the DIB membranes. At the molecular level, the C-terminal IMS domain of Tom22 is likely to be responsible for this, as confirmed by direct anchoring of TOM using His-modified Tom22 and Ni-NTA-modified hydrogels (Figure 5.25). Accordingly, for sufficiently long observation times, TOM-CC thus clearly obeyed the law (for review, see Jacobson et al. 2019) of restricted and confined diffusion (Figure 5.12).

6.3 Role of Tom22 in linking lateral movement and channel activity of TOM-CC

To date, the question of how the function of a membrane protein is influenced by its local molecular environment and thus by its actual position in the membrane is often unresolved (for review, see Jacobson et al., 2019). It is even more complex to answer the question of how the lateral movement of a protein affects its function (for review, see Jacobson et al., 2019).
In this work, it was possible to decipher the relationship between lateral movement and channel activity of TOM-CC in DIBs supported by an artificial hydrogel skeleton: it was shown that freely moving TOM-CCs were in a state of high ion permeation, while transiently or permanently entrapped TOM-CCs were in a state of medium or low ion permeation. Anchoring of TOM-CC via Tom22 to the hydrogel skeleton adjacent to the membrane triggered channel closure.

These observations are fully consistent with the Cryo-EM structure of the TOM-CC (Bausewein et al., 2017; Ornelas et al., 2023), where the two IMS domains of Tom22 clearly protrude at least 2 nm from the membrane, far enough to make contact with the hydrogel skeleton beneath the membrane. The majority of TOM-CC molecules (67 %) were in a non-diffusive,

intermediate and low permeation state when permanently anchored to Ni-NTA hydrogel via His-tagged Tom22 compared to 28 % of complexes in DIB membranes supported by unmodified agarose. In the presence of imidazole, the TOM-CC molecules were in motion and in a state of high permeation. Whenever the IMS domain of Tom22 touched the hydrogel, this triggered the closure of both Tom40 channels within the TOM-CC. There are two possible molecular models to explain this result that may be worth investigating in more detail in the near future:

i. The dimer interface of the Tom40 barrel is limited to only nine amino acid residues that contribute to the interface on the cytosolic side of the barrel. At the IMS side of the barrel, two conserved lysine residues (Tom40-K298, contributed from each Tom40 monomer) seem to severely destabilize the dimer (Figure 6.3A) (for review, see Bausewein et al., 2020; Ornelas et al., 2023). In fact, most of the stabilizing interactions of the Tom40 dimer seem to be contributed by residues from the interacting, rigid Tom22 subunits and a lipid phosphate group (Figure 6.3B) (Araiso et al., 2019; Tucker and Park, 2019; for review, see Bausewein et al., 2020; Ornelas et al., 2023). Thus, the conformation of the Tom40 barrel dimer is essentially determined by the positioning of the two Tom22 subunits (Figure 6.4). When the IMS domains of the Tom22 subunits interact with the matrix of the agarose gel, the Tom22 subunits might force the Tom40 subunits to rotate slightly against each other at their interface. This could cause the cytosolically located N-terminal domain of the Tom22 subunit to "fall into" the Tom40 channel, thereby blocking Ca^{2+} export in the TIRF experiment.
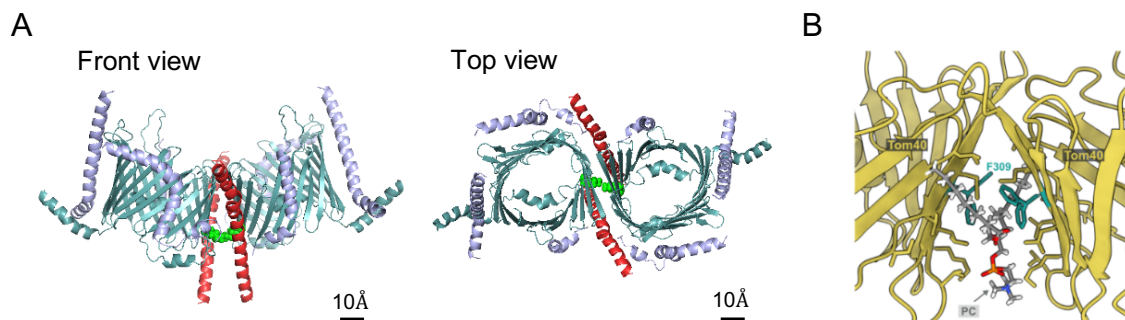
Figure 6.3: Stabilization of TOM-CC dimer by a phospholipid. *A) Two conserved lysine residues (green, K298) in Tom40 (EMDB, EMD-3761; (Bausewein et al., 2017a, 2020)) destabilizing dimeric TOM-CC. B) Close-up view of the Tom40 dimer interface. Phosphatidylcholine (PC) interacts with K298 on each Tom40 subunit through its phosphate group (courtesy to Pamela Ornelas).*
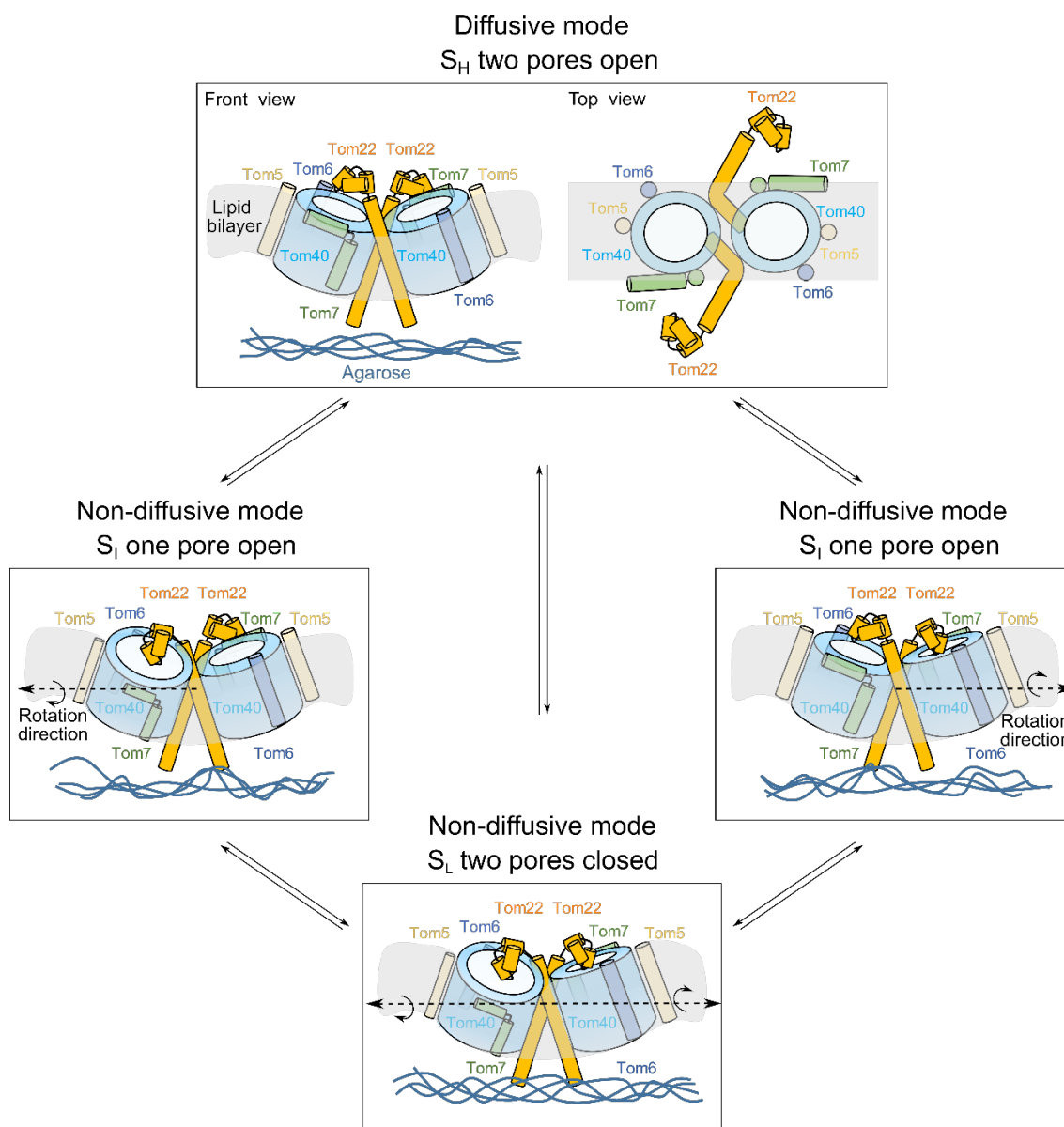
Figure 6.4: Tom40 rotation model for opening and closing the TOM-CC channel. *In diffusive mode (top), TOM-CC can move laterally in the membrane. Both Tom40 pores are open (S_H). There is no interaction between the IMS domain of Tom22 and the hydrogel. In non-diffusive mode (bottom), TOM-CC molecules are trapped. One or two Tom40 pores are closed (S_I and S_L). At least one Tom22 IMS domain binds to the hydrogel. If a Tom22 IMS domain binds to the hydrogel, this could force Tom40 to undergo a conformational change along the membrane axis (dashed line), blocking the Tom22 cytosolic domain from a Tom40 pore.*

ii. A mechanical stimulus caused by interacting with the hydrogel is acting on the IMS domain of Tom22. The stimulus is then transferred to the cytosolic domain of Tom22, causing a conformational change of its cytosolic domain (Figure 6.5). This may block a Tom40 pore.
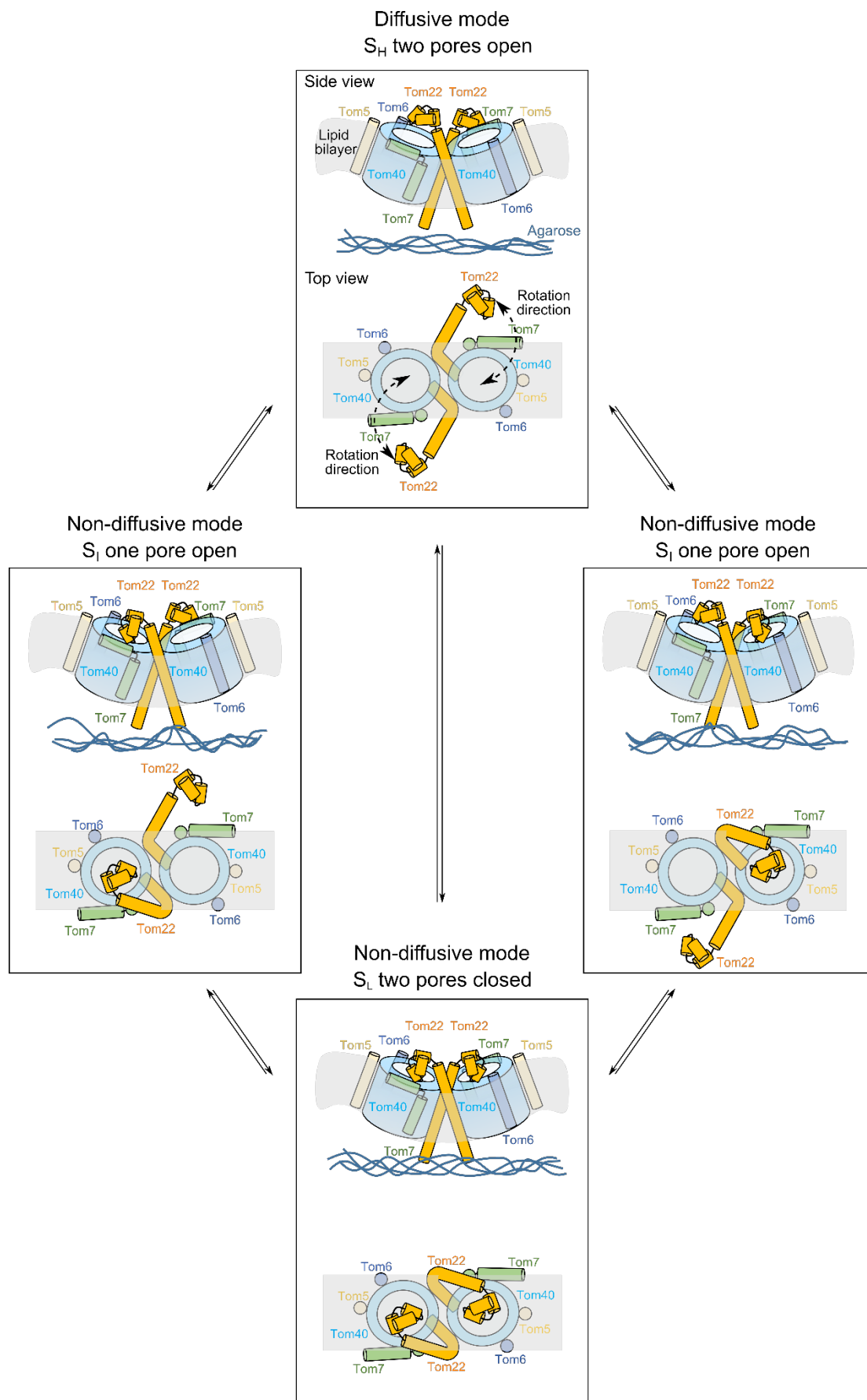
Figure 6.5: Tom22 'scissors' model for opening and closing the TOM-CC channel. *The TOM complex is almost completely embedded in the lipid bilayer (top), except for its cytosolic and IMS Tom22 domains*

(Su et al., 2022). It can move freely in the membrane (diffusive mode) and its two pores are open (S_H). The IMS domain of Tom22 does not interact with the hydrogel. In the non-diffusive mode, TOM-CC is trapped by the interaction of at least one IMS domain of Tom22 with the hydrogel (bottom). This, in turn, causes Tom22 to rotate between the Tom40 barrels (like "scissors") and block a Tom40 pore by a cytosolic Tom22 domain (S_I and S_L).

In vivo, a mechanical stimulus acting on the IMS domain of Tom22 could be caused by physical interaction with Tim50 of the TIM23 machinery in the inner mitochondrial membrane during protein import (Figure 3.1) (Mokranjac et al., 2009; Shiota et al., 2011; Callegari et al., 2020). When a preprotein appears at the exit of the TOM-CC channel in the IMS, it is transferred from Tom22 to Tim50, a preprotein receptor of TIM23. To achieve this handover, both complexes are in close proximity to each other. In this work, it could be demonstrated for the first time that the channel activity of TOM-CC correlates with its *stop-and-go* dynamics. It is therefore very intriguing to conclude that binding of Tom22 to Tim50 results not only in mitochondrial contact sites, but also causing closure of Tom40 pores.

Recently, extensive structural and physical data common to mechanosensitive membrane proteins have been reviewed (for review, see Jin et al., 2020; for review, see Kefauver et al., 2020). The structural data allowed mechanosensitive proteins and protein complexes (all of which were comprised of transmembrane α-helices) to be separated into five different classes, each subject to characteristic underlying molecular mechanisms. They also showed that for the membrane channels considered, fundamental physical properties of the membrane can influence channel activity. This ancient mechanism to regulate open-closed channel activity has also been observed in MSL1, a mitochondrial ion channel that dissipates the mitochondrial membrane potential to maintain redox homeostasis during abiotic stress (Lee et al., 2016; Walewska et al., 2018; Deng et al., 2020; Li et al., 2020).

This work provides first in vitro evidence for a membrane β-barrel protein complex that exhibits membrane state-dependent mechanosensitive-like properties. The findings indicate that the channel opening of TOM-CC can be described by the "tether model" for mechanosensitive ion channels (for review, see Kefauver et al., 2020). Here, a protein anchor Tom22 interacting with a structural periphery of the membrane restricts the lateral diffusion of the TOM complex, as observed for a large number of α-helical membrane proteins (for review, see Martinac, 2004; Brohawn et al., 2014; Ge et al., 2018; Wang et al., 2019b; for review, see Jin et al., 2020; for

review, see Kefauver et al., 2020). Since the TOM-CC complex bends the outer mitochondrial membrane locally towards the intermembrane space with an average radius of about 140Å (Lomize et al., 2022), the anchor domains of the two Tom22 subunits should easily be able to dock with other proteins in the mitochondrial intermembrane space and the mitochondrial inner membrane. It will be interesting to study as to whether the mechanostimulated conformational change of the TOM-CC observed in vitro can be confirmed in intact mitochondria. However, the physiological significance of this mechanostimulated closure remains to be investigated.

7 Conclusions

In this work, the channel activity and lateral mobility of individual TOM core complexes were investigated at the single-molecule level. Here, Ca^{2+}-ion flux through individual TOM-CCs was measured by monitoring the fluorescence emission of a Ca^{2+} sensitive dye in close proximity to the membrane using TIRF microscopy in the absence of membrane potential. By doing so, four discoveries were made:

i.   The TOM-CC channel presents three ion permeation states, corresponding to its dimeric structure. These permeation states can switch reversibly between each other.

ii. Freely moving TOM-CC molecules can be transiently trapped in lipid membranes.

iii. Freely mobile TOM-CC molecules are only found in the high ion permeation (S_H) state. Temporarily trapped TOM-CC channels were mostly observed in intermediate or low ion permeation states (S_I and S_L).

iv. Tom22 plays an important role in causing TOM-CC molecules to change into non-diffusive mode in a lipid membrane. The mechanical interaction of its IMS domain with structures below the membrane triggers the closure of TOM-CC Tom40 pores.

8 Future perspectives

My results raise a fundamental question: are the two Tom40 channels open continually, as static Cryo-EM structures seem to indicate (Bausewein et al., 2017; Araiso et al., 2019; Tucker and Park, 2019; Wang et al., 2020), or can the protein channels be actively influenced by interaction with exogenous interacting proteins near the membrane that restrict the movement of the TOM-CC? To address this question, future work will require the development of new *in vivo* assays to investigate the role of intrinsic TOM-CC dynamics in real mitochondria. Special attention must be paid to mitochondrial protein import. Another aspect that is important to understand is how Tom22 blocks the ion flux through Tom40 at the molecular level. Conformational changes in Tom22, for example, can be studied by single-molecule FRET experiments. Finally, it will be interesting to see whether the opening of the TOM-CC channel is regulated only by the mechanical interaction of Tom22 with peripheral structures of the membrane or is also mechanically influenced by membrane tension. Since the insertion of TOM-CC into lipid membranes is accompanied by a local change in membrane curvature (Demirel and Gerbaud, 2019; Lomize et al., 2022), one can imagine that the activity of TOM-CC also depends on this parameter. Furthermore, in addition to studying TOM, the experimental approach described in this work could complement established optical methods such as fluorescence correlation spectroscopy (for review, see Elson, 2011) and single-molecule particle tracking (Kubitscheck, 2006) to study mechanosensitive ion channels (for review, see Kefauver et al., 2020) in membranes.

9 Bibliography

Abe Y, Shodai T, Muto T, Mihara K, Torii H, Nishikawa S, Endo T & Kohda D (2000) Structural basis of presequence recognition by the mitochondrial protein import receptor Tom20. *Cell* 100: 551–560

Ahting U, Thieffry M, Engelhardt H, Hegerl R, Neupert W & Nussberger S (2001) Tom40, the pore-forming component of the protein-conducting TOM channel in the outer membrane of mitochondria. *J Cell Biol* 153: 1151–1160

Ahting U, Thun C, Hegerl R, Typke D, Nargang FE, Neupert W & Nussberger S (1999) The TOM core complex: the general protein import pore of the outer membrane of mitochondria. *J Cell Biol* 147: 959–968

Alberts B, Johnson A, Lewis J, Raff M, Roberts K & Walter P (2002) Integrins. *Mol Biol Cell 4th Ed*

Alenghat FJ & Golan DE (2013) Membrane protein dynamics and functional implications in mammalian cells. *Curr Top Membr* 72: 89–120

Appelhans T & Busch KB (2017) Dynamic imaging of mitochondrial membrane proteins in specific sub-organelle membrane locations. *Biophys Rev* 9: 345–352

Appelhans T, Richter CP, Wilkens V, Hess ST, Piehler J & Busch KB (2012) Nanoscale organization of mitochondrial microcompartments revealed by combining tracking and localization microscopy. *Nano Lett* 12: 610–616

Araiso Y, Imai K & Endo T (2021) Structural snapshot of the mitochondrial protein import gate. *FEBS J* 288: 5300–5310

Araiso Y, Tsutsumi A, Qiu J, Imai K, Shiota T, Song J, Lindau C, Wenz L-S, Sakaue H, Yunoki K, *et al* (2019) Structure of the mitochondrial import gate reveals distinct preprotein paths. *Nature* 575: 395–401

Baba T, Toshima Y, Minamikawa H, Hato M, Suzuki K & Kamo N (1999) Formation and characterization of planar lipid bilayer membranes from synthetic phytanyl-chained glycolipids. *Biochim Biophys Acta BBA - Biomembr* 1421: 91–102

Banci L, Bertini I, Cefaro C, Cenacchi L, Ciofi-Baffoni S, Felli IC, Gallo A, Gonnelli L, Luchinat E, Sideris D, *et al* (2010) Molecular chaperone function of Mia40 triggers consecutive induced folding steps of the substrate in mitochondrial protein import. *Proc Natl Acad Sci* 107: 20190–20195

Bausewein T, Mills DJ, Langer JD, Nitschke B, Nussberger S & Kühlbrandt W (2017) Cryo-EM structure of the TOM core complex from *Neurospora crassa*. *Cell* 170: 693–700

Bausewein T, Naveed H, Liang J & Nussberger S (2020) The structure of the TOM core complex in the mitochondrial outer membrane. *Biol Chem* 401: 687–697

Bayley H, Cronin B, Heron A, Holden MA, Hwang WL, Syeda R, Thompson J & Wallace M (2008) Droplet interface bilayers. *Mol Biosyst* 4: 1191–1208

Bayrhuber M, Meins T, Habeck M, Becker S, Giller K, Villinger S, Vonrhein C, Griesinger C, Zweckstetter M & Zeth K (2008) Structure of the human voltage-dependent anion channel. *Proc Natl Acad Sci* 105: 15370–15375

Becker L, Bannwarth M, Meisinger C, Hill K, Model K, Krimmer T, Casadio R, Truscott KN, Schulz GE, Pfanner N, *et al* (2005) Preprotein translocase of the outer mitochondrial membrane: reconstituted Tom40 forms a characteristic TOM Pore. *J Mol Biol* 353: 1011–1020

Becker T, Pfannschmidt S, Guiard B, Stojanovski D, Milenkovic D, Kutik S, Pfanner N, Meisinger C & Wiedemann N (2008) Biogenesis of the mitochondrial TOM complex: Mim1 promotes insertion and assembly of signal-anchored receptors. *J Biol Chem* 283: 120–127

Becker T, Wenz L-S, Krüger V, Lehmann W, Müller JM, Goroncy L, Zufall N, Lithgow T, Guiard B, Chacinska A, *et al* (2011) The mitochondrial import protein Mim1 promotes biogenesis of multispanning outer membrane proteins. *J Cell Biol* 194: 387–395

Benz R (2006) Bacterial and eukaryotic porins: structure, function, mechanism John Wiley & Sons

Beverly KN, Sawaya MR, Schmid E & Koehler CM (2008) The Tim8–Tim13 complex has multiple substrate binding sites and binds cooperatively to Tim23. *J Mol Biol* 382: 1144–1156

Bhagawati M, Arroum T, Webeling N, Montoro AG, Mootz HD & Busch KB (2021) The receptor subunit Tom20 is dynamically associated with the TOM complex in mitochondria of human cells. *Mol Biol Cell* 32: br1

Bhakdi S & Tranum-Jensen J (1991) Alpha-toxin of *Staphylococcus aureus*. *Microbiol Rev* 55: 733–751

Bieligmeyer M, Artukovic F, Nussberger S, Hirth T, Schiestel T & Müller M (2016) Reconstitution of the membrane protein OmpF into biomimetic block copolymer–phospholipid hybrid membranes. *Beilstein J Nanotechnol* 7: 881–892

Botelho SC, Österberg M, Reichert AS, Yamano K, Björkholm P, Endo T, von Heijne G & Kim H (2011) TIM23-mediated insertion of transmembrane α-helices into the mitochondrial inner membrane. *EMBO J* 30: 1003–1011

Bradford MM (1976) A rapid and sensitive method for the quantitation of microgram quantities of protein utilizing the principle of protein-dye binding. *Anal Biochem* 72: 248–254

Braha O, Gu L-Q, Zhou L, Lu X, Cheley S & Bayley H (2000) Simultaneous stochastic sensing of divalent metal ions. *Nat Biotechnol* 18: 1005–1007

Bratic A & Larsson N-G (2013) The role of mitochondria in aging. *J Clin Invest* 123: 951–957

Brix J, Rüdiger S, Bukau B, Schneider-Mergener J & Pfanner N (1999) Distribution of binding sequences for the mitochondrial import receptors Tom20, Tom22, and Tom70 in a

presequence-carrying preprotein and a non-cleavable preprotein. *J Biol Chem* 274: 16522–16530

Brohawn SG, Campbell EB & MacKinnon R (2014) Physical mechanism for gating and mechanosensitivity of the human TRAAK K$^+$ channel. *Nature* 516: 126–130

Callegari S, Cruz-Zaragoza LD & Rehling P (2020) From TOM to the TIM23 complex – handing over of a precursor. *Biol Chem* 401: 709–721

Chacinska A, Lind M, Frazier AE, Dudek J, Meisinger C, Geissler A, Sickmann A, Meyer HE, Truscott KN, Guiard B, *et al* (2005) Mitochondrial presequence translocase: switching between TOM tethering and motor recruitment involves Tim21 and Tim17. *Cell* 120: 817–829

Chacinska A, Pfannschmidt S, Wiedemann N, Kozjak V, Sanjuán Szklarz LK, Schulze-Specking A, Truscott KN, Guiard B, Meisinger C & Pfanner N (2004) Essential role of Mia40 in import and assembly of mitochondrial intermembrane space proteins. *EMBO J* 23: 3735–3746

Checkley MA, Luttge BG & Freed EO (2011) HIV-1 envelope glycoprotein biosynthesis, trafficking, and incorporation. *J Mol Biol* 410: 582–608

Colombini M, Blachly-Dyson E & Forte M (1996) VDAC, a channel in the outer mitochondrial membrane. In *Ion channels*, Narahashi T (ed) pp 169–202. Boston, MA: Springer US

Cowan S, Garavito R, Jansonius J, Jenkins J, Karlsson R, König N, Pai E, Pauptit R, Rizkallah P, Rosenbusch J, *et al* (1995) The structure of OmpF porin in a tetragonal crystal form. *Structure* 3: 1041–1050

Cowan SW, Schirmer T, Rummel G, Steiert M, Ghosh R, Pauptit RA, Jansonius JN & Rosenbusch JP (1992) Crystal structures explain functional properties of two *E. coli* porins. *Nature* 358: 727–733

Daum G & Vance JE (1997) Import of lipids into mitochondria. *Prog Lipid Res* 36: 103–130

Davy A, Gale NW, Murray EW, Klinghoffer RA, Soriano P, Feuerstein C & Robbins SM (1999) Compartmentalized signaling by GPI-anchored ephrin-A5 requires the Fyn tyrosine kinase to regulate cellular adhesion. *Genes Dev* 13: 3125–3135

De Pinto V, Reina S, Guarino F & Messina A (2008) Structure of the voltage dependent anion channel: state of the art. *J Bioenerg Biomembr* 40: 139–147

Demirel Y & Gerbaud V (2019) Chapter 11 - Thermodynamics and biological systems. In *Nonequilibrium thermodynamics (Fourth Edition)*, Demirel Y & Gerbaud V (eds) pp 489–571. Elsevier

Demishtein-Zohary K & Azem A (2017) The TIM23 mitochondrial protein import complex: function and dysfunction. *Cell Tissue Res* 367: 33–41

Deng Z, Maksaev G, Schlegel AM, Zhang J, Rau M, Fitzpatrick JAJ, Haswell ES & Yuan P (2020) Structural mechanism for gating of a eukaryotic mechanosensitive channel of small conductance. *Nat Commun* 11: 3690

Dolezal P, Likic V, Tachezy J & Lithgow T (2006) Evolution of the molecular machines for protein import into mitochondria. *Science* 313: 314–318

Dustin ML & Choudhuri K (2016) Signaling and polarized communication across the T cell immunological synapse. *Annu Rev Cell Dev Biol* 32: 303–325

Edidin M (1992) Patches, posts and fences: proteins and plasma membrane domains. *Trends Cell Biol* 2: 376–380

Einstein A (1905) Über die von der molekularkinetischen Theorie der Wärme geforderte Bewegung von in ruhenden Flüssigkeiten suspendierten Teilchen. *Ann Phys* 322: 549–560

Elson EL (2011) Fluorescence correlation spectroscopy: past, present, future. *Biophys J* 101: 2855–2870

Finney DJ (1941) On the distribution of a variate whose logarithm is normally distributed. *Suppl J R Stat Soc* 7: 155–161

Fritzsche M, Li D, Colin-York H, Chang VT, Moeendarbary E, Felce JH, Sezgin E, Charras G, Betzig E & Eggeling C (2017) Self-organizing actin patterns shape membrane architecture but not cell mechanics. *Nat Commun* 8: 14347

Fujiwara TK, Iwasawa K, Kalay Z, Tsunoyama TA, Watanabe Y, Umemura YM, Murakoshi H, Suzuki KGN, Nemoto YL, Morone N, *et al* (2016) Confined diffusion of transmembrane proteins and lipids induced by the same actin meshwork lining the plasma membrane. *Mol Biol Cell* 27: 1101–1119

Fukasawa Y, Tsuji J, Fu S-C, Tomii K, Horton P & Imai K (2015) MitoFates: improved prediction of mitochondrial targeting sequences and their cleavage sites. *Mol Cell Proteomics MCP* 14: 1113–1126

Ge J, Elferich J, Goehring A, Zhao H, Schuck P & Gouaux E (2018) Structure of mouse protocadherin 15 of the stereocilia tip link in complex with LHFPL5. *eLife* 7: e38770

Gebert N, Chacinska A, Wagner K, Guiard B, Koehler CM, Rehling P, Pfanner N & Wiedemann N (2008) Assembly of the three small Tim proteins precedes docking to the mitochondrial carrier translocase. *EMBO Rep* 9: 548–554

Gennis RB (1989) Biomembranes: molecular structure and function. Springer

Gessmann D, Flinner N, Pfannstiel J, Schlösinger A, Schleiff E, Nussberger S & Mirus O (2011a) Structural elements of the mitochondrial preprotein-conducting channel Tom40 dissolved by bioinformatics and mass spectrometry. *Biochim Biophys Acta* 1807: 1647–1657

Gessmann D, Mager F, Naveed H, Arnold T, Weirich S, Linke D, Liang J & Nussberger S (2011b) Improving the resistance of a eukaryotic β-barrel protein to thermal and chemical perturbations. *J Mol Biol* 413: 150–161

Geula S, Naveed H, Liang J & Shoshan-Barmatz V (2012) Structure-based analysis of VDAC1 protein. *J Biol Chem* 287: 2179–2190

Gevorkyan-Airapetov L, Zohary K, Popov-Čeleketić D, Mapa K, Hell K, Neupert W, Azem A & Mokranjac D (2009) Interaction of Tim23 with Tim50 is essential for protein translocation by the mitochondrial TIM23 complex. *J Biol Chem* 284: 4865–4872

Glick BS, Brandt A, Cunningham K, Müller S, Hallberg RL & Schatz G (1992) Cytochromes c1 and b2 are sorted to the intermembrane space of yeast mitochondria by a stop-transfer mechanism. *Cell* 69: 809–822

Goffeau A, Barrell BG, Bussey H, Davis RW, Dujon B, Feldmann H, Galibert F, Hoheisel JD, Jacq C, Johnston M, *et al* (1996) Life with 6000 Genes. *Science* 274: 546–567

Gowrishankar K, Ghosh S, Saha S, C R, Mayor S & Rao M (2012) Active remodeling of cortical actin regulates spatiotemporal organization of cell surface molecules. *Cell* 149: 1353–1367

Greaves J, Prescott GR, Gorleku OA & Chamberlain LH (2009) The fat controller: roles of palmitoylation in intracellular protein trafficking and targeting to membrane microdomains (Review). *Mol Membr Biol* 26: 67–79

Gu L-Q, Braha O, Conlan S, Cheley S & Bayley H (1999) Stochastic sensing of organic analytes by a pore-forming protein containing a molecular adapter. *Nature* 398: 686–690

Guo XW, Smith PR, Cognon B, D'Arcangelis D, Dolginova E & Mannella CA (1995) Molecular design of the voltage-dependent, anion-selective channel in the mitochondrial outer membrane. *J Struct Biol* 114: 41–59

Hac-Wydro K & Wydro P (2007) The influence of fatty acids on model cholesterol/phospholipid membranes. *Chem Phys Lipids* 150: 66–81

Haggie PM, Kim JK, Lukacs GL & Verkman AS (2006) Tracking of quantum dot-iabeled CFTR shows near immobilization by C-terminal PDZ interactions. *Mol Biol Cell* 17: 4937–4945

Heine M, Ciuraszkiewicz A, Voigt A, Heck J & Bikbaev A (2016) Surface dynamics of voltage-gated ion channels. *Channels* 10: 267–281

Herrmann JM & Neupert W (2004) Protein transport into mitochondria. In *Encyclopedia of biological chemistry*, Lennarz WJ & Lane MD (eds) pp 510–515. New York: Elsevier

Herrmann JM & Riemer J (2010) The intermembrane space of mitochondria. *Antioxid Redox Signal* 13: 1341–1358

Hill K, Model K, Ryan MT, Dietmeier K, Martin F, Wagner R & Pfanner N (1998) Tom40 forms the hydrophilic channel of the mitochondrial import pore for preproteins. *Nature* 395: 516–521

Hiller S & Wagner G (2009) The role of solution NMR in the structure determinations of VDAC-1 and other membrane proteins. *Curr Opin Struct Biol* 19: 396–401

Hirsch M, Wareham RJ, Martin-Fernandez ML, Hobson MP & Rolfe DJ (2013) A stochastic model for electron multiplication charge-coupled devices – from theory to practice. *PLOS ONE* 8: e53671

Hoffmann W, Sarzala MG & Chapman D (1979) Rotational motion and evidence for oligomeric structures of sarcoplasmic reticulum Ca^{2+}-activated ATPase. *Proc Natl Acad Sci* 76: 3860–3864

Horvath SE & Daum G (2013) Lipids of mitochondria. *Prog Lipid Res* 52: 590–614

Howorka S, Cheley S & Bayley H (2001) Sequence-specific detection of individual DNA strands using engineered nanopores. *Nat Biotechnol* 19: 636–639

Huang S, Romero-Ruiz M, Castell OK, Bayley H & Wallace MI (2015) High-throughput optical sensing of nucleic acids in a nanopore array. *Nat Nanotechnol* 10: 986–991

Jacobson K, Liu P & Lagerholm BC (2019) The lateral organization and mobility of plasma membrane components. *Cell* 177: 806–819

Jacobson K, Mouritsen OG & Anderson RGW (2007) Lipid rafts: at a crossroad between cell biology and physics. *Nat Cell Biol* 9: 7–14

Jaqaman K & Grinstein S (2012) Regulation from within: the cytoskeleton in transmembrane signaling. *Trends Cell Biol* 22: 515–526

Jin P, Jan LY & Jan Y-N (2020) Mechanosensitive ion channels: structural features relevant to mechanotransduction mechanisms. *Annu Rev Neurosci* 43: 207–229

Joo C & Ha T (2008) Single-molecule FRET with total internal reflection microscopy. In *Single-molecule techniques: a laboratory manual*, Selvin PR & Ha T (eds) pp 3–36. Cold Spring Harbor Laboratory Press

Jores T, Klinger A, Groß LE, Kawano S, Flinner N, Duchardt-Ferner E, Wöhnert J, Kalbacher H, Endo T, Schleiff E, *et al* (2016) Characterization of the targeting signal in mitochondrial β-barrel proteins. *Nat Commun* 7: 12036

Kaiser H-J, Orłowski A, Róg T, Nyholm TKM, Chai W, Feizi T, Lingwood D, Vattulainen I & Simons K (2011) Lateral sorting in model membranes by cholesterol-mediated hydrophobic matching. *Proc Natl Acad Sci U S A* 108: 16628–16633

Kang Y, Baker MJ, Liem M, Louber J, McKenzie M, Atukorala I, Ang C-S, Keerthikumar S, Mathivanan S & Stojanovski D (2016) Tim29 is a novel subunit of the human TIM22 translocase and is involved in complex assembly and stability. *eLife* 5: e17463

Kasianowicz JJ, Brandin E, Branton D & Deamer DW (1996) Characterization of individual polynucleotide molecules using a membrane channel. *Proc Natl Acad Sci* 93: 13770–13773

Kawato S, Sigel E, Carafoli E & Cherry RJ (1981) Rotation of cytochrome oxidase in phospholipid vesicles. Investigations of interactions between cytochrome oxidases and between cytochrome oxidase and cytochrome bc1 complex. *J Biol Chem* 256: 7518–7527

Kefala G, Ahn C, Krupa M, Esquivies L, Maslennikov I, Kwiatkowski W & Choe S (2010) Structures of the OmpF porin crystallized in the presence of foscholine-12. *Protein Sci Publ Protein Soc* 19: 1117–1125

Kefauver JM, Ward AB & Patapoutian A (2020) Discoveries in structure and physiology of mechanically activated ion channels. *Nature* 587: 567–576

Keil P, Hönlinger A & Pfanner N (1996) Targeting and translocation of preproteins by the Toms of the mitochondrial receptor complex. In *Advances in Molecular and Cell Biology*, Bittar EE (ed) pp 81–102. Elsevier

Kemper C, Habib SJ, Engl G, Heckmeyer P, Dimmer KS & Rapaport D (2008) Integration of tail-anchored proteins into the mitochondrial outer membrane does not require any known import components. *J Cell Sci* 121: 1990–1998

Kiebler M, Pfaller R, Söllner T, Griffiths G, Horstmann H, Pfanner N & Neupert W (1990) Identification of a mitochondrial receptor complex required for recognition and membrane insertion of precursor proteins. *Nature* 348: 610–616

Koppel DE, Sheetz MP & Schindler M (1981) Matrix control of protein diffusion in biological membranes. *Proc Natl Acad Sci* 78: 3576–3580

Krakow JL, Hereld D, Bangs JD, Hart GW & Englund PT (1986) Identification of a glycolipid precursor of the *Trypanosoma brucei* variant surface glycoprotein. *J Biol Chem* 261: 12147–12153

Krumpe K, Frumkin I, Herzig Y, Rimon N, Özbalci C, Brügger B, Rapaport D & Schuldiner M (2012) Ergosterol content specifies targeting of tail-anchored proteins to mitochondrial outer membranes. *Mol Biol Cell* 23: 3927–3935

Kubitscheck U (2006) Fluorescence microscopy: single particle tracking. In *Encyclopedic reference of genomics and proteomics in molecular medicine* pp 579–583. Berlin, Heidelberg: Springer

Kühlbrandt W (2015) Structure and function of mitochondrial membrane protein complexes. *BMC Biol* 13: 89

Künkele K-P, Heins S, Dembowski M, Nargang FE, Benz R, Thieffry M, Walz J, Lill R, Nussberger S & Neupert W (1998) The preprotein translocation channel of the outer membrane of mitochondria. *Cell* 93: 1009–1019

Kusumi A, Fujiwara TK, Chadda R, Xie M, Tsunoyama TA, Kalay Z, Kasai RS & Suzuki KGN (2012) Dynamic organizing principles of the plasma membrane that regulate signal transduction: commemorating the fortieth anniversary of Singer and Nicolson's fluid-mosaic model. *Annu Rev Cell Dev Biol* 28: 215–250

Kusumi A, Sako Y & Yamamoto M (1993) Confined lateral diffusion of membrane receptors as studied by single particle tracking (nanovid microscopy). Effects of calcium-induced differentiation in cultured epithelial cells. *Biophys J* 65: 2021–2040

Kusumi A, Shirai YM, Koyama-Honda I, Suzuki KGN & Fujiwara TK (2010) Hierarchical organization of the plasma membrane: Investigations by single-molecule tracking vs. fluorescence correlation spectroscopy. *FEBS Lett* 584: 1814–1823

Kusumi A, Suzuki KGN, Kasai RS, Ritchie K & Fujiwara TK (2011) Hierarchical mesoscale domain organization of the plasma membrane. *Trends Biochem Sci* 36: 604–615

Kusumi A, Tsunoyama TA, Hirosawa KM, Kasai RS & Fujiwara TK (2014) Tracking single molecules at work in living cells. *Nat Chem Biol* 10: 524–532

Kuszak AJ, Jacobs D, Gurnev PA, Shiota T, Louis JM, Lithgow T, Bezrukov SM, Rostovtseva TK & Buchanan SK (2015) Evidence of distinct channel conformations and substrate binding affinities for the mitochondrial outer membrane protein translocase pore Tom40. *J Biol Chem* 290: 26204–26217

Kutik S, Stojanovski D, Becker L, Becker T, Meinecke M, Krüger V, Prinz C, Meisinger C, Guiard B, Wagner R, *et al* (2008) Dissecting membrane insertion of mitochondrial β-Barrel proteins. *Cell* 132: 1011–1024

Kutik S, Stroud DA, Wiedemann N & Pfanner N (2009) Evolution of mitochondrial protein biogenesis. *Biochim Biophys Acta BBA - Gen Subj* 1790: 409–415

Kuzmenko A, Tankov S, English BP, Tarassov I, Tenson T, Kamenski P, Elf J & Hauryliuk V (2011) Single molecule tracking fluorescence microscopy in mitochondria reveals highly dynamic but confined movement of Tom40. *Sci Rep* 1: 195

Laemmli UK (1970) Cleavage of structural proteins during the assembly of the head of bacteriophage T4. *Nature* 227: 680–685

Lang T, Bruns D, Wenzel D, Riedel D, Holroyd P, Thiele C & Jahn R (2001) SNAREs are concentrated in cholesterol-dependent clusters that define docking and fusion sites for exocytosis. *EMBO J* 20: 2202–2213

Lebendiker M & Danieli T (2017) Purification of proteins fused to maltose-binding protein. *Methods Mol Biol Clifton NJ* 1485: 257–273

Lee CP, Maksaev G, Jensen GS, Murcha MW, Wilson ME, Fricker M, Hell R, Haswell ES, Millar AH & Sweetlove L (2016) MSL1 is a mechanosensitive ion channel that dissipates mitochondrial membrane potential and maintains redox homeostasis in mitochondria during abiotic stress. *Plant J Cell Mol Biol* 88: 809–825

Lemeshko SV & Lemeshko VV (2000) Metabolically derived potential on the outer membrane of mitochondria: a computational model. *Biophys J* 79: 2785–2800

Leptihn S, Castell OK, Cronin B, Lee E-H, Gross LCM, Marshall DP, Thompson JR, Holden M & Wallace MI (2013) Constructing droplet interface bilayers from the contact of aqueous droplets in oil. *Nat Protoc* 8: 1048–1057

Levental I, Lingwood D, Grzybek M, Coskun Ü & Simons K (2010) Palmitoylation regulates raft affinity for the majority of integral raft proteins. *Proc Natl Acad Sci* 107: 22050–22054

Li Y, Hu Y, Wang J, Liu X, Zhang W & Sun L (2020) Structural insights into a plant mechanosensitive ion channel MSL1. *Cell Rep* 30: 4518-4527.e3

Lindsey H, Petersen NO & Chan SI (1979) Physicochemical characterization of 1,2-diphytanoyl-sn-glycero-3-phosphocholine in model membrane systems. *Biochim Biophys Acta BBA - Biomembr* 555: 147–167

Lionaki E, de Marcos Lousa C, Baud C, Vougioukalaki M, Panayotou G & Tokatlidis K (2008) The essential function of Tim12 *in vivo* is ensured by the assembly interactions of its C-terminal domain. *J Biol Chem* 283: 15747–15753

Lipper CH, Stofleth JT, Bai F, Sohn Y-S, Roy S, Mittler R, Nechushtai R, Onuchic JN & Jennings PA (2019) Redox-dependent gating of VDAC by mitoNEET. *Proc Natl Acad Sci* 116: 19924–19929

Liu AP & Fletcher DA (2006) Actin polymerization serves as a membrane domain switch in model lipid bilayers. *Biophys J* 91: 4064–4070

Lomize AL, Todd SC & Pogozheva ID (2022) Spatial arrangement of proteins in planar and curved membranes by PPM 3.0. *Protein Sci* 31: 209–220

Lutz T, Neupert W & Herrmann JM (2003) Import of small Tim proteins into the mitochondrial intermembrane space. *EMBO J* 22: 4400–4408

Mager F, Gessmann D, Nussberger S & Zeth K (2011) Functional refolding and characterization of two Tom40 isoforms from human mitochondria. *J Membr Biol* 242: 11–21

Mager F, Sokolova L, Lintzel J, Brutschy B & Nussberger S (2010) LILBID-mass spectrometry of the mitochondrial preprotein translocase TOM. *J Phys Condens Matter Inst Phys J* 22: 454132

Mahendran KR, Lamichhane U, Romero-Ruiz M, Nussberger S & Winterhalter M (2013) Polypeptide translocation through the mitochondrial TOM channel: temperature-dependent rates at the single-molecule level. *J Phys Chem Lett* 4: 78–82

Mannella CA (1998) Conformational changes in the mitochondrial channel protein, VDAC, and their functional implications. *J Struct Biol* 121: 207–218

Manzo C & Garcia-Parajo MF (2015) A review of progress in single particle tracking: from methods to biophysical insights. *Rep Prog Phys* 78: 124601

Martin DS, Forstner MB & Käs JA (2002) Apparent subdiffusion inherent to single particle tracking. *Biophys J* 83: 2109–2117

Martinac B (2004) Mechanosensitive ion channels: molecules of mechanotransduction. *J Cell Sci* 117: 2449–2460

Meinecke M, Wagner R, Kovermann P, Guiard B, Mick DU, Hutu DP, Voos W, Truscott KN, Chacinska A, Pfanner N, *et al* (2006) Tim50 maintains the permeability barrier of the mitochondrial inner membrane. *Science* 312: 1523–1526

Menestrina G (1986) Ionic channels formed by Staphylococcus aureus alpha-toxin: voltage-dependent inhibition by divalent and trivalent cations. *J Membr Biol* 90: 177–190

Mesecke N, Terziyska N, Kozany C, Baumann F, Neupert W, Hell K & Herrmann JM (2005) A disulfide relay system in the intermembrane space of mitochondria that mediates protein import. *Cell* 121: 1059–1069

Milovanovic D, Honigmann A, Koike S, Göttfert F, Pähler G, Junius M, Müllar S, Diederichsen U, Janshoff A, Grubmüller H, *et al* (2015) Hydrophobic mismatch sorts SNARE proteins into distinct membrane domains. *Nat Commun* 6: 5984

Mokranjac D & Neupert W (2015) Architecture of a protein entry gate. *Nature* 528: 201–202

Mokranjac D, Sichting M, Popov-Čeleketić D, Mapa K, Gevorkyan-Airapetov L, Zohary K, Hell K, Azem A & Neupert W (2009) Role of Tim50 in the transfer of precursor proteins from the outer to the inner membrane of mitochondria. *Mol Biol Cell* 20: 1400–1407

Mori H & Ito K (2006) Different modes of SecY–SecA interactions revealed by site-directed *in vivo* photo-cross-linking. *Proc Natl Acad Sci* 103: 16159–16164

Morone N, Fujiwara T, Murase K, Kasai RS, Ike H, Yuasa S, Usukura J & Kusumi A (2006) Three-dimensional reconstruction of the membrane skeleton at the plasma membrane interface by electron tomography. *J Cell Biol* 174: 851–862

Müller-Späth S, Soranno A, Hirschfeld V, Hofmann H, Rüegger S, Reymond L, Nettels D & Schuler B (2010) Charge interactions can dominate the dimensions of intrinsically disordered proteins. *Proc Natl Acad Sci* 107: 14609–14614

Muro C, Grigoriev SM, Pietkiewicz D, Kinnally KW & Campo ML (2003) Comparison of the TIM and TOM channel activities of the mitochondrial protein import complexes. *Biophys J* 84: 2981–2989

Murschall LM, Peker E, MacVicar T, Langer T & Riemer J (2021) Protein import assay into mitochondria isolated from human cells. *Bio-Protoc* 11: e4057

Nakae T, Ishii J & Tokunaga M (1979) Subunit structure of functional porin oligomers that form permeability channels in the other membrane of *Escherichia coli*. *J Biol Chem* 254: 1457–1461

Naveed H, Jackups R & Liang J (2009) Predicting weakly stable regions, oligomerization state, and protein–protein interfaces in transmembrane domains of outer membrane proteins. *Proc Natl Acad Sci* 106: 12735–12740

Neupert W & Herrmann JM (2007) Translocation of proteins into mitochondria. *Annu Rev Biochem* 76: 723–749

Nicolson GL (2014) The fluid—mosaic model of membrane structure: still relevant to understanding the structure, function and dynamics of biological membranes after more than 40 years. *Biochim Biophys Acta BBA - Biomembr* 1838: 1451–1466

Nunnari J & Suomalainen A (2012) Mitochondria: in sickness and in health. *Cell* 148: 1145–1159

Ober RJ, Ram S & Ward ES (2004) Localization accuracy in single-molecule microscopy. *Biophys J* 86: 1185–1200

Ornelas P, Bausewein T, Martin J, Morgner N, Nussberger S & Kühlbrandt W (2023) Two conformations of the Tom20 preprotein receptor in the TOM holo complex. 2023.01.26.525638 doi:10.1101/2023.01.26.525638 [PREPRINT]

O'Rourke B (2007) Mitochondrial ion channels. *Annu Rev Physiol* 69: 19–49

Ouldali H, Sarthak K, Ensslen T, Piguet F, Manivet P, Pelta J, Behrends JC, Aksimentiev A & Oukhaled A (2020) Electrical recognition of the twenty proteinogenic amino acids using an aerolysin nanopore. *Nat Biotechnol* 38: 176–181

Owen DM, Williamson D, Rentero C & Gaus K (2009) Quantitative microscopy: protein dynamics and membrane organisation. *Traffic* 10: 962–971

Paulick MG & Bertozzi CR (2008) The glycosylphosphatidylinositol anchor: a complex membrane-anchoring structure for proteins. *Biochemistry* 47: 6991–7000

Peleh V, Cordat E & Herrmann JM (2016) Mia40 is a trans-site receptor that drives protein import into the mitochondrial intermembrane space by hydrophobic substrate binding. *eLife* 5: e16177

Pfanner N, Warscheid B & Wiedemann N (2019) Mitochondrial protein organization: from biogenesis to networks and function. *Nat Rev Mol Cell Biol* 20: 267–284

Podkalicka J, Biernatowska A, Majkowski M, Grzybek M & Sikorski AF (2015) MPP1 as a factor regulating phase separation in giant plasma membrane-derived vesicles. *Biophys J* 108: 2201–2211

Poynor M, Eckert R & Nussberger S (2008) Dynamics of the preprotein translocation channel of the outer membrane of mitochondria. *Biophys J* 95: 1511–1522

Qiu J, Wenz L-S, Zerbes RM, Oeljeklaus S, Bohnert M, Stroud DA, Wirth C, Ellenrieder L, Thornton N, Kutik S, *et al* (2013) Coupling of mitochondrial import and export translocases by receptor-mediated supercomplex formation. *Cell* 154: 596–608

Rahman B, Kawano S, Yunoki-Esaki K, Anzai T & Endo T (2014) NMR analyses on the interactions of the yeast Tim50 C-terminal region with the presequence and Tim50 core domain. *FEBS Lett* 588: 678–684

Ramadurai S, Duurkens R, Krasnikov VV & Poolman B (2010) Lateral diffusion of membrane proteins: consequences of hydrophobic mismatch and lipid composition. *Biophys J* 99: 1482–1489

Ramadurai S, Holt A, Krasnikov V, van den Bogaart G, Killian JA & Poolman B (2009) Lateral diffusion of membrane proteins. *J Am Chem Soc* 131: 12650–12656

Rapaport D, Künkele K-P, Dembowski M, Ahting U, Nargang FE, Neupert W & Lill R (1998) Dynamics of the TOM complex of mitochondria during binding and translocation of preproteins. *Mol Cell Biol* 18: 5256–5262

Redwood WR, Pfeiffer FR, Weisbach JA & Thompson TE (1971) Physical properties of bilayer membranes formed from a synthetic saturated phospholipid in n-decane. *Biochim Biophys Acta BBA - Biomembr* 233: 1–6

Rege TA & Hagood JS (2006) Thy-1, a versatile modulator of signaling affecting cellular adhesion, proliferation, survival, and cytokine/growth factor responses. *Biochim Biophys Acta BBA - Mol Cell Res* 1763: 991–999

Rehling P, Model K, Brandner K, Kovermann P, Sickmann A, Meyer HE, Kühlbrandt W, Wagner R, Truscott KN & Pfanner N (2003) Protein insertion into the mitochondrial inner membrane by a twin-pore translocase. *Science* 299: 1747–1751

Rissler M, Wiedemann N, Pfannschmidt S, Gabriel K, Guiard B, Pfanner N & Chacinska A (2005) The essential mitochondrial protein Erv1 cooperates with Mia40 in biogenesis of intermembrane space proteins. *J Mol Biol* 353: 485–492

Roise D, Horvath SJ, Tomich JM, Richards JH & Schatz G (1986) A chemically synthesized pre-sequence of an imported mitochondrial protein can form an amphiphilic helix and perturb natural and artificial phospholipid bilayers. *EMBO J* 5: 1327–1334

Rojo EE, Stuart RA & Neupert W (1995) Conservative sorting of F0-ATPase subunit 9: export from matrix requires delta pH across inner membrane and matrix ATP. *EMBO J* 14: 3445–3451

Romero-Ruiz M, Mahendran KR, Eckert R, Winterhalter M & Nussberger S (2010) Interactions of mitochondrial presequence peptides with the mitochondrial outer membrane preprotein translocase TOM. *Biophys J* 99: 774-781. 10.1016/j.bpj.2010.05.010

Rosholm KR, Baker MAB, Ridone P, Nakayama Y, Rohde PR, Cuello LG, Lee LK & Martinac B (2017) Activation of the mechanosensitive ion channel MscL by mechanical stimulation of supported Droplet-Hydrogel bilayers. *Sci Rep* 7: 45180

Saffman PG (1976) Brownian motion in thin sheets of viscous fluid. *J Fluid Mech* 73: 593–602

Saffman PG & Delbrück M (1975) Brownian motion in biological membranes. *Proc Natl Acad Sci* 72: 3111–3113

Saha S, Lee I-H, Polley A, Groves JT, Rao M & Mayor S (2015) Diffusion of GPI-anchored proteins is influenced by the activity of dynamic cortical actin. *Mol Biol Cell* 26: 4033–4045

Sanderson JM (2012) Resolving the kinetics of lipid, protein and peptide diffusion in membranes. *Mol Membr Biol* 29: 118–143

Schmidt O, Harbauer AB, Rao S, Eyrich B, Zahedi RP, Stojanovski D, Schönfisch B, Guiard B, Sickmann A, Pfanner N, *et al* (2011) Regulation of mitochondrial protein import by cytosolic kinases. *Cell* 144: 227–239

Schmidt R, Weihs T, Wurm CA, Jansen I, Rehman J, Sahl SJ & Hell SW (2021) MINFLUX nanometer-scale 3D imaging and microsecond-range tracking on a common fluorescence microscope. *Nat Commun* 12: 1478

Schmidt U & Weiss M (2010) Hydrophobic mismatch-induced clustering as a primer for protein sorting in the secretory pathway. *Biophys Chem* 151: 34–38

Schneider R, Hosy E, Kohl J, Klueva J, Choquet D, Thomas U, Voigt A & Heine M (2015) Mobility of calcium channels in the presynaptic membrane. *Neuron* 86: 672–679

Schulz C & Rehling P (2014) Remodelling of the active presequence translocase drives motor-dependent mitochondrial protein translocation. *Nat Commun* 5: 4349

Schwarzer R, Levental I, Gramatica A, Scolari S, Buschmann V, Veit M & Herrmann A (2014) The cholesterol-binding motif of the HIV-1 glycoprotein gp41 regulates lateral sorting and oligomerization. *Cell Microbiol* 16: 1565–1581

Scorrano L, De Matteis MA, Emr S, Giordano F, Hajnóczky G, Kornmann B, Lackner LL, Levine TP, Pellegrini L, Reinisch K, *et al* (2019) Coming together to define membrane contact sites. *Nat Commun* 10: 1287

Sebald W, Neupert W & Weiss H (1979) Preparation of *Neurospora crassa* mitochondria. In *Methods in Enzymology* pp 144–148. Academic Press

Selvin PR, Lougheed T, Hoffman MT, Park H, Balci H, Belehm BH & Toprak E (2008) *In vitro & in vivo* FIONA and other acronyms for watching molecular motors walk. In *Single-molecule techniques: a laboratory manual*, Selvin PR & Ha T (eds) pp 37–71. Cold Spring Harbor Laboratory Press

Seu KJ, Cambrea LR, Everly RM & Hovis JS (2006) Influence of lipid chemistry on membrane fluidity: tail and headgroup interactions. *Biophys J* 91: 3727–3735

Sezgin E, Levental I, Mayor S & Eggeling C (2017) The mystery of membrane organization: composition, regulation and roles of lipid rafts. *Nat Rev Mol Cell Biol* 18: 361–374

Sharma O, Yamashita E, Zhalnina MV, Zakharov SD, Datsenko KA, Wanner BL & Cramer WA (2007) Structure of the complex of the colicin E2 R-domain and its BtuB receptor. The outer membrane colicin translocon. *J Biol Chem* 282: 23163–23170

Sheetz MP (1983) Membrane skeletal dynamics: role in modulation of red cell deformability, mobility of transmembrane proteins, and shape. *Semin Hematol* 20: 175–188

Shiota T, Imai K, Qiu J, Hewitt VL, Tan K, Shen H-H, Sakiyama N, Fukasawa Y, Hayat S, Kamiya M, *et al* (2015) Molecular architecture of the active mitochondrial protein gate. *Science* 349: 1544–1548

Shiota T, Mabuchi H, Tanaka-Yamano S, Yamano K & Endo T (2011) *In vivo* protein-interaction mapping of a mitochondrial translocator protein Tom22 at work. *Proc Natl Acad Sci* 108: 15179–15183

Shoshan-Barmatz V, Keinan N, Abu-Hamad S, Tyomkin D & Aram L (2010) Apoptosis is regulated by the VDAC1 N-terminal region and by VDAC oligomerization: release of cytochrome c, AIF and Smac/Diablo. *Biochim Biophys Acta BBA - Bioenerg* 1797: 1281–1291

Söllner T, Pfaller R, Griffiths G, Pfanner N & Neupert W (1990) A mitochondrial import receptor for the ADP/ATP carrier. *Cell* 62: 107–115

Sondermann M, George M, Fertig N & Behrends JC (2006) High-resolution electrophysiology on a chip: transient dynamics of alamethicin channel formation. *Biochim Biophys Acta BBA - Biomembr* 1758: 545–551

Song J, Midson C, Blachly-Dyson E, Forte M & Colombini M (1998) The sensor regions of VDAC are translocated from within the membrane to the surface during the gating processes. *Biophys J* 74: 2926–2944

Song L, Hobaugh MR, Shustak C, Cheley S, Bayley H & Gouaux JE (1996) Structure of staphylococcal alpha-hemolysin, a heptameric transmembrane pore. *Science* 274: 1859–1866

Spector J, Zakharov S, Lill Y, Sharma O, Cramer WA & Ritchie K (2010) Mobility of BtuB and OmpF in the *Escherichia coli* outer membrane: implications for dynamic formation of a translocon complex. *Biophys J* 99: 3880–3886

Štefanová I, Hořejši V, Ansotegui IJ, Knapp W & Stockinger H (1991) GPI-anchored cell-surface molecules complexed to protein tyrosine kinases. *Science* 254: 1016–1019

Stoddart D, Heron AJ, Klingelhoefer J, Mikhailova E, Maglia G & Bayley H (2010) Nucleobase recognition in ssDNA at the central constriction of the alpha-hemolysin pore. *Nano Lett* 10: 3633–3637

Straub SP, Stiller SB, Wiedemann N & Pfanner N (2016) Dynamic organization of the mitochondrial protein import machinery. *Biol Chem* 397: 1097–1114

Su J, Liu D, Yang F, Zuo M-Q, Li C, Dong M-Q, Sun S & Sui S-F (2022) Structural basis of Tom20 and Tom22 cytosolic domains as the human TOM complex receptors. *Proc Natl Acad Sci* 119: e2200158119

Sugawara T, Yamashita D, Kato K, Peng Z, Ueda J, Kaneko J, Kamio Y, Tanaka Y & Yao M (2015) Structural basis for pore-forming mechanism of staphylococcal α-hemolysin. *Toxicon* 108: 226–231

Sukhorukov VM, Dikov D, Busch K, Strecker V, Wittig I & Bereiter-Hahn J (2010) Determination of protein mobility in mitochondrial membranes of living cells. *Biochim Biophys Acta - Biomembr* 1798: 2022–2032

Tanaka M & Sackmann E (2005) Polymer-supported membranes as models of the cell surface. *Nature* 437: 656–663

Teijido O, Ujwal R, Hillerdal C-O, Kullman L, Rostovtseva TK & Abramson J (2012) Affixing N-terminal α-helix to the wall of the voltage-dependent anion channel does not prevent its voltage gating. *J Biol Chem* 287: 11437–11445

Thomas DD & Hidalgo C (1978) Rotational motion of the sarcoplasmic reticulum Ca^{2+}-ATPase. *Proc Natl Acad Sci* 75: 5488–5492

Thompson RE, Larson DR & Webb WW (2002) Precise nanometer localization analysis for individual fluorescent probes. *Biophys J* 82: 2775–2783

Truscott KN, Kovermann P, Geissler A, Merlin A, Meijer M, Driessen AJ, Rassow J, Pfanner N & Wagner R (2001) A presequence- and voltage-sensitive channel of the mitochondrial preprotein translocase formed by Tim23. *Nat Struct Biol* 8: 1074–1082

Truscott KN, Wiedemann N, Rehling P, Müller H, Meisinger C, Pfanner N & Guiard B (2002) Mitochondrial import of the ADP/ATP carrier: the essential TIM complex of the intermembrane space is required for precursor release from the TOM complex. *Mol Cell Biol* 22: 7780–7789

Tucker K & Park E (2019) Cryo-EM structure of the mitochondrial protein-import channel TOM complex at near-atomic resolution. *Nat Struct Mol Biol* 26: 1158–1166

Tulodziecka K, Diaz-Rohrer BB, Farley MM, Chan RB, Di Paolo G, Levental KR, Waxham MN & Levental I (2016) Remodeling of the postsynaptic plasma membrane during neural development. *Mol Biol Cell* 27: 3480–3489

Ujwal R, Cascio D, Colletier J-P, Faham S, Zhang J, Toro L, Ping P & Abramson J (2008) The crystal structure of mouse VDAC1 at 2.3 Å resolution reveals mechanistic insights into metabolite gating. *Proc Natl Acad Sci* 105: 17742–17747

Valpadashi A, Callegari S, Linden A, Neumann P, Ficner R, Urlaub H, Deckers M & Rehling P (2021) Defining the architecture of the human TIM22 complex by chemical crosslinking. *FEBS Lett* 595: 157–168

Vasiljev A, Ahting U, Nargang FE, Go NE, Habib SJ, Kozany C, Panneels V, Sinning I, Prokisch H, Neupert W, *et al* (2004) Reconstituted TOM core complex and Tim9/Tim10 complex of mitochondria are sufficient for translocation of the ADP/ATP carrier across membranes. *Mol Biol Cell* 15: 1445–1458

Venkatesan GA, Taylor GJ, Basham CM, Brady NG, Collier CP & Sarles SA (2018) Evaporation-induced monolayer compression improves droplet interface bilayer formation using unsaturated lipids. *Biomicrofluidics* 12: 024101

Vicente NB, Zamboni JED, Adur JF, Paravani EV & Casco VH (2007) Photobleaching correction in fluorescence microscopy images. *J Phys Conf Ser* 90: 012068

Vögtle F-N, Wortelkamp S, Zahedi RP, Becker D, Leidhold C, Gevaert K, Kellermann J, Voos W, Sickmann A, Pfanner N, *et al* (2009) Global analysis of the mitochondrial N-proteome identifies a processing peptidase critical for protein stability. *Cell* 139: 428–439

Walewska A, Kulawiak B, Szewczyk A & Koprowski P (2018) Mechanosensitivity of mitochondrial large-conductance calcium-activated potassium channels. *Biochim Biophys Acta BBA - Bioenerg* 1859: 797–805

Walther DM & Rapaport D (2009) Biogenesis of mitochondrial outer membrane proteins. *Biochim Biophys Acta BBA - Mol Cell Res* 1793: 42–51

Wang W, Chen X, Zhang L, Yi J, Ma Q, Yin J, Zhuo W, Gu J & Yang M (2020) Atomic structure of human TOM core complex. *Cell Discov* 6: 1–10

Wang Y, Guo Y, Liu C, Wang L, Zhang A, Yan Z & Song C (2019a) Push-to-open: the gating mechanism of the tethered mechanosensitive ion channel NompC. *bioRxiv*: 853721

Wang Y, Wang Y, Du X, Yan S, Zhang P, Chen H-Y & Huang S (2019b) Electrode-free nanopore sensing by DiffusiOptoPhysiology. *Sci Adv* 5: eaar3309

Wang Y, Yan S, Zhang P, Zeng Z, Zhao D, Wang J, Chen H & Huang S (2018) Osmosis-driven motion-type modulation of biological nanopores for parallel optical nucleic acid sensing. *ACS Appl Mater Interfaces* 10: 7788–7797

Webb CT, Gorman MA, Lazarou M, Ryan MT & Gulbis JM (2006) Crystal structure of the mitochondrial chaperone TIM9.10 reveals a six-bladed α-propeller. *Mol Cell* 21: 123–133

Weinhäupl K, Lindau C, Hessel A, Wang Y, Schütze C, Jores T, Melchionda L, Schönfisch B, Kalbacher H, Bersch B, *et al* (2018) Structural basis of membrane protein chaperoning through the mitochondrial intermembrane space. *Cell* 175: 1365-1379.e25

Wenz L-S, Ellenrieder L, Qiu J, Bohnert M, Zufall N, van der Laan M, Pfanner N, Wiedemann N & Becker T (2015) Sam37 is crucial for formation of the mitochondrial TOM–SAM supercomplex, thereby promoting β-barrel biogenesis. *J Cell Biol* 210: 1047–1054

Wiedemann N, Kozjak V, Chacinska A, Schönfisch B, Rospert S, Ryan MT, Pfanner N & Meisinger C (2003) Machinery for protein sorting and assembly in the mitochondrial outer membrane. *Nature* 424: 565–571

Wiedemann N & Pfanner N (2017) Mitochondrial machineries for protein import and assembly. *Annu Rev Biochem* 86: 685–714

Wiedemann N, Pfanner N & Ryan MT (2001) The three modules of ADP/ATP carrier cooperate in receptor recruitment and translocation into mitochondria. *EMBO J* 20: 951–960

van Wilpe S, Ryan MT, Hill K, Maarse AC, Meisinger C, Brix J, Dekker PJT, Moczko M, Wagner R, Meijer M, *et al* (1999) Tom22 is a multifunctional organizer of the mitochondrial preprotein translocase. *Nature* 401: 485–489

Winkler K, Karner A, Horner A, Hannesschlaeger C, Knyazev D, Siligan C, Zimmermann M, Kuttner R, Pohl P & Preiner J (2020) Interaction of the motor protein SecA and the bacterial protein translocation channel SecYEG in the absence of ATP. *Nanoscale Adv* 2: 3431–3443

Yamano K, Tanaka-Yamano S & Endo T (2010) Tom7 regulates Mdm10-mediated assembly of the mitochondrial import channel protein Tom40. *J Biol Chem* 285: 41222–41231

Young JC, Hoogenraad NJ & Hartl FU (2003) Molecular chaperones Hsp90 and Hsp70 deliver preproteins to the mitochondrial import receptor Tom70. *Cell* 112: 41–50

Zhang F, Lee GM & Jacobson K (1993) Protein lateral mobility as a reflection of membrane microstructure. *BioEssays* 15: 579–588

Zimmerberg J & Parsegian VA (1986) Polymer inaccessible volume changes during opening and closing of a voltage-dependent ionic channel. *Nature* 323: 36–39

Zinser E, Sperka-Gottlieb CD, Fasch EV, Kohlwein SD, Paltauf F & Daum G (1991) Phospholipid synthesis and lipid composition of subcellular membranes in the unicellular eukaryote Saccharomyces cerevisiae. *J Bacteriol* 173: 2026–2034

Zorova LD, Popkov VA, Plotnikov EY, Silachev DN, Pevzner IB, Jankauskas SS, Babenko VA, Zorov SD, Balakireva AV, Juhaszova M, *et al* (2018) Mitochondrial membrane potential. *Anal Biochem* 552: 50–59

10 Curriculum vitae

Personal details

Name:	Shuo Wang
Date and place of birth:	15.10.1990, Kaifeng, China
Nationality:	Chinese

Education

Feb. 2019 – Jul. 2023	PhD student at the Institute of Biomaterials and Biomolecular Systems, Department of Biophysics (Prof. Stephan Nussberger), University of Stuttgart, Germany
Apr. 2017 – May 2018	Master thesis at the Max Planck Institute for Intelligent Systems, Physical Intelligence Department (Prof. Dr. Metin Sitti, Prof. Dr. Joachim Bill), Stuttgart, Germany
Oct. 2015 – May 2018	Studies in Materials Science (Master of Science), University of Stuttgart, Germany
Sep. 2010 – Jun. 2014	Studies in Polymer Materials and Engineering (Bachelor of Engineering), Zhengzhou University of Light Industry, China

Professional experience

Jul. 2018 – Dec. 2018	Research assistant at the Max Planck Institute for Intelligent Systems, Physical Intelligence Department (Prof. Dr. Metin Sitti, Dr. Ajay Vikram Singh), Stuttgart, Germany

Awards

2021 – 2022	Short term PhD fellowship (Lgf-Stipendium, Ministry of Education of Baden-Württemberg)
2012 – 2013	The National Scholarship (Ministry of Education of the People's Republic of China)
2010 – 2011	The National Encouragement Scholarship (Henan Province Education Department)

11 Publications

Tracking the activity and position of mitochondrial β-barrel proteins

Shuo Wang and Stephan Nussberger (in: Springer Protocols, Methods in Molecular Biology on "Membrane beta-barrel proteins", Editor Raffaele Ieva, in press)

Single-molecule imaging of lateral mobility and ion channel activity in lipid bilayers using total internal reflection fluorescence (TIRF) microscopy

Shuo Wang and Stephan Nussberger (Journal of Visualized Experiments, 2023, (192), e64970)

Optical single-channel recordings reveal correlation between lateral protein diffusion and channel activity of TOM

Shuo Wang and Stephan Nussberger (Nature Bioengineering Community Blog, 2022)

Spatiotemporal stop-and-go dynamics of the mitochondrial TOM core complex correlates with channel activity

Shuo Wang, Lukas Findeisen, Sebastian Leptihn, Mark I Wallace, Marcel Hörning, and Stephan Nussberger (Communications Biology, 2022, 5(1), 1-11)

Multifunctional magnetic hairbot for untethered osteogenesis, ultrasound contrast imaging and drug delivery

Ajay Vikram Singh, Mohammad Hasan Dad Ansari, Cem Balda Dayan, Joshua Giltinan, Shuo Wang, Yan Yu, Vimal Kishore, Peter Laux, Andreas Luch, and Metin Sitti (Biomaterials, 2019, 219, 119394)

The adoption of three-dimensional additive manufacturing from biomedical material design to 3D organ printing

Ajay Vikram Singh, Mohammad Hasan Dad Ansari, Shuo Wang, Peter Laux, Andreas Luch, Amit Kumar, Rajendra Patil, and Stephan Nussberger (Applied Science, 2019, 9(4), 811)

Peptide-induced biomineralization of tin oxide (SnO$_2$) nanoparticles for antibacterial applications

Ajay Vikram Singh, Timotheus Jahnke, Yang Xiao, Shuo Wang, Yan Yu, Hilda David, Gunther Richter, Peter Laux, Andreas Luch, Anchal Srivastava, Preeti S Saxena, Joachim Bill, and Metin Sitti (Journal of Nanoscience and Nanotechnology, 2019, 19(9), 5674-5686)

Anisotropic gold nanostructures: optimization via in silico modeling for hyperthermia

Ajay Vikram Singh*, Timotheus Jahnke*, Shuo Wang*, Yang Xiao, Yunus Alapan, Soheila Kharratian, Mehmet Cengiz Onbasli, Kristen Kozielski, Hilda David, Gunther Richter, Joachim Bill, Peter Laux, Andreas Luch, and Metin Sitti (ACS Applied. Nano Materials, 2018, 1(11), 6205–6216), *equal contribution.

12 Acknowledgements

I would like to express my sincere thanks to my PhD supervisor Prof. Dr. Stephan Nussberger. He has offered me many trainings in single molecule imaging, membrane protein biochemistry and data analysis. His trainings are my treasures for my future research, especially his rigorous thinking in data analysis. I always appreciated talking to him about my work. He gave me all the freedom to do the experiments I wanted to do. In addition, he also helped me a lot in my daily life in Stuttgart. I would also like to thank Prof. Dr. Robin Ghosh of the Department of Bioenergetics for his listening ear, his extremely valuable advice, his continuous encouragement and for taking the time to review my thesis as a co- examiner.

A big thank you also goes to Prof. Dr. Laura Na Liu (2nd Institute of Physics, University of Stuttgart). I am grateful for her support during the last six months of my PhD and for involving me in the collaboration with her group in the field of DNA origami and synthetic cells.

I would like to thank Beate Nitschke for her continuous support in growing *Neurospora*, purifying mitochondria and her help in isolating all my proteins. Special thanks also go to Lukas Findeisen for initial advice, to Dr. Marcel Hörning who helped me set up the MATLAB program for data analysis, and to Dr. Stephan Eisler for his help with our TIRF microscope. I am very grateful to PD Dr. Maximillian Ulbrich for his advice in calculating the positional accuracy of my TOM molecules. Thanks to Prof. Dr. Jörg Wrachtrup and Jun. Prof. Dr. Michael Heymann for the regular use of their plasma cleaners. Without access to such a - actually simple - device, my work at the single-molecule level would not have been possible. Pamela Ornelas and Dr. Thomas Bausewein (Max Planck Institute for Biophysics) provided preproteins for my thesis. I really thank for that.

It is very important for me to thank my friends Dr. Sisi Fan, Dr. Longjiang Ding and M.Sc. Xiang Hao in Stuttgart, Dr. Ruirui Song in Japan, and M.Sc. Chensi Wang and B.A. Ziqian Yang in my hometown. They have given me many wonderful moments.

Finally, I am very grateful to my parents and grandparents for their love and understanding.